ABSTRACT

A Photogrammetric Method for Measuring
Transient Frost Surface Roughness

Taber Scott Miyauchi, M.S.M.E.

Mentor: Stephen T. McClain, Ph.D.

Cold-soaked fuel frost (CSFF) is a form of aircraft wing contamination that results in aerodynamic degradation. Unless a certification exemption for a specific aircraft model is provided by the FAA, an operator of an aircraft is not allowed to takeoff with CSFF on aircraft wing surfaces. To assist manufacturers in the design of air vehicles and to assist the FAA in evaluating exemption requests, frost roughness evolution must be characterized and modeled. However, measuring transient frost roughness is difficult because of the optical and material properties of frost. This experimental investigation presents a nonintrusive, in-situ method of measuring frost roughness using structure-from-motion photogrammetry. This method was validated with fabricated rough surfaces and was used on a closed-loop psychrometric wind tunnel that is capable of producing frost formations in various environmental conditions. The resulting roughness parameters and detailed height distributions were analyzed to determine the effects of each environmental variable.

A Photogrammetric Method for Measuring Transient Frost Surface Roughness

by

Taber Scott Miyauchi, B.S.M.E.

A Thesis

Approved by the Department of Mechanical Engineering

_____

Paul I. Ro, Ph.D., Chairperson

Submitted to the Graduate Faculty of
Baylor University in Partial Fulfillment of the
Requirements for the Degree
of
Master of Science in Mechanical Engineering

Approved by the Thesis Committee

_____

Stephen T. McClain, Ph.D., Chairperson

_____

Dennis O'Neal, Ph.D.

_____

Enrique Blair, Ph.D.

Accepted by the Graduate School
December 2018

_____

J. Larry Lyon, Ph.D., Dean

Page bearing signatures is kept on file in the Graduate School.

TABLE OF CONTENTS

LIST OF FIGURES

LIST OF TABLES

NOMENCLATURE

A	Mean surface area
A_s	Roughness element wetted area of windward surface
A_p	Roughness element frontal area
b	Vector that lies along same plane as $\varepsilon_{\#}$
C	Chord length
C_d	Change in drag coefficient
C_f	Skin-friction coefficient
C_L	Change in lift coefficient
D	Average roughness element relative spacing
d	Displacement of image location from physical location
k_s	Equivalent sand-grain roughness
L	Distance from start of viscous boundary layer to location of interest
l	Fuselage length
P	Degrees of coverage on upper length of airfoil
Pp_i	Perspective projection matrix
P_i	Camera image consisting of all pixels or 2D matrix of all elements
q''	Heat flux
R	Object point location
R_q	Root-mean-square height
r_i	Pixel in image or element in matrix that corresponds with R

S	Wing surface area
Skw	Skewness
S_q	Surface point cloud file
T_{dp}	Dew-point temperature
T_f	Frost surface temperature
T_{fp}	Fog-point temperature
T_s	Surface temperature
T_∞	Freestream temperature
u	Velocity
U_∞	Freestream velocity
V_c	Aircraft velocity
w	Weighting factor proportional to the number of frost nucleation sites
W_c	Weight of clean, unfrosted aircraft
w_s	Humidity ratio
x	Ordinate value
x_f	Frost thickness
y	Ordinate value
$Z(x, y)$	Distance normal to single point from mean surface height of all points
z	Wall-normal distance from plate surface

Greek

α	Angle of attack
β_i	Light ray or vector that corresponds with r_i

Δ	Change in term of interest
ε_i	Epipolar line in P_i
λ	Equivalent roughness element spacing ratio
μ	Dynamic fluid viscosity
ρ	Fluid density
ρ_a	Air density
τ_w	Wall shear stress

Abbreviations

AF	Auto focus
AFM	Airplane Flight Manual
ANOVA	Analysis of Variance
AT	Air temperature
AV	Air velocity
CFR	Code of Federal Regulations
CMOS	Complementary metal-oxide semiconductor
CRC	Close range correction
CRM	Common research model
CSFF	Cold-soaked fuel frost
DACS	Data acquisition and control system
DSLR	Digital single-lens reflex
FAA	Federal Aviation Association
ISO	Image sensor optimization

NASA	National Aeronautics and Space Administration
NI	National Instruments
PCM	Phase change material
P2V	Peak-to-valley
RH	Relative humidity
RMS	Root-mean-square
SCR	Silicon-controlled rectifier
ST	Surface temperature
STL	Stereolighography

ACKNOWLEDGMENTS

First and foremost, I owe many thanks to Dr. Stephen McClain who served as my mentor not just academically, but personally by passing on many valuable life lessons. His support and guidance are greatly valued. I would also like to thank Dr. Dennis (Dean) O'Neal for his invaluable knowledge on frost formation and Dr. Enrique (Erik) Blair for both serving as members on my thesis committee. Their assistance is highly appreciated.

Many thanks to my predecessors in the Baylor Icing Group, Tim Shannon, John-Mark Clemenson, Zac Williams and Jaime McCarrell for their friendship and support during my time at Baylor. I also owe much thanks to Tony Zhang whose passing knowledge of the Baylor Frost Tunnel enabled the successful completion of my research. Along with Tony, many thanks are extended to Andy McAllister who assisted in the operation of the wind tunnel. I also appreciate the work of Mr. Ashley Orr in manufacturing various brackets for the camera traversing system. I cannot leave out my friends from LeTourneau whose phones calls and text messages of encouragement are most appreciated.

My deepest gratitude goes out to my family. To my parents, thank you for your constant love which instilled in me strong values and for your sacrifices which provided me the opportunity for an outstanding education. To Elly, Logan, Sam and Alex, I have not thanked you enough for your love and support over the years.

The research efforts reported in this paper were supported by the FAA through Grant No. 17-G-011. Any opinions presented in this work are those of the author and do not reflect the views of the FAA or the United States government.

DEDICATION

To my family

CHAPTER ONE

Introduction

Cold-soaked frost is a phenomenon that occurs when an aircraft surface reaches below-freezing temperatures in certain atmospheric conditions, resulting in frost contamination on the surface. This problem commonly occurs when an aircraft is flown to a spoke airport with enough fuel for both the departure and return trip from a central hub. During the flight to these spoke airports, an aircraft may reach cruising heights of 10,000 meters, which will cause the extra fuel and wing surfaces to reach temperatures around or below -25 °C. Upon landing at airports with relatively cold air temperatures and high humidity levels, an aircraft can develop what is referred to as cold-soaked fuel frost on aircraft surfaces surrounding the fuel tanks.

Motivation

Frost accumulation adversely affects the aerodynamic performance of an aircraft because it makes an aircraft surface rough. The roughness causes greater turbulence in the boundary layer resulting in a reduced lift margin and increased drag [1]. This degradation has the greatest impact during takeoff, as evidenced by the crash of a frost contaminated Bombardier Challenger in 2002 [2]. Multiple crashes like this have occurred over the years resulting in the death of numerous people. For safety reasons, the FAA has restricted the takeoff of an aircraft with frost contamination on the upper surface of a wing, unless an exemption is granted for an aircraft model. An example of a specific aircraft model that has received exemption with appropriate CSFF limitations is the Boeing 737-700, -800 and

-900 Next Generation airplanes [3]. All other aircraft are required to takeoff under the Federal Aviation Regulation 14 CFR Part 135.227 [4]. This regulation requires that an airplane is free of frost, ice or snow contamination otherwise a deicing or alternative procedure must be used to clean aircraft surfaces before takeoff. Therefore, aircraft operators are required to clean the aircraft wings if CSFF occurs. However, deicing equipment is not always readily available when conditions cause cold-soaked fuel frost and other options are time consuming such as emptying and refilling the fuel tanks.

Regardless of the availability of de-frosting methods, aircraft operators desire exemption for takeoff with CSFF wings as this would save time and money. Therefore, airframe manufacturers are expected to pursue designs that safely operate with CSFF at takeoff and may be approved for exemption requests for CSFF takeoffs. This has led airframe manufacturers to consult with the FAA about exemptions for takeoff with cold-soaked fuel frosted wings. The FAA has responded by considering the approval of aircraft model exemptions for specific cold-soaked frost contaminations that are visibly marked within a zone and takeoff limitations are outlined within an FAA approved Airplane Flight Manual (AFM) [3]. However, to give clear guidance on these limitations for airframe manufacturers and the FAA, a public database of frost roughness evolution, modeled at various psychrometric conditions is needed. Therefore, a method to accurately measure frost surface roughness had to be established in order to understand the complete aerodynamic impact of frost.

Surface roughness has been a challenge and topic of interest for over a century because it affects the efficiency, safety and reliability of engineered components and systems. Roughness, like that caused by CSFF, has an undesirable impact in industries

concerning fluid flow and heat transfer. Some additional applications in these industries include conduit piping, marine hulls and gas-turbine blades. In each of these applications, surface roughness reduces the efficiency of the system and in some cases the safety. A rough surface increases the skin friction resulting in a higher drag force [1]. When heat transfer is a concern, surface roughness will increase the convective heat losses [5]. Additionally, in the materials engineering industry surface roughness affects the reliability of numerous products that are manufactured from molding, casting, metal working, machining, composites, and additive fabrication. In this industry, surface roughness generally decreases the life span of a component due to friction [6] and surface crack initiation sites.

In fluid flow and heat transfer engineering, surface roughness has been measured with pin-needle micrometers, hand tracings, plaster molds, profilometers and laser scanning. Each application of measuring surface roughness presents a unique challenge. In some cases surface roughness is in a difficult to access area, like the inner walls of a pipe. Additionally, surface deformities may range in miniscule sizes from centimeters to microns. Other times roughness is characterized by different spatial disconformities in all surface directions making it a meticulous process to measure. Furthermore, surface contaminations may be sensitive to temperature, contact forces and transient in value. Determining a method to measure surface roughness varies between each application.

In this study a new method for measuring miniscule surface roughness accretion is established. This method had to be minimally invasive, a rapid data collection process, capable of measuring objects on the scale of microns and in situ to where the frost would be experimentally accreted. This established method uses a photogrammetric

structure-from-motion method adapted from aerial surveying. The process incorporates capturing overlapping photos of frost developed in a closed-loop psychrometric wind tunnel. From the corresponding pixels in each 2D photo, a 3D topographical point cloud model of the frost may be computed. Upon scaling the point cloud to the correct size, the roughness statistics of the frost may be calculated. The resulting measurements and computations produce frost height distributions and a one-dimensional frost roughness time plot for each atmospheric test condition.

Objectives

There were two primary objectives of this study. The first was to develop, validate, and implement a method for measuring frost roughness. The second was to identify the most important parameters governing frost roughness formation in application to aircraft cold-soaked fuel frost. The objective of establishing a measuring method was broken into two areas of research: data collection and computational process. The data collection process detailed the physical steps to obtaining accurate and usable data which could then be used in the computational process. The computational process reduced the raw data images into detailed height distributions using a structure-from-motion photogrammetric method. From the height distributions, another computation determined specific roughness parameters. The objective of identifying the governing atmospheric factors occurred through the analysis of frost roughness measurements obtained at various environmental conditions of air temperature, relative humidity, air speed, and surface temperature. The post analysis examined the roughness parameters in time evolution plots for a wide range of psychrometric conditions to understand the fundamental development of frost roughness and the significance of each atmospheric factor. From these results the most influential

environmental factors were presented and assessed for predicting when critical CSFF conditions occurred. The method and results will serve as a foundation for future studies on cold-soaked fuel frost since the data from this research alone does not present a comprehensive database of a psychrometric prediction model of frost on aircraft wings.

Order of Presentation

The remainder of this paper is outlined in the following order. Chapter Two provides technical background in the areas of frost formation, surface roughness, frost roughness, and photogrammetry. Chapter Three outlines the methodology and experimental apparatuses used to collect data. Additionally, this chapter will describe the calibration method and the data reduction process. Chapter Four provides the photogrammetric results of frost roughness and the implication of the results. Chapter Five concludes with recommendations for improving the photogrammetric method and future work.

CHAPTER TWO

Technical Background

The following chapter provides a brief review on technical concepts relevant to the current investigation. The background information reviews frost formation theory and previous research methods for characterizing surface roughness. Additionally, this chapter introduces the application and fundamental mathematics of photogrammetry for measuring surface roughness. The chapter concludes with relevant surface roughness parameters and their implication to the aerodynamic effects of CSFF roughness.

Frost Theory

Formation

Frost formation is a complex process that occurs through mass and heat transfer on a cold surface. Georgiadis [7] described frost growth as two competing process:

1. Ice deposition occurring from water vapor.
2. Water vapor condensation to liquid solidification followed by ice crystal growth from water vapors.

The first process, defined as desublimation frosting, is dominant when air temperatures are below the triple point of water (.01 °C and 0.611 kPA) or for surface temperatures below -20 °C. Desublimation frosting is commonly referred to as hoar frosting in the aviation industry [8]. It usually consists of a feathery nature, which is significantly rougher than the contending frost process. The second process, called condensation frosting, is dominant for air temperatures and partial pressures above the triple point and for surface temperatures

from -20 °C to 0 °C [9]. Essentially, both processes create ice crystals that make up frost, however condensation frosting has an initial phase where nucleation sites form from water droplets. Additionally, the structure and surface roughness of the two types of frost vary. This research focuses on frost formations that primarily occur through condensation frosting, however desublimation is also a consideration because CSFF may reach surface temperatures below -20 °C.

Understanding the temperature at which frost will form is critical to predicting frost roughness. Dietenberger [10] derived a weighting factor (w) (proportional to the number of nucleation sites available) that determines the surface temperature (T_f) at which frost will form at various conditions. The weighting factor has a value between 0 and 1. The atmospheric conditions can be determined by the dew-point temperature (T_{dp}) and the fog-point temperature (T_{fp}). Dew-point is the temperature that air conditions would need to be cooled, to achieve fully saturated air (100% relative humidity) [11]. Fog-point temperature is dependent upon the air temperature, saturation ratio for fog nucleation, and the Schmidt number [10]. In a more general sense, fogging occurs when water vapor becomes supercooled water droplets in the boundary layer, resulting in water droplet condensation on the surface. The following equation implies that for a weighting factor of 0, the surface frost point would be the temperature at which fog forms near the surface.

$$T_f = w\,T_{dp} + (1 - w)\,T_{fp} \tag{2.1}$$

The frost growth process of condensation to freezing can be conceptualized as three stages [7]:

1. Water vapor condense to water droplets, which supercool then coalesce.
2. The droplets suddenly freeze forming nucleation sites.

3. Ice dendrites grow from the nucleation sites toward the humid air stream and accumulate in a porous crystalline matrix called frost.

A summary of the three stages of condensation frosting is shown in Figure 2.1.

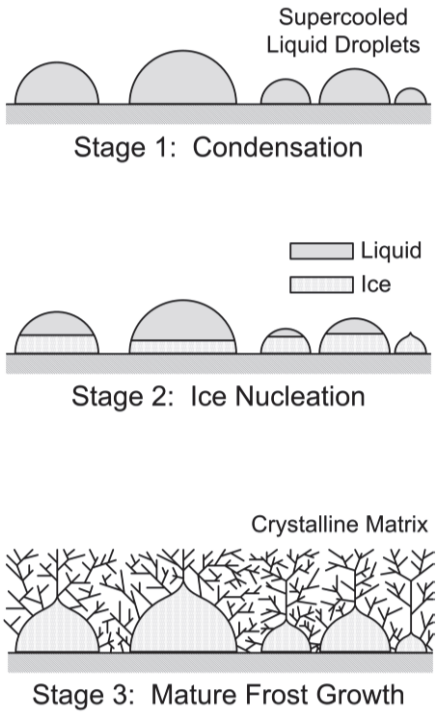

Figure 2.1 Three Stages of Condensation Frosting [12]

Frost Modeling

The third stage of frost growth has the greatest reduction on airflow and heat transfer; therefore this stage has always been the most significant concern in engineering industries. One dimensional frost thickness growth models of the third stage have been developed, but these vary in scope and complexity. The most accurate models characterize the mass transport and heat transfer through the following sections: the air to the top of the frost layer, the inner crystalline matrix, and the base of the frost to the cold surface. The majority of these models are based off of the work of Jones and Parker [13]. Some of the

subsequent models include modifications to account for thermal conductivity and density [14]. Other models include corrections to mass transfer and convection coefficients at the surface to moist air interface [15–19]. While these models present valid estimations for frost thickness as a function of environmental conditions, they lack results on frost roughness. The motivation for the development of all these models has been for characterizing frost thickness in refrigeration and heat exchangers where frost roughness is not a very critical factor. Therefore, substantial experimental measurement data is still needed before analytically modeling frost roughness evolution as a function of air velocity, air temperature, humidity, and surface temperature.

Surface Roughness Measurements

Measuring surface roughness introduces the initial step to understanding the effect roughness has on a fluid flow and convective heat transfer. Because limited and unverified research has been conducted in measuring frost roughness, it is important to first review established methods for measuring surface roughness before focusing on frost roughness measurement methods.

Traditional Methods

The most traditional method for measuring micro level surface roughness is a contact profilometer. Contact profilometers operate based on the displacement of a stylus as it drawn over a surface. This displacement can be mapped as a 2D profile or a 3D surface depending on the tracking capabilities of the system [20]. However, a profilometer is inadequate for measuring frost roughness because even the smallest of contact forces will alter the structural formation of the frost.

The most similar surface accretion to frost that has been precisely measured is ice accretion on the wings of aircraft. In the Icing Research Tunnel at NASA Glenn Research Center, several methods for measuring ice roughness have been established [21–23]. The oldest of these methods is a casting method that uses a relatively warm wax to create a mold of the ice. The mold is then cast in a plaster to create a replicate of the ice shape. Additionally a hand tracing method was established that uses a hot wire to cut a slot in the ice. A piece of cardboard is then slid into the slot and the ice shape is then traced by hand onto the cardboard [21]. However, these established ice measuring methods cannot adequately measure frost roughness because frost is more sensitive to physical contact and temperature. Frost will be altered at the smallest of contact forces or changes in temperature and since the exact roughness of frost is desired to be measured at specific atmospheric conditions, the frost cannot be altered in any way. A more advanced method established at NASA uses a laser scanner (comprised of a laser diode sheet and a CCD camera) to obtain a 3D model of the ice shape [22–26]. Yet before the ice is scanned, a coat of white paint is applied through an airbrush to the ice surface to properly capture roughness details with the laser acquisition system. All laser scanners require transparent objects to be coated with a white paint in order to capture all details [22,27]. Other forms of light-induced, noncontact surface measuring methods include diffraction pattern recognition, electromagnetic wave interferometry and chromatic confocal profilometery [28–30]. However for all of these technologies, if the surface is transparent it will affect the accuracy of the measurement. Since frost is partially transparent and refracts light, it would have to be painted for accurate measurements. Consequently, laser scanning and other light

metrology methods cannot adequately detail the surface elements of frost roughness, because the required airbrush painting would deform and break the frost dendrites.

In reviewing these established methods, it becomes evident that a new technique for measuring frost roughness is required. This method must not alter the temperature surrounding the frost, incur no physical contact, and use technology that is not affected by the transparency of frost. Furthermore, frost grows at a relatively rapid pace even with a low rate of moist air impingement, so an expedited method for collecting the frost roughness data is required.

Frost Roughness Characterization

In the context of measuring surface roughness resulting from frost, several research efforts have been performed. However, none of these studies achieved high levels of accuracy or presented validation of the measurements. On a side note, the majority of these research efforts have focused on environmental frost, in refrigeration and hoar frosting scenarios. Environmental frost and cold-soaked fuel frost are similar enough in structure that examining the measurement techniques employed in these studies is still beneficial for determining a more accurate and adaptive method for measuring cold-soaked fuel frost.

In 1964, Chen and Rohsenow [31] compared images of frost formed on the surface of a clear heat exchanger to sand grain sizes. Their efforts were to determine a correlation between frost roughness and the sand grain equivalent roughness model [32]. Although Chen and Rohsenow's results were qualitative, they concluded that in the initial growth phase, frost roughness and thickness are dependent. Once the frost developed, the roughness and thickness become independent. Additionally, they concluded that frost roughness is the most critical factor to determining pressure drop and heat transfer in a

frosted pipe. Dietenberger [10] built upon Chen and Rohsenow's theoretical work to determine a frost formation model. His work focused on the thickness of the frost; however he attempted to relate the frost thickness (x_f) to a roughness equivalence (k_s) as shown in Eq. (2.2).

$$k_s = 1.66\, x_f \tag{2.2}$$

Dietenberger's equation was useful for indicating the order of magnitude of frost roughness effects, however it was based off of theoretical work for flow regimes in closed conduits. Dietenberger recognized this by stating that his frost formation model is different from what is expected for frost formation on aircraft wings.

Further research comes from Lawrysyn [33] measuring environmental frost in application to aircraft frost contamination. Lawrysyn conducted experiments by placing thick aluminum plates outside overnight in subfreezing temperatures. Once frost had accumulated on the plate, the surface roughness was captured using a polyvinyl formal plastic material dissolved in ethylene dichloride. The solution was poured along the edge of the plate, seeping into the frost and slowly evaporated, leaving behind a plastic mold of the frost. The frost height along a profile was then measured using several methods. One method utilized a profilometer type device that was drawn over the frost dendrites [34]. The more optimum method measured the maximum and minimum frost heights visually using a feeler gauge and watchmaker's eyepiece. A frost roughness height of 0.4 millimeters was reported as an average value. Additionally, the frost dendrite spacing was evaluated optically by counting the number of particles in a square inch. The reported density of frost dendrites ranged from 12 to 30 particles/in^2 where only the highest 20% of the frost grains were counted. Also, the shape of frost elements was empirically determined

by comparing elements to known surface roughness shapes. These parameters were applied to Dirling's [35] experimental data that correlated roughness density to equivalent sand-grain roughness as modeled in Eq. (2.3).

$$\lambda = \frac{D}{k_s}\left(\frac{A_s}{A_p}\right)^{4/3} \tag{2.3}$$

The work of Lawrysyn presents a valid method for measuring frost, however there is several limitations. The method of applying the polyvinyl ethylene dichloride solution, was contingent upon the temperature of the solution and the technique of pouring the solution onto the slanted plate. The optical roughness height measurements were highly dependent upon the measurer's ability. The spacing parameter was subjective as Lawrysyn determined to only count the highest 20% of the frost grains. Moreover, the frost results only apply to hoar frost without controlled ambient conditions or incremental time measurements, thereby eliminating the possibility of creating a frost prediction model.

In 2002, Yun et al. [36] performed experiments in a closed-loop wind tunnel by measuring the frost height over time on a refrigerated test plate. The minimum and maximum frost heights were measured using a needle-pointed micrometer and a magnifier to check for contact. From the resulting measurements (Figure 2.2), a one-dimension model of the frost roughness as a function of time was created.

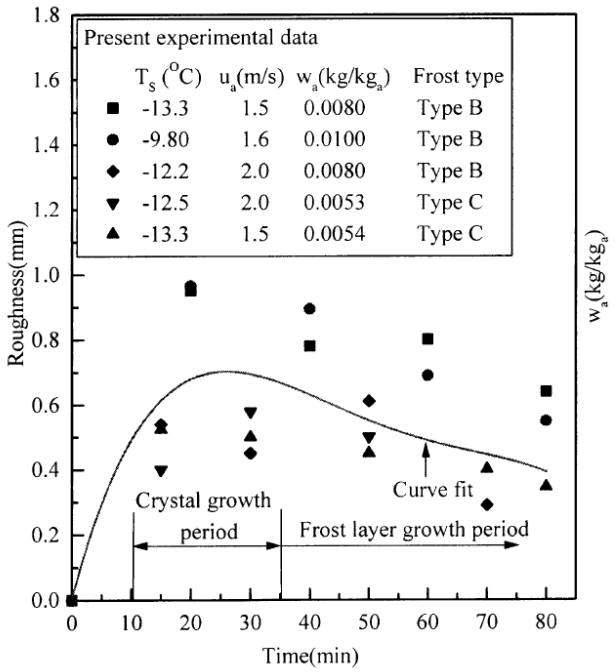

Figure 2.2: Yun' Frost Roughness Measurements over Time [36]

However, Yun's model has limitations as they only considered a limited range of atmospheric conditions and the experimental data had a standard deviations of ±29%. Most critically, the needle point had to come in contact with the frost dendrite. This would most certainly create excessive uncertainty in the results. Additionally, the roughness height was only measured at one specific area on the plate therefore decreasing accuracy as the temperature and air flow may have been slightly different compared to the recorded atmospheric conditions. Furthermore, recording only one measurement eliminates the ability to collect RMS height and skewness, which are important parameters for understanding the full effect of roughness on fluid flow and heat transfer.

In review of the frost roughness measurement techniques conducted by various researchers, it becomes evident that extensive research is still needed. More specifically, a frost roughness measurement method is needed that can quantify frost height in a controlled

environment with minimum uncertainty. This minimum uncertainty is achieved by measuring frost that is not altered in any way from physical contact or variations in atmospheric conditions. Moreover, the atmospheric conditions must be repeatable to demonstrate precision.

Photogrammetry

One of the best methods for measuring frost roughness evolution is through the use of photogrammetry. This claim is supported by the evidence described in the following paragraphs and the validation presented in Chapter Three. Photogrammetry is the science of deriving the spatial and geometrical information of objects through the evaluation of recorded data images [37].

Application

Because depth of field is lost in a two dimensional image, determining surface information is accomplished by capturing multiple perspectives of a surface. The light rays that create the pixels in an image can be intersected and used to calculate height at various location [38]. These multiple perspectives can be captured by moving the camera between images which is a method known as structure-from-motion [39]. An important distinction of photogrammetry is that it functions solely with non-contact optical images, unlike laser scanners [40] or other electromagnetic interferometers [30] which require light beams to be directed at the surface. Because frost can be transparent and/or reflective, photogrammetry can be used with various light setups to optically capture the frost surface with extraordinary detail. Historically, photogrammetry was created for the topographical assessment and aerial surveying of terrain and metropolises [41]. By tracking the location

of where images were captured from an aircraft and interspersing survey targets on the ground, the elevation at every point could be measured. Today, close-range (non-topographic) photogrammetry is used in a vast range of fields including archaeology, bioengineering, mechanical inspection, plant engineering, ship construction, and computer animation. The same concept is applied except the camera is moved and rotated so that different perspectives are captured around the object. Figure 2.3 depicts this movement of the camera with the resulting perspective change of feature points on an object of interest.

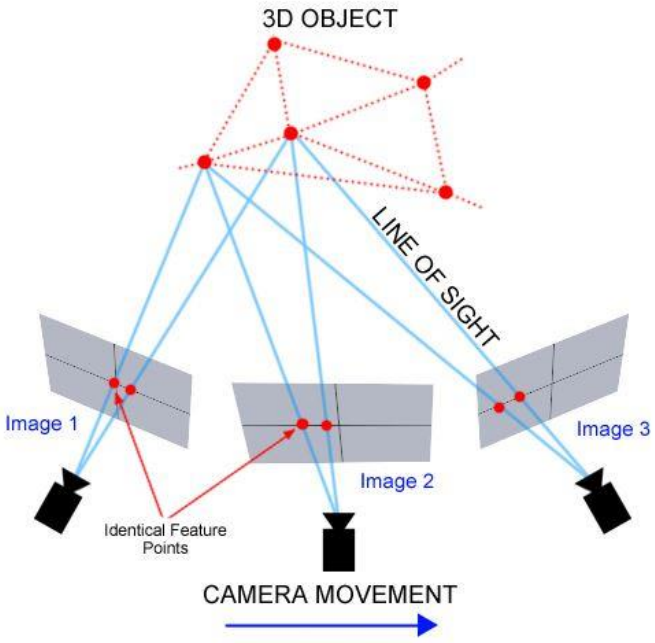

Figure 2.3: Photogrammetric Structure from Motion [42]

Additionally, photogrammetry has been used in the aerospace industry for measuring geometrical and physical quantities. Liu et al. [43] describes photogrammetric techniques for measuring position, shape, size, aeroelastic deformation, and dynamics of objects such at rotating blades, aircraft, space structures and wind tunnels. In the measurement of deformation or dynamics, a single-view camera orientation may be

established to assess the movement of a structure or object. However, a single camera view is insufficient for measuring frost roughness evolution because the full development of frost may take several hours. On the other hand, there is a certain type of structure measured with photogrammetry and has several similar features to frost, called gossamer spacecraft structures [44]. Gossamer structures are fragile, reflective structures such as solar sails, large membrane reflectors, and thin-film solar arrays. Photogrammetry is ideal in measuring structures like these because it is noninvasive, offers the simplicity of capturing images with an off-the-shelf digital camera and results in excellent measurement precision. With any photogrammetric model, targets must be placed on the surface or object of interest to utilize known measurements for scaling the photogrammetric model. Because physical targets used in traditional photogrammetric setups could potentially damage the membranes in measuring gossamer structures, laser-induced fluorescence projections are the best alternative to generate targets. These lasers create grid patterns on the surface, resulting in a photogrammetric setup that has no physical contact.

Surface Roughness

There are a limited number of studies when photogrammetry has been used to measure surface roughness from accretion contamination. Collier et al. [45] utilized close range photogrammetry for three dimensional modeling of ice on an airfoil because it premises upon non-contact, global measurements, enables flexibility in capturing data in tight fit areas, and has the ability to capture the time accretion. Flat targets were placed on the airfoil and a stereo pair of images were used to calculate camera positions before the start of the test. Images captured from these positions along with the reference of the clean airfoil were used in determining the distortion of the iced surface. Post processing was

performed with a geographical analytical plotter that created a photogrammetric model. Although Collier's results were not highly accurate, his method of placing targets inside the wind tunnel for the entire duration of the test was intuitive for establishing a noninvasive measurement process. He concluded that photogrammetry is the most advantageous method for measuring ice accretion because it allows maximum data acquisition in the shortest amount of time and at minimal cost.

More recently, Soinne et al. [46] compared a photogrammetry technique to NASA's [22–26] established laser scanning method by measuring frost on an aircraft wing. The frost was generated in the method as described previous for Koivisto [47]. Once frost had formed, a small target was laid upon the frost and a total of 47 to 54 images at different orientations were captured around the target. However, reorienting the camera between captured images required up to one hour for the total set of images, which is an excessive time resulting in definite frost variation. The other method, laser scanning, utilized a robotic arm that tracked the location of the scanner as it measured the frost and only required ten minutes of data acquisition. The difference in average frost thickness between the two methods was 0.5 mm, indicating significant errors in possibly both data acquisition processes. Although the laser scanning entailed less time, this was still not sufficient for capturing frost accretion, as frost dendrites will significantly change in 10 minutes. Additionally, in both methods the researcher had to stand within the wind tunnel to adjust the scanner and the camera. This presents uncertainty in the air temperature which will alter the frost surface from the convective heat of the researcher. Furthermore, the procedure of stopping the wind tunnel for data acquisition does not suffice for this present study because a transient measurement of frost roughness is the desired outcome.

Although photogrammetry is the best method for obtaining surface measurements in a brief time and noninvasively, the situation of modeling a frosted surface to the correct scale, presents several unique challenges. The challenges revolve around frost being transparent, diffractive, miniscule, fragile, and temperature sensitive. These characteristics void the traditional techniques discussed for target placement. Since the frost is miniscule, fragile and temperature sensitive it is much more prone to alteration from slight variations in air temperature or residual heat from a target being placed beside the frost. Therefore, Soinne's [46] technique of placing a target on top of the frost presents too much uncertainty for this study. Furthermore, using a laser projection for target placement in a similar fashion to the gossamer structures [44] does not suffice because of the diffraction and transparency of the frost scattering the laser-induced fluorescent light. Due to the challenges of evaluating frost formation, to conceptualize and create a highly accurate, photogrammetric frost measurement technique, the fundamental computations of a photogrammetry algorithm had to be understood. Once this was comprehended, minimizing error and determining the best method for obtaining a scaled photogrammetric frost model from non-invasive targets could be performed.

Fundamental Mathematics of Photogrammetry

Image Orientation

The computational foundation of photogrammetry is the perspective projection transformation, which establishes the correlation between the three-dimensional object space and the two dimensional image plane [48]. Referring to Figure 2.4, the data input to a photogrammetry algorithm or software is at least two images (P_1, P_2) from which the

algorithm will determine each photo's six degrees of spatial orientation (three translational and thee rotational) based off of at least one known object point location (R). These point locations are selected on each image (r_1,r_2) either manually or autonomously by the photogrammetric algorithm.

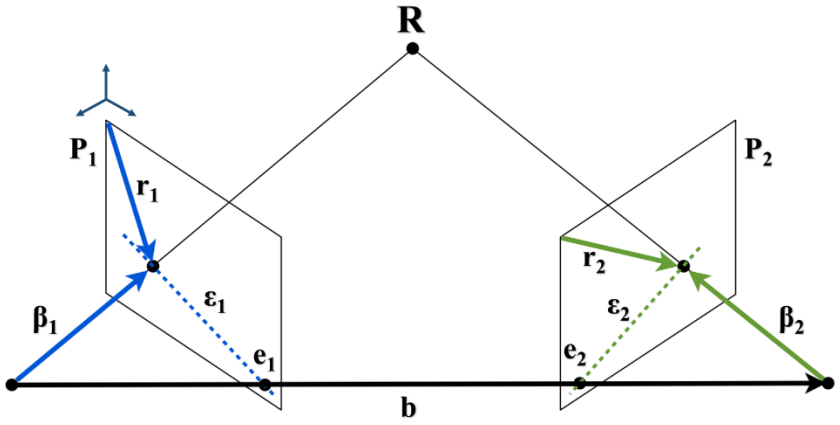

Figure 2.4: Coplanarity Constraint of Two Images P1 and P2.

The fundamental concept that drives the orientation of the photos is the coplanarity (or epipolar) constraint [48]. This constraint requires that for two corresponding pixels (r_1,r_2) on two different images (P_1, P_2), there are two corresponding rays (β_1, β_2). The intersection of these rays must meet at the object point location R. From these rays, a plane can be created that constrains the images to each other by ensuring that two other corresponding pixels e_1 and e_2 are along the same line, b. From a mathematic standpoint, r_1, r_2, e_1, and e_2 are elements in the 2D matrices P_1 and P_2 that must lie along corresponding epipolar lines ε_1 and ε_2. The vectors β_1, β_2, and b are vectors in Euclidean coordinates that must lie along the same plane. The coplanarity constraint therefore requires:

$$\beta_1 \cdot (b \times \beta_2) = r_1^T \varepsilon_1 = 0 \quad (2.4)$$

After applying the above constraint, the photos are oriented and can be described through a perspective projection matrix *P* that transforms the two-dimensional image plane to three-dimensional object space. In a general sense, the images (composed of thousands of pixels) have now been oriented in 3D space. It is very important that the perspective projection matrix is as accurate as possible to the true physical orientations of the camera because it affects the global error. To increase this accuracy, the selection of pixels r_1 and r_2 that correspond to R affect the accuracy of the alignment process and ultimately the generation of the dense point cloud [49]. From a physical perspective, the accuracy can be improved by initially knowing the spatial orientation of the cameras and validating the image orientations with the coplanarity constraint. If it is unfeasible to physically measure the camera orientations, accuracy may be increased by ensuring that well defined targets are in the images. A superfluous constraint may also be applied to further increase accuracy called the trifocal constraint [48]. This constraint is similar to coplanarity constraint, but exists between triplets of images with a vector that connects all three images in the same way as vector b.

Dense Point Cloud Generation

After determining the 3D orientation of all images, an algorithm begins scanning every image and determining if it can recognize matching features between images [50]. If the program identifies a feature, it refines the scan and incurs an estimate on exactly which image pixels (r_1,r_2,r_3…) correspond to an unknown object point location (R). Application-wise, the accuracy of the correctly matched pixels can be increased by ensuring that high

quality, heavily detailed images are captured and by taking multiple images. After this identification process, the positioning of object points operate on the basis of triangulation [48]. Since the pixels in each image have been spatially oriented, corresponding pixels between images are used to triangulate object point locations. In this context, triangulation operates on the collinearity constraint which implies:

$$([r_i] \times Pp_i)\, R = 0 \tag{2.5}$$

In the equation, Pp is the perspective projection matrix for each image, found previously in the image orientation process. Vertically concatenating the equations leads to a system of equations used to solve for the object point location R. For only two camera images, the resulting solution is unique. For more than two cameras, a method of least squares must be utilized. It is beneficial to take more than two images of a specific area of interest because this will smooth out the errors through the use of the least squares method. Once all identified object point locations have been calculated through the collinearity constraint, the resulting sum is a dense point cloud representing an object's surface.

Tilt Distortion

As described in the alignment of the photos, a photogrammetry algorithm can calculate an image's six degrees of freedom. However in the case of a flat surface, the angular tilt of the camera alters the perspective characteristics of the image [43] as portrayed in Figure 2.5. This perspective change makes it much more difficult to derive the camera orientation in the photo alignment process.

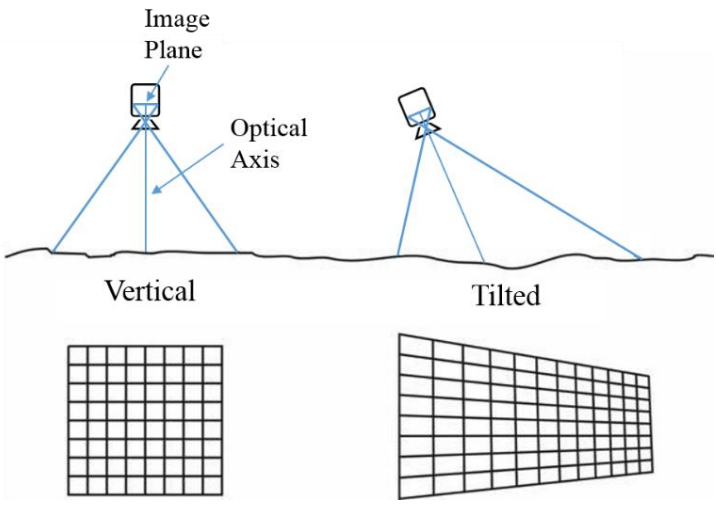

Figure 2.5: Angular Roll of a Camera Resulting in Tilt Distortion

Furthermore, this tilt distortion causes error in the positioning of object points for the generation of the dense point cloud as described in Figure 2.6. The principal point is the location where the optical axis intersects the ground. The nadir is the point vertically beneath the camera. For a tilted image, the displacement (d) at the point of interest can be calculated in the photogrammetric algorithm, but there is a much larger uncertainty compared to photos parallel with the surface.

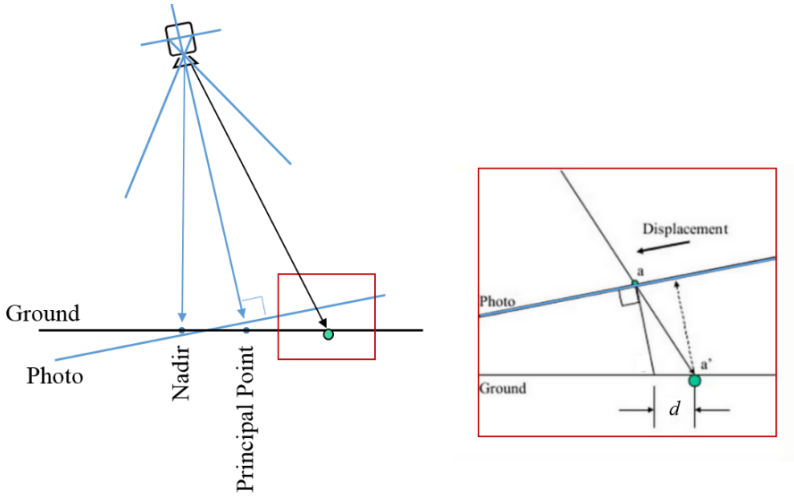

Figure 2.6: Tilt Distortion Resulting in Displacement Uncertainty

If an image is taken so that the nadir and the principal point are at the exact same location, then the photogrammetry algorithm does not have to correct for perspective change (d). This eliminates the need to calculate two rotational degrees of freedom. The perspective projection matrix has the smallest magnitude of error for perfectly vertical images because of a smaller buildup in displacement uncertainty. Because frost is a highly complex, crystalline structure, reducing the buildup in uncertainty is essential for the photogrammetry algorithm to compute the frost surface correctly.

Surface Roughness Analysis

Once a surface is measured, roughness analysis is the detailed modeling of surface spatial geometries and variations. The two primary parameters that are needed to analyze a surface statistically are root-mean-square (RMS) height and skewness [51]. From these parameters, an empirical formula may be used to predict the relevant aerodynamic roughness.

Surface Statistics

RMS height represents the standard deviation of height from the mean surface value. As described in Eq. (2.6), it is the square root of the sum of the squares of each element's distance from the mean surface. In the following equation, A is the mean surface, Z is the distance from the mean surface, and x and y are the ordinate values.

$$R_q = \sqrt{\frac{1}{A}\iint Z^2(x,y)dxdy} \tag{2.6}$$

Skewness is a dimensionless value that represents the symmetric distribution of the surface as shown in Eq. (2.7). A negative skewness indicates a surface composed of

ravines, whereas a positive skewness signifies a surface primarily composed of peaks or frost dendrites. A surface with an even distribution of peaks and valleys has a skewness of zero.

$$Skw = \frac{1}{{R_q}^3}\left[\frac{1}{A}\iint Z^3(x,y)dxdy\right] \tag{2.7}$$

Additional parameters that are relevant to surface statistics include maximum peak height and maximum valley depth. As defined by name, maximum peak height and maximum valley depth are measured from the mean surface height. Therefore, the overall maximum height parameter (commonly referred to as peak-to-valley) is defined as the sum of the maximum peak height and the absolute value of the maximum valley depth.

Predictive Method

Based solely off of surface statistics, Flack and Schultz [52] determined a method to predict the equivalent sand-grain roughness height of a surface. Upon reviewing the work of Nikurasde [53] and Schlicting [32] in flow fields in the fully rough regime, Flack and Schultz built upon their research by incorporating equivalent sand-grain roughness heights as the roughness scale. The study analyzed the relationship between equivalent sand-grain roughness heights and physical roughness statistics for a range of three-dimensional surfaces. The results proved that the most effective surface parameters to characterize a surface are the skewness and RMS height. From these parameters, a correlation was created to predict equivalent sand-grain roughness height:

$$k_s = 4.43R_q(1 + Skw)^{1.37} \tag{2.8}$$

The application of the equivalent sand-grain roughness is very advantageous in the field of aerodynamics. From the equivalent sand-grain roughness height, a prediction of the frictional drag coefficient (C_f) can be resolved by using boundary layer similarity scaling. The overall frictional drag coefficient can be determined as a function of equivalent sand-grain roughness height divided by the distance from the start of the boundary layer to the location of interest (L). Many functions for the variation of skin friction with boundary layer location are available. An example function is presented by Flack and Schultz [52] and shown in in Eq. (2.9).

$$\sqrt{\frac{2}{C_f}} = -2.186\, ln\left(\frac{k_s}{L}\right) + 0.495 \tag{2.9}$$

Aerodynamic Effects of Frost Formation

Aerodynamically, the third stage of frost growth is the most crucial to the scope of this research because of the subsequent increase in friction. Increased drag occurs from the fluid motion sticking to the rough crystalline structure resulting in an increased wall shear stress (τ_w) as defined in Eq. (2.10). The equation presents the relationship of a wall shear stress to the dynamic viscosity of a Newtonian fluid multiplied by the velocity gradient at the wall [1].

$$\tau_w = \mu \frac{\partial u}{\partial z}\bigg|_{z=0} \tag{2.10}$$

Wall shear stress can be non-dimensionalized to obtain the skin friction coefficient (C_f). Eq. (2.11) describes this relationship between the skin friction coefficient and wall

shear stress, where ρ is the fluid density and U_∞ is the freestream velocity. The increase in the skin friction coefficient will cause an increase in the parasitic drag.

$$C_f = \frac{\tau_w}{\frac{1}{2}\rho U_\infty^2} \tag{2.11}$$

Similarly, frost dendrites will cause perturbations in the flow, initiating a trip in the boundary layer resulting in an earlier transition from laminar to turbulent flow compared to a clean wing. Figure 2.7 demonstrates this effect and the origin of a stall at smaller angles of attack. Furthermore frost roughness could potentially result in leading or trailing edge separation flow which results in a reduced stall margin. The combined effects of frost roughness increasing wall shear stress and perturbations lead to a decrease in aerodynamic performance. Conclusively, measuring frost roughness is crucial to understanding its magnitude of aerodynamic degradation.

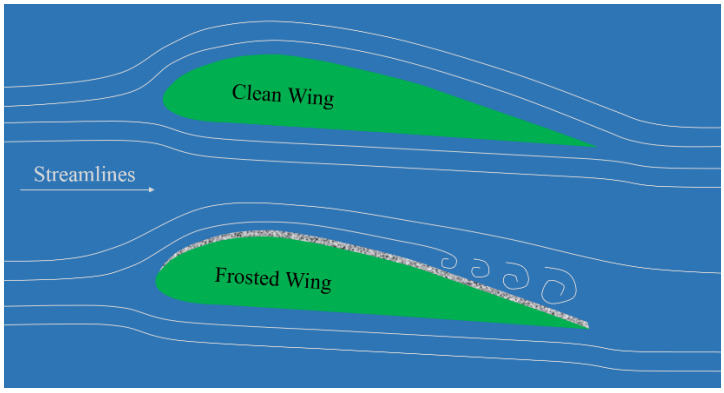

Figure 2.7: Turbulent Flow Caused by Frost Contamination on an Aircraft Wing

Based on the atmospheric conditions, thermal boundary layer and velocity boundary layer, the frost will vary in thickness and roughness [10]. Theoretically if a frost dendrite reaches a height in the thermal boundary layer that is above 0 °C, then that frost

pinnacles will melt back into the crystalline matrix causing the density of the frost to increase and therefore reducing the roughness [54]. Figure 2.8 demonstrates a frost layer that has reached its maximum height due to the thermal boundary layer. The velocity distribution is also presented because it affects the thermal boundary layer and the frost formation. Cheng and Wu observed this by noting that an increase in air velocity resulted in an increase in the frost density [55]. This phenomena has become known as the remelt or the redensification phase in frost formation [18]. While the focus of this initial effort is simply on measuring frost roughness, understanding the various boundary layers and redensification phases that result from the measured frost roughness values is the ultimate goal of the complete research project.

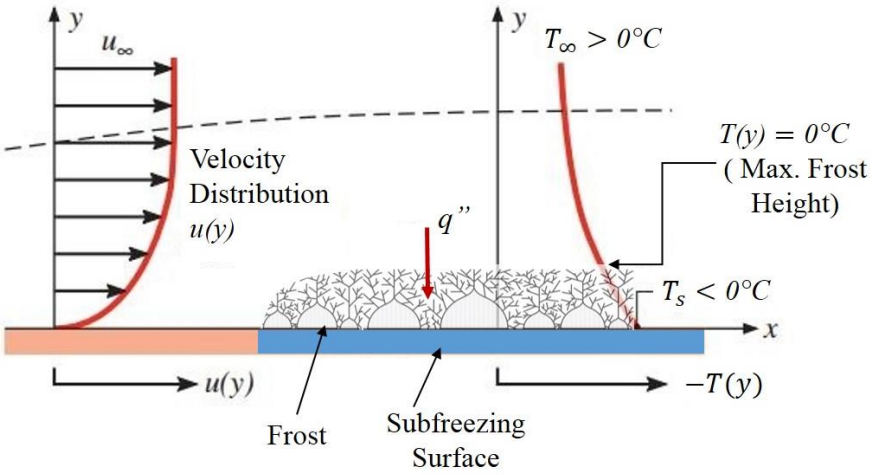

Figure 2.8: Boundary Layer Limiting Frost Height

Aerodynamic Tests of Frost Roughness

In some circumstances, researchers have skipped the measuring and modeling of frost roughness and instead directly approached the aerodynamic impact. This approach was not pursued in this study because of the need to build a frost roughness database that

can be used to model and predict frost roughness on cold-soaked frosted wings in various environmental conditions. In addition, the method and results from this research could potentially be applied to other industrial applications such as cryogenic fuel tanks or heat exchangers. Nevertheless, understanding the magnitude of impact that frost roughness has on the takeoff of an aircraft is imperative to the initial motivation behind this study. Frost roughness may decrease the lift and stall margin, thereby reducing the safety of an aircraft's takeoff.

In 1982, Boeing developed an experimental program to evaluate the impact of frost on the stall characteristics, climbing performance, drag and lift of several 700 series aircraft [33]. An anti-slip adhesive material with a layer of epoxy potting compound was applied to wing surfaces and roughened with a textured paint roller. Three roughness heights were applied and tested: 0.36mm, 0.76mm, and 1.27mm. The results demonstrated significant reduction in climbing performance and maneuverability. On the other hand, the results also portrayed that an aircraft with surface contamination could increase stall angle by taking-off at faster speeds than normal. This was performed without any warning from the stick-shaker stall warning. In the conclusion of the report, Boeing conveyed that aircraft with wing contaminations could sustain acceptable safety margins at takeoff with faster speeds and smaller angles of attack.

Another takeoff analysis came from Dietenberger [56] who combined the computations of aerodynamic penalties of surface contaminations with the steady flight equations. He developed an empirical relationship to demonstrate the effects on drag (ΔC_d), lift ($\Delta C_L/C_L$), and angle of attack ($\Delta\alpha/\alpha$). Specific results were calculated for a single-engine, aircraft with a NACA 64A215, 20-deg flaps wing section. The aircraft parameters

consisted of an unfrosted weight of $W_c = 3100\,lb$, a velocity parameter (V_c) of $\left(\frac{\rho_a S}{2}\right) V_c^2 = 2608.2$ (where S is the wing surface area and ρ_a is the air density) an airfoil chord length of $C = 4.91\,ft$ and a fuselage length of $l = 25.28\,ft$. Additionally, two degrees of coverage (P) were calculated with three different estimated frost roughness heights (k_s). The aerodynamic penalties for this aircraft are presented in Table 2.1.

Table 2.1: Results of Takeoff Analysis for Single-Engine Aircraft [56]

k_s (mm)	P	$\Delta C_L/C_L$	$\Delta\alpha/\alpha$	ΔC_d	$\alpha_{takeoff}$ (deg)
1.0	1.0	0.333	0.241	0.0274	4.69
0.5	1.0	0.304	0.220	0.0214	4.93
0.1	1.0	0.237	0.172	0.0096	5.49
1.0	0.95	0.182	0.132	0.0226	5.95
0.5	0.95	0.161	0.116	0.0176	6.13
0.1	0.95	0.111	0.080	0.0078	6.54
Clean Wing	1.00	0	0	0	7.475

$W_c = 3100lb;\ \left(\frac{\rho_a S}{2}\right) V_c^2 = 2608.2;\ C = 4.91ft;\ l = 25.28ft$

The results portray that the maximum lift coefficient of loss may be as high as 33.3% and the maximum angle of attack loss may be as high as 24.1%. Dietenberger concluded that both small and large airfoils could experience significant loss in lift. Conversely, he also concluded that safe takeoff margins could be obtained. This could be achieved by reducing the weight of the aircraft proportionally to the maximum lift loss. However, Dietenberger only advised this in the event of an emergency or in a military environment. The calculations were informative, but equivalent sand-grain values were never truly measured which are critical to determining the exact aerodynamic penalties. Therefore, it is imperative to measure frost roughness parameters at known psychrometric conditions, in order to predict sand-grain roughness on an aircraft in various atmospheres.

Kind [57] demonstrated that frost near the leading edge of a wing section has the most significant degradation to the lift of an aircraft. Kind performed experimental tests in a wind tunnel with frost models obtained in the same process as Lawrysyn [33]. The boundary layers were experimentally measured from the frost models and incorporated into a computer program that could apply the measurements to an airfoil. The surface roughness was computationally applied at various degrees of chord from trailing edge to 1% chord of the leading edge. The results in Figure 2.9 show that with a 99% coverage condition (1% to 100% chord) the lift and drag performance dramatically degraded due to the thickened boundary layer which increased the location of flow separation. The lift coefficient decreased by approximately 50% for an angle of attack of 16 degrees.

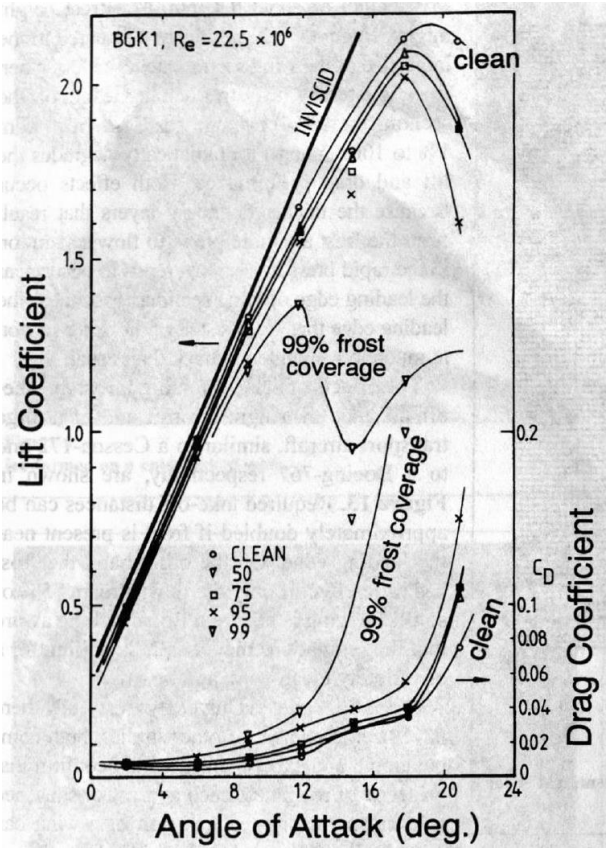

Figure 2.9: Predicted Lift and Drag of an Airfoil with
Various Degrees of Frost Coverage on the Upper Surface [57]

With knowledge of Kind's roughness analysis on the upper surface, Bragg [58] assessed the lower surface of an airfoil in NASA's Low-Turbulence Pressure Tunnel using flight Reynolds numbers. Bragg simulated frost roughness with ballotini beads applied with an adhesive to the bottom of a supercritical high-lift airfoil model. The beads were air-pressure sprayed onto a thin-film, fast-drying adhesive paint. The roughened surface was then photographed and the beads were counted to determine the roughness density. At full scale, the roughness height was 0.016 inches with a density of 30 beads/in^2. The airfoil was placed in the wind tunnel to determine the lift to drag ratio. Similar to Kind's result, Bragg concluded that underwing frost has the most detrimental effect on an aircraft when it is near the leading edge. For frost coverage starting at the 12% cord, the maximum change in lift coefficient was 4.8% compared to a clean surface wing.

Most recently, Koivisto [47] tested a common research model (CRM) wing embedded with glycol coolant tanks chilled with cooling circuits. The wing was tested in a chilled wind tunnel with ambient conditions derived from outside winter conditions in Helsinki, Finland. Koivisto measured the lift of the frosted wing model and compared it to that of a clean wing. Although this method obtained useful information, the results were unrepeatable due to the varying outside conditions. Furthermore, the results do not present any characteristics or specific measurements of the frost at various psychrometric conditions, therefore removing the potential of creating a frost roughness model.

Summary

In review of the technical background, various frost formations may procure on a surface depending on air temperature, relative humidity, surface temperature, and air velocity. Determining the frost roughness is critical in the area of frost contamination on

aircraft wings as any surface roughness will degrade the lift and angle of attack of an aircraft. No research has been performed to date, that accurately measures transient frost roughness parameters: RMS height, skewness or equivalent sand-grain roughness which are important for aerodynamic analysis. This research has assessed a new method for measuring frost roughness using a photogrammetric technique. This photogrammetric approach is based on structure-from-motion algorithms traditionally employed in aerial surveying. The use of photogrammetry is supreme for measuring frost roughness because it is non-invasive, not heavily time dependent, in-situ, and captures global measurements. However the one drawback to this method is the requirement of scaling the photogrammetric model using targets placed in the camera's view of focus.

CHAPTER THREE

Materials and Methodology

To investigate the transient surface roughness of cold-soaked frost formation at various atmospheric conditions, an experimental method was conceptualized and established. The experimental procedure used a cold-soaked plate in a psychrometric wind tunnel and photogrammetric data acquisition method. This chapter describes the experimental devices and procedures employed. Additionally, the design and construction of experimental apparatuses specific for these tests is described in detail. This section also includes the data reduction process to calculate RMS height, skewness, overall maximum height and equivalent sand-grain roughness. The chapter concludes with validation of measuring frost roughness using the photogrammetric method.

Experimental Wind Tunnel

To study frost formation, the Baylor Frost Tunnel was designed and fabricated by Dooley [12] with the ability to vary air temperature, humidity, velocity and surface temperature. The tunnel provides steady-state, conditioned airflow over a test surface flush-mounted to the bottom side of a test section. Attached underneath the test surface is a thermal stage which controls the test surface temperature with high precision. The tunnel involves two main components: a closed-loop psychrometric wind tunnel and a data acquisition and control system (DACS).

Psychrometric Wind Tunnel

The air conditioning system of the wind tunnel contains five main mechanisms: an adjustable-speed blower, a humidification system, two cooling coils, an electric reheat module and a dry gas injection system. These components are housed in discrete modules as shown in Figure 3.1. The modules are constructed from rigid insulated duct board and sealed together with soft foam gasket material. The motivation behind the module concept is to facilitate each element and to isolate the most vibration prone components (specifically the blower and humidifier) from the test section. Vibration to the camera and test section is further reduced by the presence of a vibration isolation table.

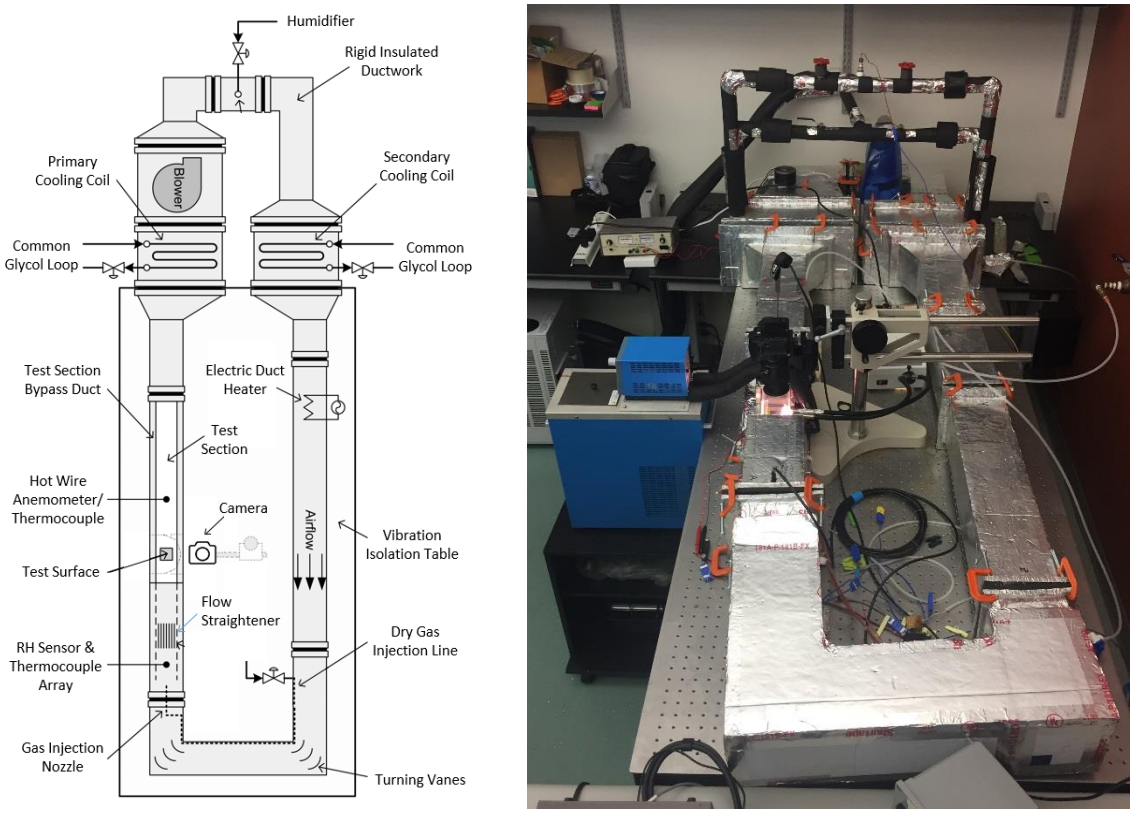

Figure 3.1: Overview of Psychrometric Wind Tunnel

A 120 VAC centrifugal blower drives air through the entire wind tunnel while manually controlled with a silicon-controlled rectifier (SCR) controller. Rubber isolators attenuate vibrations from the blower. The blower is capable of providing air velocities from 0.2 to 10 m/s in the test section

The primary method for adding moisture to the airstream is through injection of cool mist. The moisture is sourced from an ultrasonic, dial-adjustable humidifier with a water reservoir of 3.5L. The humidifier is equipped with a ceramic filter. For air velocities and air temperatures of interest for this research, the maximum output of the humidification system is a bulk air stream relative humidity of 91% for more than 4 hours.

Downstream and upstream of the blower and humidifier are crossflow cooling coils provided with a single-phase glycol/water mixture reservoir. The chiller can produce temperatures of -5 °C while maintaining bulk air stream temperatures as low as 3 °C for air velocities at 3 m/s. Standard laboratory-grade globe valves and rotameters control the flow rate to each cooling coil, which ultimately control the coolant-to-air temperature at each heat exchanger. The unique design of the dual coil is the capacity to cool downstream of the humidifier on demand, thereby making it possible to increase the dry bulb temperature without increasing humidity or vice versa.

The reheat module provides sensible reheat addition to increase dry bulb air temperature if necessary. This module is located directly downstream of the second cooling coil and contains a 120VAC, 500W electric duct heater. A 9-element thermocouple array at the inlet of the test section provides input to the heater through a programmable Red Lion Model controller. The reheat module was rarely used except for testing conditions with air temperatures above 15 °C.

Depending on the particular test conditions, humidity can be reduced by injecting conditioned gas directly into the wind tunnel. This moisture trim module is located immediately upstream of the test section and pumps zero-grad nitrogen (N_2) into the wind tunnel chamber. The dry gas system contains an inline pressure regulator, a gas injection line that runs parallel to the airflow and a nozzle that releases the gas co-linearly with the centerline of the test section inlet. This design allows for isothermal dehumidification with fine control at lower humidity levels.

Test Section

The central component to the wind tunnel is the test section module. Within the module there are two parallel ducts: a test duct with a thermal stage and a bypass duct (Figure 3.2). At the entrance of the test section, the airstream is split in half by a partition. In the top section, a portion of the air enters the test duct through an annular design. The remainder of the air returns to the bypass duct through a break in the partition. This annular design insulates the entry region of the test duct while preserving a uniform air temperature over the test plate. The bypass duct ensures a sufficient airflow over the dual cooling coil, for a wide range of air velocities over the test plate.

At the entrance of the test section, a duct-mounted relative humidity sensor and 5-element thermocouple array measure and record the air conditions to a NI LabVIEW program [12]. Just within the test duct is a bank of 1.5 mm diameter and 20 mm long flow straighteners. The test duct is manufactured out of acrylic glass panels fused together with dichloromethane. An optical view port for capturing top-down photographs is machined out of the acrylic panel and allows for in-situ data acquisition. A double pane of optical quality, 0.17 mm thick glass is sealed over the view port to ensure clarity for viewing frost

while preserving the air temperature. Downstream of the test surface a hot wire anemometer calibrated for measuring the air velocity.

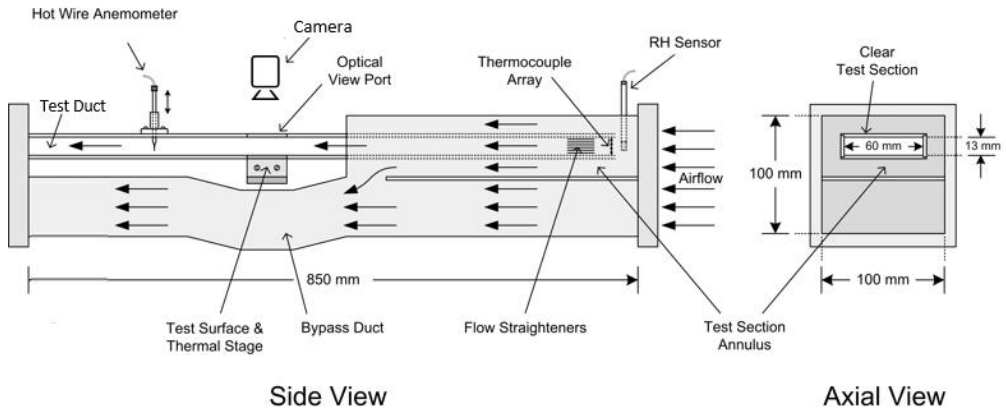

Figure 3.2: Detailed Schematic of Test Section Module

The thermal stage used to control the surface temperature is comprised of a copper heat sink, a Peltier module, a thin-film heat flux gage, a thermocouple and a test surface [12] as shown in Figure 3.3.

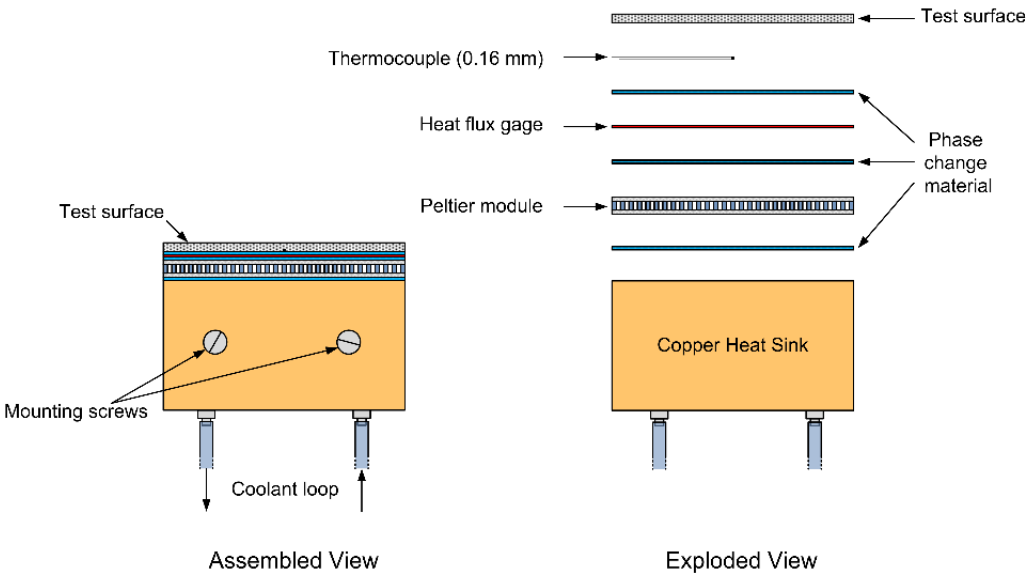

Figure 3.3: View of the Thermal Stage [12]

The thermal stage is secured with mounting brackets and placed so that the test surface is flush to the bottom of the test section. The aluminum test surface is 30 by 30 mm with a thickness of 0.67 mm. The heat sink contains an internal serpentine conduit and is machined out of copper to maximize heat transfer. A small chiller with a cooling capacity of -15 °C provides a propylene glycol/water mixture as a coolant to the heat sink. The Peltier module increases the cooling capacity of the thermal stage with a commercial-grade 36W thermoelectric cooler regulated by a DC power supply. The module can also be used for heating the surface through the use of an electromechanical switch that changes the polarity of the power supply. The heat sink and Peltier module combination are capable of sustaining surface temperatures of -25 °C. On top of the Peltier module is a thin film heat flux gage used to measure instantaneous heat flux (q'') through the thermal stage. Additionally, a small type-T thermocouple is used to measure the bottom side temperature (T_b) of the test surface. The data acquisition and control system use these two measurements to calculate the upper surface temperature (T_s) in real time using the plane wall conduction formula as shown in Eq. (3.1). From this calculation the DACS software controls the Peltier module to ensure a constant temperature is sustained throughout an entire test.

$$T_s = \frac{q''\Delta y}{k} + T_b \tag{3.1}$$

The thermal stage components are bonded with a thermally conductive phase change material (PCM). At temperatures above 52 °C the PCM is a viscous fluid that can easily be applied between interfaces. Once the thermal stage is assembled and the phase change material has cooled in temperature, the PCM solidifies and holds the components

together with good thermal conductivity. A distinct advantage of the phase change material is the elimination of external clamping or permanent adhesives. Furthermore, the PCM dismisses the potential of surface contamination compared to other adhesives such as thermal grease.

Data Acquisition and Control System

A multichannel data acquisition and control system for the wind tunnel include National Instruments hardware and software created by Dooley [12]. The hardware's interface with the instrumentation was managed by two modules: an 8 channel cFP-AIO-610 analog input/output module and an 8 channel cFP-TC-120 thermocouple module. These modules are connected to an NI Compact FieldPoint cFP-1804 controller. From a dedicated Ethernet cable, the controller managed a data acquisition and control program developed in NI LabVIEW as shown in Figure 3.4.

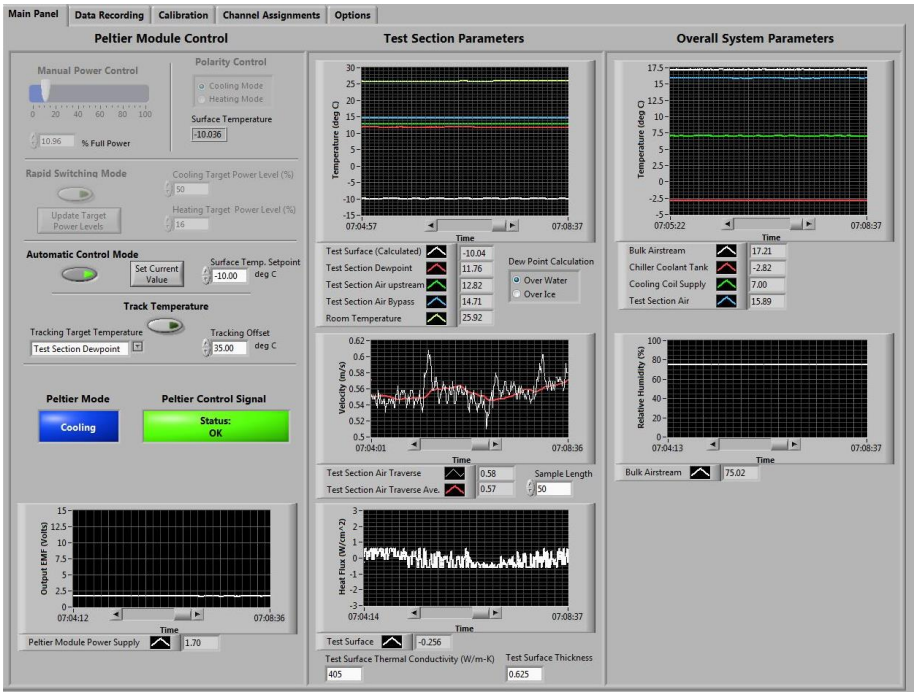

Figure 3.4: NI LabVIEW Data Acquisition and Control Panel

Instrumentation

To measure temperature, humidity and velocity, several specific instruments were equipped to the psychrometric wind tunnel [12]. A TSI model 1750 constant temperature anemometer and 1201 hot film probe measured the air velocity in the test section. Type-T thermocouples (copper-constantan) measured multiple wall and air temperatures along the wind tunnel to ensure that the heat transfer had reached steady-state conditions during testing. An Omega Engineering HFS-4 thin-film heat flux sensor was used in the thermal stage to calculate surface temperature. A Vaisala HMT333 duct-mounted thin film capacitive relative humidity sensor measured moisture entering the test section. Additional parameters that were measured include the voltage of the Peltier module, the temperature of the heat sink and the temperature of the dual cooling coils. These parameters were tracked for control and diagnostic purposes only.

The DACS software is equipped with a standard polynomial calibration curve for all instruments used. The hot wire anemometer was calibrated in-situ with a TSI 8346 VelociCalc thermal anemometer probe. The thermocouples were calibrated in a glycol reservoir with a NIST-traceable 100 Ω platinum resistance thermometer. The heat flux gage and relative humidity sensor were each delivered with a factory calibration certificate. The calibration range and estimated uncertainty of each instrument is listed in Table 3.1.

Table 3.1: Calibrated Ranges and Estimated Uncertainties of Test Instrumentation [12]

Measurement	Calibrated Ranges		Max. Uncertainty
	Low	High	
Temperature °C	-30	50	± 0.2
Heat Flux $\frac{W}{cm^2}$	-9.5	9.5	± 0.06
Air Velocity $\frac{m}{s}$	0	12	± 0.5
Relative Humidity %	25	95	± 1.7

Operating Conditions

The atmospheric conditions selected for the tests were based on historical weather conditions at airports where cold-soaked fuel frost has been an issue. These locations included airports in Dallas, Miami, Houston and Los Angeles [59]. From these records, various air temperatures, humidity levels, air velocities and surface temperatures were selected that the psychrometric wind tunnel was capable of sustaining. Air temperatures were tested at conditions ranging from 10 °C to 16 °C and the relative humidity was set between 61% and 91%. The air velocity was established between 0.5 m/s and 5.0 m/s, because airflow over a stationary aircraft is expected to be at a minimum when cold-soaked fuel frost occurs. Additionally, a surface temperature of -10 °C was selected based on the expected value that cold-soaked fuel laden wings could experience and -25 °C surface temperature was selected as a worst case condition.

Photogrammetric Instrumentation

Photogrammetry was the selected method of acquiring frost roughness because it obtains global, non-contact measurements, captures surface data in-situ, and is minimally time independent. The photogrammetric instrumentation involved a steadily mounted

camera in a top-down orientation above the frosted test surface. The camera was moved in micrometrical increments through the use of a multi-axial traversing system. A sloped scaled bar with high-contrasting object point locations was placed streamwise to the airflow. A halogen light, directed through fiber optic guides, illuminated the frost and the scale bar. Figure 3.5 outlines these photogrammetric components and their integration with the frost tunnel system. The subsequent sections detail each component in the following order: the photography system, the tri-axial traversing system, lighting and the scale bar.

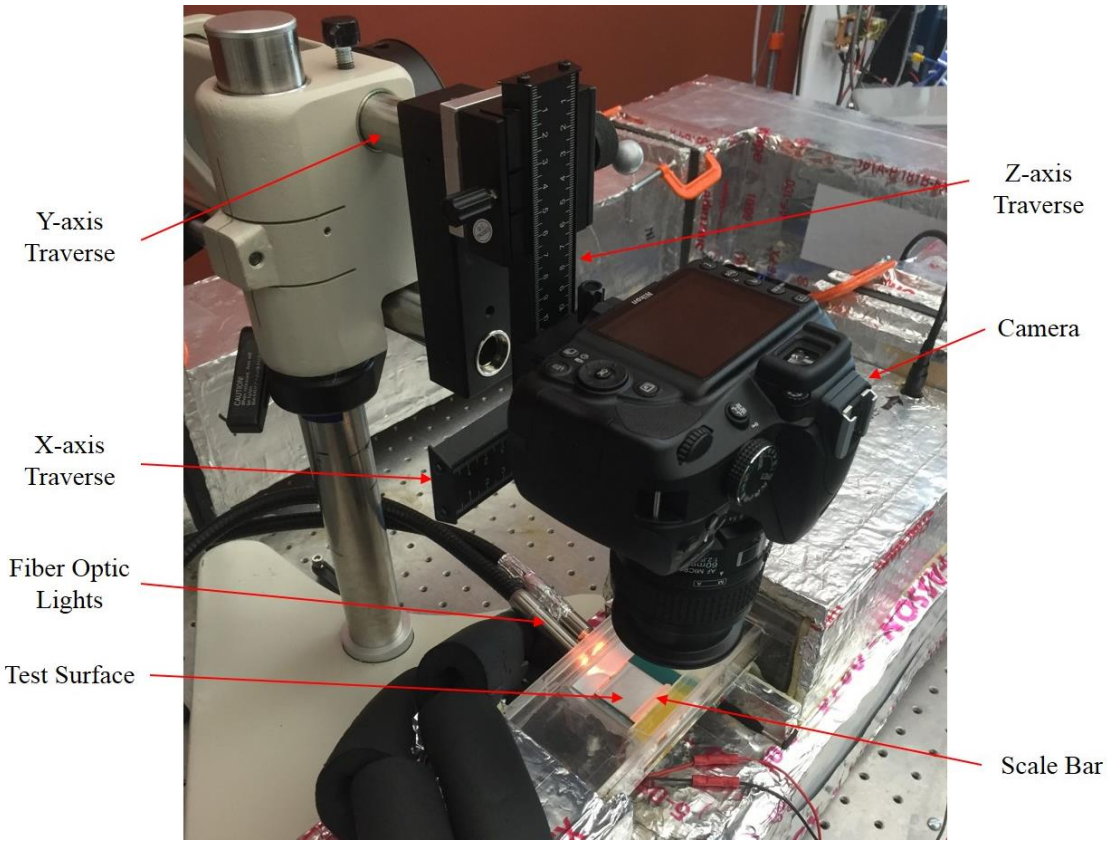

Figure 3.5: Photogrammetric Instrumentation Setup

Photography System

A digital micro photography system provides quantitative data acquisition of the test surface during the entire duration of frost formation. The imaging system includes a

high resolution, 24.2 megapixel Nikon D3400 DSLR camera with an integrated complementary metal-oxide semiconductor (CMOS) sensor. The sensor size is 23.5 mm by 15.6 mm. The camera is equipped with an AF Micro Nikkor 60mm f/2.8D lens. The lens is integrated with close range correction (CRC) and has a maximum reproduction ratio of 1.0x. This maximum reproduction ratio implies that the subject in the plane of focus is identical in size to the image sensor size. A key feature of this lens is the 1.0x magnification with a working distance of 73 mm. The working distance is measured from the front of the lens to the subject in focus and is made possible through the telescopic dynamics of the inner ring as seen Figure 3.6. With a 1.0x reproduction ratio the camera was capable of clearly documenting microscopic details of the frost elements while giving plenty of standoff distance from the top surface of the wind tunnel.

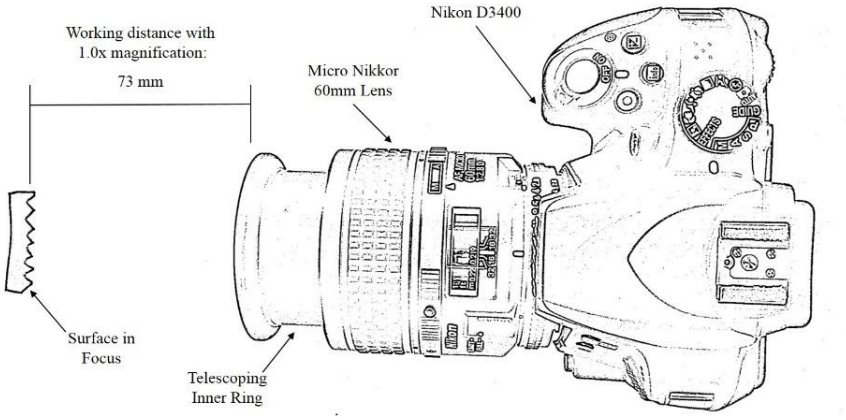

Figure 3.6: Working Distance of Micro Lens

Camera Settings. The lens was set to an aperture of f/22 to provide a large depth of field so that the peaks and valleys of the frost surface were in focus. This resulted in more accurate photogrammetric models. The ISO was set to 200 to reduce noise in the images. This allowed the photogrammetric software to recognize more reference points and

resulted in more detailed models. The shutter speed was varied from 1/30 to 1/200 seconds to ensure that the photos were not underexposed or overexposed. A fixed magnification of 1.0x was used in all images captured because a varying reproduction ratio will increase uncertainty in the photogrammetry calculation due to lens distortion [49].

Tri-axial Traversing System

The multi-axial traversing system incorporated a telescoping boom stand and two positioning slide plates to traverse the camera and to obtain the working distance of 73 mm from the frost surface. Figure 3.7 presents the configuration.

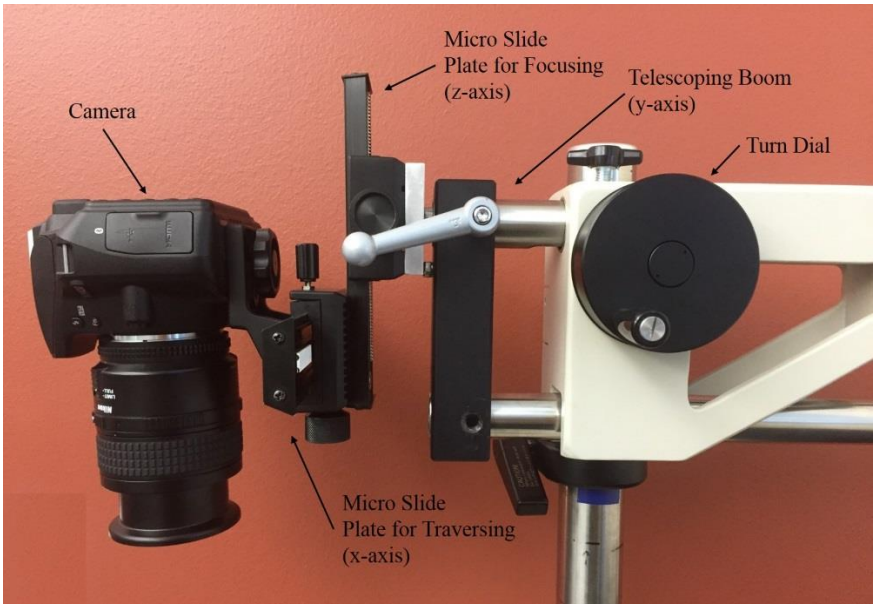

Figure 3.7: Camera and Multi-Axial Traversing System

The boom stand was placed on the active pneumatic frequency isolation table which eliminated any vibration or movement to the camera while pictures were captured. Additionally, the dual-arm boom was equipped with ball bearings and a turn dial to perform smooth traversing motion along the y-axis at quick interval movements between statically

captured images. Each micrometric slide plates utilized a helical gear rack and pinion for small movements. One of the micro slide plates was used to traverse the camera along the x-axis. The other slide plate adjusted the height (z-axis) of the camera to focus the image on the frost surface as the frost thickness increased. The image plane of the camera was parallel with the test surface, to eliminate the computational need for rotational orientation.

Lighting

Lighting was equally important in capturing detailed data. The most critical aspect of lighting was illuminating the frost without any flat light. Flat light illuminates a surface but does not optically present any depth or detail. An example of this is seen in snow covered landscapes when the sun is directly overhead or when the sky is overcast [60]. However when the sun is setting, flat light is non-existent. Therefore in the experimentation, lights were directed along the same plane as the frost, thereby illuminating the frost to clearly depict frost pinnacles and ravines. The light source was from a Nikon illuminator with two 150W infrared-filtered halogen lights directed through fiber optic guides that could be adjusted as the frost height increased. Although halogen lights produce radiation, the fiber optic guides were long enough that negligible heat affected the formation of the frost. This was verified by repeating environmental conditions with the lights on for the entire duration of the test and lights on for only the data acquisition time frame. No significant variations were seen between the resulting frost formations.

Scale Bar

Since the spacing between the images was irregular using the manual traversing system, the camera software had to calculate the camera location for each image. A

reference feature must be present in at least two of the photos to scale the entire model to the correct units. Since targets or markers could not be placed on the frost nor on the metal test surface a microscopic calibrated ruler within the test section was required. Therefore, a scale bar was conceptualized and designed to meet this requirement along with several other requirements. These additional requirements included:

a. The scale bar must be the same order of magnitude in size as the frost. A usable photogrammetric model must be easy to make of the scale bar.
b. The scale bar must have distinct targets to specifying object point locations in the photogrammetry software.
c. The scale bar must not interfere with the airflow in the test section nor accumulate excessive condensation.

The requirement of creating a usable photogrammetric model of the scale bar was increased in challenge by the fact that captured images had to clearly depict details of the scale bar and the frost. This inferred that the lighting, height in focus, detail, and exposure must be satisfactory for the frost and the scale bar at the same time. Because frost thickness increased over time, the height in focus also changed therefore requiring the scale bar to have distinct targets at varying heights. With limited literature in the area of micro photogrammetry target placement, several iterations of design, fabricating and testing occurred. The final product was a simple yet effective triangular prism with a flat topped surface and infinitesimal, permanent targets on a sloped surface. Figure 3.8 shows the scale bar oriented in terms of the test section and an example data image collected of the scale bar and frosted surface.

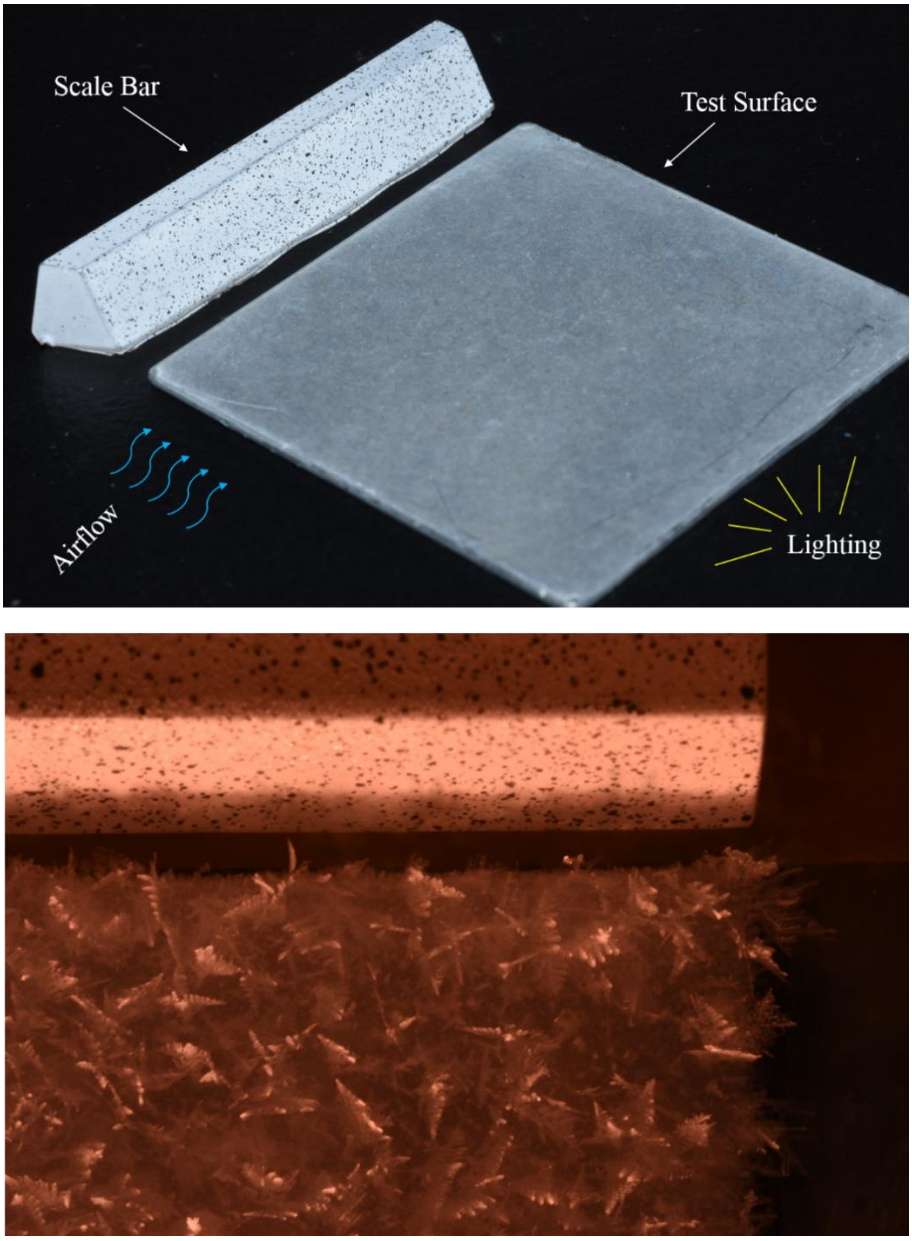

Figure 3.8: Scale Bar Orientation and Example Data Image

Some design outcomes to note about the scale bar included no interference with the frost on the test surface or the airflow influencing frost formation. Moreover, the sloped surface rendered a well-lighted area with microscopic targets at various heights. These targets were easily visible with the correct camera settings as seen in the example data image of Figure 3.8. The top of the scale bar was for leveling purposes discussed later in

the data reduction section. The sloped surface was designed at a steep angle to prevent water droplet condensation, but not to the degree where the camera images could not clearly portray the sloped surface. The scale bar was modeled in SolidWorks and fabricated on a stereolithography FormLabs Form 2 printer with the printer resolution set to 25 μm. The targets were permanently placed on the sloped surface by speckling the white surface with black spray paint specks. The distance between specific paint speck targets was measured using a Keyence VR 3000 macroscope with a tolerance of ± 5μm. This printed triangular prism proved to be a competent microscopic calibrated ruler for photogrammetric measuring.

Experimental Procedure

Wind Tunnel Procedure

The following experimental procedure outlines the steps to obtain steady state psychrometric conditions in the wind tunnel.

1. The wind tunnel instrumentation and National Instruments workstation was powered on for monitoring: surface temperature, air velocity, relative humidity and air temperatures.
2. The wind tunnel was purged with dry nitrogen gas until the relative humidity sensor measured 50%. This verified that no condensation had accumulated in the duct from previous testing.
3. The test surface was cleaned with dry nitrogen gas injected through a nozzle and the Peltier module was set to 20 °C in the NI LabVIEW program. This ensured that frosting did not occur before the test was started.

4. The scale bar was placed alongside the test surface and parallel to the airflow. Next, the view port was sealed with the double pane of optical glass.
5. The thermal stage chiller was turned on and set to a temperature of -10 °C. However the surface temperature remained above freezing because of the Peltier module.
6. The air conditioning chiller feeding the dual cooling coils was turned on and set to the temperature necessary to maintain the desired test section air temperature.
7. The blower was turned on and the SCR controller was adjusted to provide the desired air velocity in the test section.
8. The humidifier was turned on and adjusted to provide the desired relative humidity within the test section. If the relative humidity was too high for the desired conditions, dry nitrogen was injected through control of the inline dry gas pressure regulator.
9. For warmer air temperature testing conditions (e.g. 16 °C) the electric heater was turned on and automated through the Red Lion controller to ensure precise, steady state test section air temperatures.
10. As the recordings of the air temperature and relative humidity leveled off on the LabVIEW program, the humidifier, air conditioning chiller, and/or the dry-gas injector and duct heater were adjusted to reach the desired steady state conditions.
11. The time required to reach steady state conditions generally required one hour.
12. Once the air temperature, relative humidity and air velocity had reached steady state conditions, the Peltier module temperature was changed in the LabVIEW program to the desired surface temperature. To reach the desired surface temperature generally required less than 10 seconds.

13. Once the Peltier module produced the desired the surface temperature a stopwatch was started and the test had begun.

Photography Procedure

The following steps outline the photogrammetric data acquisition method for capturing frost roughness. The camera was mounted to the tri-axial traversing system and ensured to be parallel with the test surface using a bubble level. Next the camera was ensured to have a reproduction ratio of 1.0x, an ISO of 200, and an aperture of f/22. The instrumentation was now set up for data acquisition. Data acquisition occurred every 15 minutes in the following steps:

1. At one minute before the start of data acquisition, the fiber optic light guides were ensured to be level with the frost thickness. Additionally, the multi-axial traverse was operated to position the camera directly overhead of the test surface corner comprised of the trailing edge and scale bar.
2. At 30 seconds before the start of data acquisition, the vertical micro slide was adjusted so that the top of the frost dendrites were the most in focused aspect in the camera image.
3. After the vertical slide was adjusted and locked, a test picture was taken of the frost to check the exposure of the image. The shutter speed was adjusted if the frost and scale bar were underexposed or overexposed. All test pictures were deleted.
4. At the start of data acquisition, a cyclic operation began of capturing a photo with a remote sensor and traversing the camera. During the moments when images were captured, neither the camera nor the traversing system were physically touched to ensure no camera movement. Between the moments of capturing images, the camera

was traversed approximately 2.15 mm in the positive y-direction. Once this cyclic y-direction traverse had occurred for the acquisition of 10 images, the camera was traversed approximately 4.45 mm in the positive x-direction for one repetition. Next, the y-axis traversing/image capturing cycle was repeated in the negative y-direction. This entire traversing/image capturing procedure was repeated once more so that a total of 4 columns of 10 images were acquired. The approximate time to capture all 40 images was 45 seconds. Figure 3.9 displays the resulting layout of the images. As a side note, with the approximate 2.15mm y-axis movements and 4.45mm x-axis movements (and 1.0x reproduction ratio), the overlap in the images in the y-direction and x-direction is 81.5 percent and 86.2 percent respectively. These values are within bounds of the recommended overlap between images [50].

5. At the conclusion of the 40^{th} picture, data acquisition of the frost surface for that specific time was complete. Steps one through four were repeated for two hours, to capture the full evolution of frost roughness.
6. At the conclusion of two hours, the test was complete. If testing was complete for the day, the camera was uninstalled from the traversing system and the entire psychrometric wind tunnel was shut down.

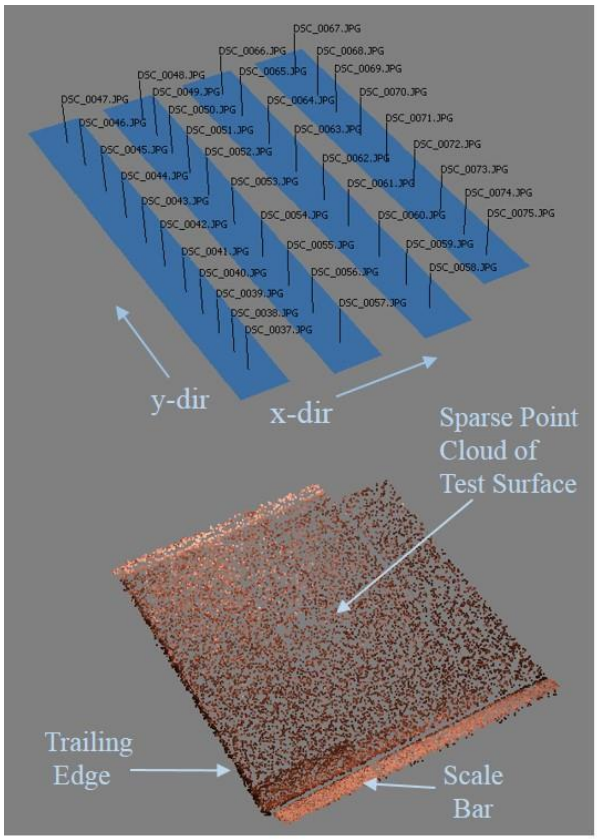

Figure 3.9: Photogrammetric Image Layout

Data Reduction

The data images collected from the tests required extensive processing. This post processing produced detailed height distributions and roughness parameter time plots. The data reduction process required two computational programs working sequentially. First, photogrammetric software (Agisoft Photoscan Pro) was used to produce a preliminary point cloud file. Next, a matrix-based programming platform (MATLAB) made corrections to the point cloud, and produced detailed and overall time evolution results. The processes used in each software is described in the sections to follow.

Photogrammetric Modeling

The commercial software used to produce a photogrammetric, point cloud model was Agisoft Photoscan Pro. Once all images were acquired for the entire duration of the two hour test, the images were subdivided by time intervals and imported into individual Agisoft Photoscan programs. The programs all followed the same software workflow as described in the following paragraphs.

First, the software would scan each image and find 120,000 corresponding points between photos. From these corresponding points, a refinement process occurred where the software would keep only the best matching 1,000 points per image. These points were considered "known" point locations on the surface and were used to orient the images. This orientation process used the coplanarity constraint as described in the technical background. Once the images were oriented, a sparse point cloud of the "known" point locations and the image locations were graphically displayed as shown in Figure 3.9. The next step was to visually ensure that the point cloud surface and images were parallel on the same x-y plane. On the rare occasion that they were not aligned, the graphic display would clearly indicate this with a catastrophic layout of the image orientations. If this was the case, each image was visually analyzed, the image causing an issue was deleted and the orientation process was recomputed. Once the point cloud surface and the images were properly aligned, a bounding box was defined to enclose only the surface area of interest. This reduced the computation time in the following step.

Next, the dense point cloud was generated from the oriented images. However each image had 24 million pixels and calculating the location of this many pixels would take over 48 hours computation time on an Intel i7-4790 processor. Therefore, the image sizes

were reduced by three quarters so that only 6 million pixels existed and the computation time was reduced to approximately 15 hours. The computation involved the following. The photogrammetric software would scan the 6 million pixels and determine corresponding pixels between images. If individual pixels did not correspond between images, they were eliminated from placement in the 3D dense point cloud. Since the majority of the pixels were identified between more than two images a filtering process occurred where 3D points were eliminated that had too much variation in their calculated locations based on pairs of images. Mathematically this occurred through a process similar to the method of least squares where if the resulting R-squared value was not close enough to a value of one, then that point was eliminated from the point cloud. At the conclusion of the computation, a dense point cloud of the frost and scale bar were displayed, as shown in Figure 3.10.

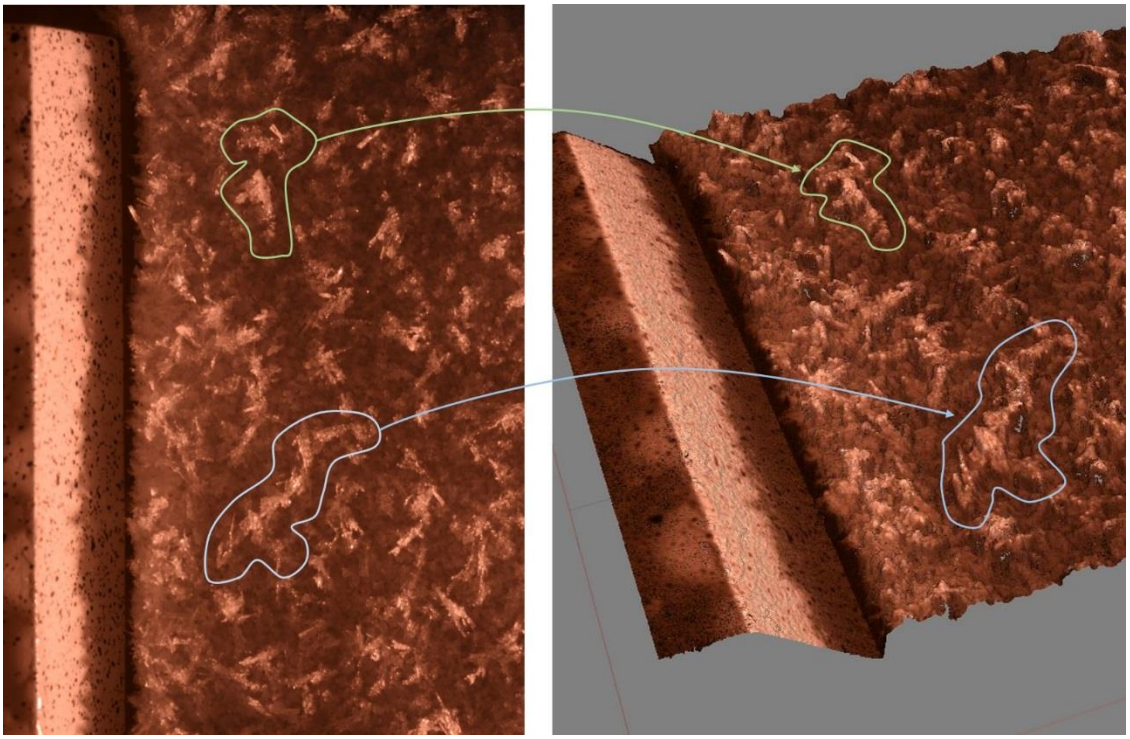

Figure 3.10: Example of Data Image (Left) and Resulting Point Cloud Photogrammetric Model (Right) with Matching Frost Dendrite Elements

Further, Figure 3.10 demonstrates the robust detailing abilities of the photogrammetric method as specific frost elements can clearly be seen.

Scaling Model

Once the dense point cloud had been generated, each photogrammetric model still needed to be scaled to the correct units in the x, y and z direction. The next sections describe the steps required for proper scaling of the model.

X and Y Direction. The scale bar was designed to easily define measurements in the photogrammetric software to constrain the model in the x and y direction to the correct size. The initial step to this process required a user to place markers on the slope of the scale bar in the photogrammetric model. It was necessary for the locations of these markers to be at equal heights because this scaled the model specifically in the x and y direction. Additionally, the markers needed to be placed on clearly defined targets. As seen in Figure 3.10, as the frost thickness grew it cast a shadow on the scale bar. Targets that were shadowed could not be easily seen, therefore clearly defined targets were the specks of black spray paint that were above the shadow which were in high contrast to the white background surface. Once targets were selected and markers were placed on the photogrammetric model, the physical scale bar was taken and scanned with a Keyence VR 3000 macroscope. The distance between the targets that had been selected in the photogrammetric model, was measured with the macroscope. This measurement was imported into the photogrammetric software thus scaling the model in the x and y direction. Figure 3.11 shows two markers labeled with blue flags (point 1 and point 2) that define the

distance between two targets. The Keyence macroscope scan that measured the distance between the targets is also displayed in the figure.

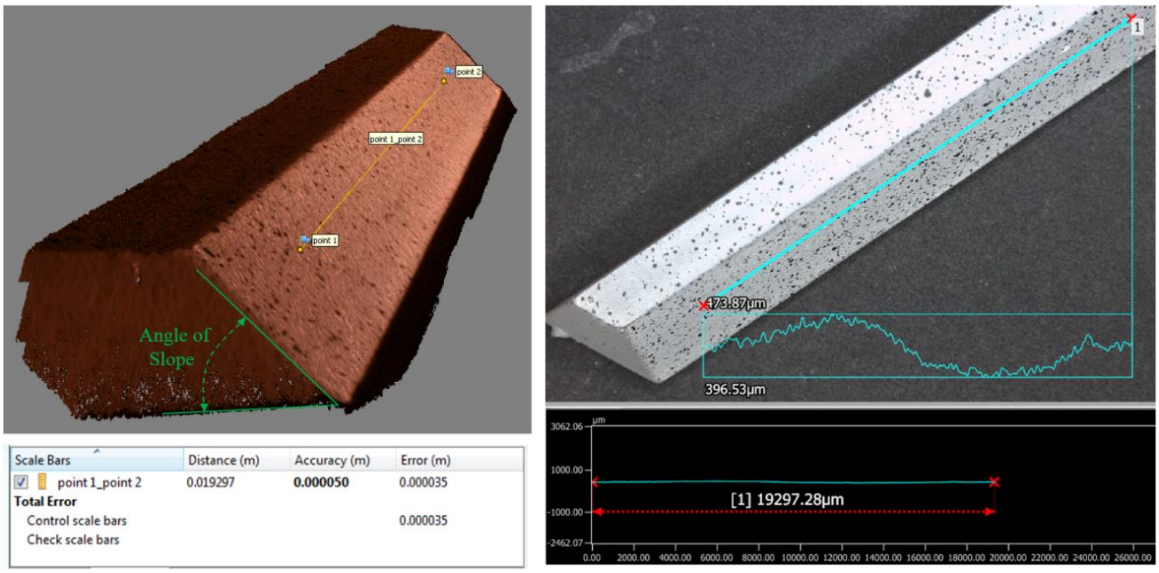

Figure 3.11: Scale Bar: Photogrammetric Model with Imported Marker Distance and Exported Slope (Left) and Macroscope Scan with Measured Target Distance (Right)

Z-Direction. In an ideal case one measurement would define the model in the x, y, and z direction. However, due to the photogrammetry software initializing the image locations, the software incorrectly placed the images farther away from the surface compared to the true physical coordinates. This resulted in the entire model being proportionally shorter in the z-direction than what it actually was. If the image locations had been tracked with the camera movement and had been imported into the photogrammetric software, the z-direction would have correctly scaled with the x/y measurement. Instead to resolve this problem, a MATLAB program corrected the point cloud file of the photogrammetric model by only scaling the model in the z-direction. The magnitude that the model was scaled in the z-direction was determined by comparing the physical slope of the scale bar to the computed slope of the scale bar in the photogrammetric model. The following paragraphs detail the programming method for

determining the difference in slopes and the resulting magnitude required to correctly scale the dense point cloud model in the z-direction. This z-direction magnitude scale is referred to as the z-scaling factor.

Two point cloud files of the scale bar were used for determining the z-scaling factor. The first point cloud file was the top surface of the scale bar and the second file was the sloped surface as labeled in Figure 3.11. The z-scaling factor hinged upon the assumption that the physical sloped surface was 60 degrees from horizontal based off of the SolidWorks model. Upon further analysis using the Keyence VR 3000, this assumption proved to be slightly off. Figure 3.12 outlines a side profile view of the scale bar measured with the Keyence macroscope. The difference in angle between the horizontal surface and the top scale bar plane demonstrates that the slope of the surface is not always 60 degrees.

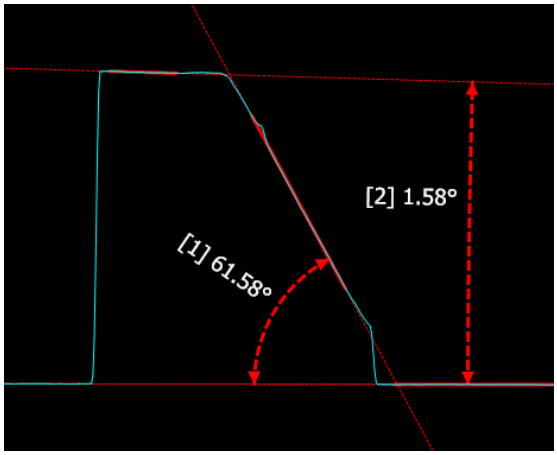

Figure 3.12: Difference in Angle Between Top Surface and Horizontal Plane

Further, this difference in angle could change slightly with the movement of the scale bar, therefore a simple subtraction of 1.58 degrees could not be applied every time. To resolve the issue, the point cloud file of the top surface of the scale bar was compared to the difference in angle with the horizontal plane. This difference in angles was then

inserted into a rotational matrix that rotated the entire point cloud file of the scale bar. The scale bar point cloud file was now corrected for any difference in angle from horizontal and the 60 degree known measurement could be used.

With the 60 degree sloped surface point cloud file, the z-scaling factor could easily be obtained using an iterative method. The computation minutely increased the slope of the point cloud file with a multiplying factor until it matched the 60 degree slope of the physical scale bar. The final multiplying factor that resulted in matching slopes was the z-scaling factor. This, z-scaling factor was applied to the point cloud file of the frost surface, resulting in a model that was correctly scaled in the x, y and z direction. An example of a completed model is displayed in Figure 3.13. For the MATLAB functions that ran these computations, refer to Appendix A.

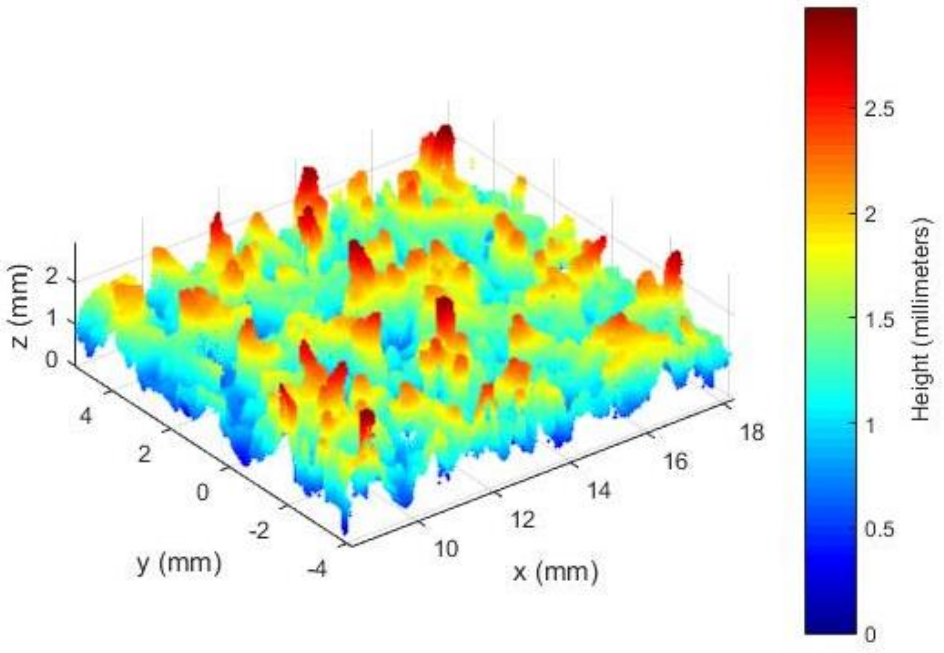

Figure 3.13: Example of Final Dense 3D Point Cloud Model

Surface Parameters

From the correctly scaled dense point cloud model, surface roughness analysis could easily be performed. The point cloud file as exampled in Figure 3.13 was exported as a three column matrix, containing x, y and z locations of each point. Since, the frost was developed on a flat plate and not on a curved surface of an aircraft wing, a simple planar fit was applied to the data. This plane represented the mean surface height of the frost. From this plane the root-mean-square height, skewness, and peak-to-valley height were computationally found. Furthermore, the RMS height and skewness were used to easily calculate the equivalent sand-grain roughness height of Eq. (2.8).

The root-mean-square height was calculated using a numerical method by summing the squared difference of each point's z-location and the planar fit. This summation was divided by the total number of points. The resulting quotient was square rooted and the calculated answer represented the RMS height for that frost surface data.

The skewness was calculated in a similar method as the root-mean-square height with two alterations to the equation. First the summation of the difference was cubed. Additionally, the square root of the quotient was not taken, but instead the quotient was divided by the RMS height cubed. The resulting answer represented the asperity or degree of bias of frost roughness elements.

The overall maximum height parameter or peak-to-valley was simply calculated by equipping the max and min function in MATLAB to find the highest and lowest z-location points normal to the planar fit. This maximum height was summed with the absolute value of the minimum height to obtain the overall maximum height parameter. For additional details on the numerical computations of the surface parameters refer to Appendix A.

The roughness parameter results were used for analysis of variance (ANOVA), sensitivity analysis, validation tests, and can be used for future studies. Analysis of variance is a statistical testing method developed by Fisher [61] and is useful for comparing multiple variables at once to see if results change based on certain variables or combinations of variables. For this study a two-way ANOVA test was assessed because it indicates the significance of environmental factors and combinational effects of paired environmental conditions on frost roughness formation. Conceptually, this is similar to performing multiple two-sample, t-tests to check for significance of variables. The statistical software JMP performed the ANOVA computations for this research to determine the statistical significance of the test variables: air temperature, air velocity, surface temperatures and relative humidity. Sensitivity analysis is simpler than ANOVA, but still a powerful analysis tool. It determines the effect a single variable has on an output result by holding all other variables constant [62]. The results of these two analysis methods are presented in the Chapter Four. Validation is presented in the following section.

Validation

Validation was essential to ensure that the photogrammetric frost measuring technique was precise and accurate. There were three validations processes used for this study: measurement method comparison, repeatability and measurement frequency test.

Measurement Method Comparison

Artificially Roughened Surfaces. With the newly established photogrammetric method, a measurement comparison was the first necessary validation. Since no research has accurately measured frost roughness before, there was no established values for

comparing the results of the photogrammetric method. Instead, plastic surfaces with artificial roughness values similar to estimated frost roughness parameters were fabricated for comparing the photogrammetric method to an established roughness measuring method. These validation surfaces were modeled using a Lagranian droplet simulator that randomly plotted circles with diameters ranging within a Gaussian distribution [63]. From the circles, cones were 3D modeled and converted to a stereolithography (STL) file producing a 3D printable model with specific roughness parameters. A total of seven validation surfaces were created, with the following approximate peak-to-valley heights: 250, 500, 750, 1000, 1500, 2000 and 3000 µm. Figure 3.14 presents height distribution renderings for four of these surfaces. The STL models were printed on the Form 2 printer with the resolution set to 25 µm. An example of one of the resulting 3D printed surfaces is pictured in Figure 3.15.

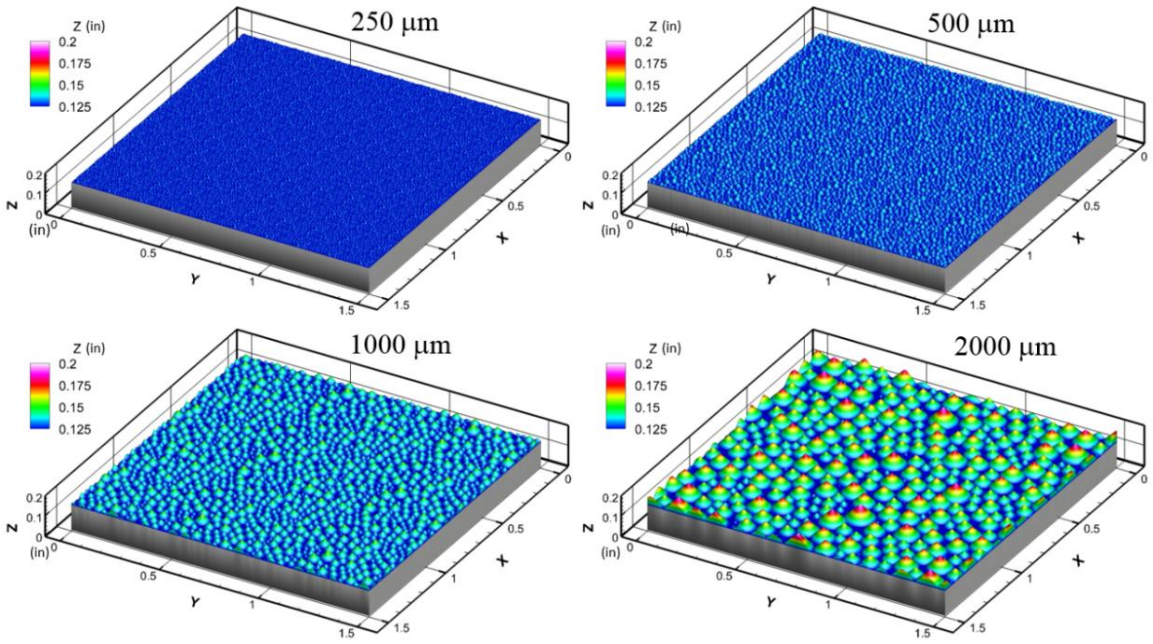

Figure 3.14: Validation Surfaces with Various Maximum Peak-to-Valley Heights

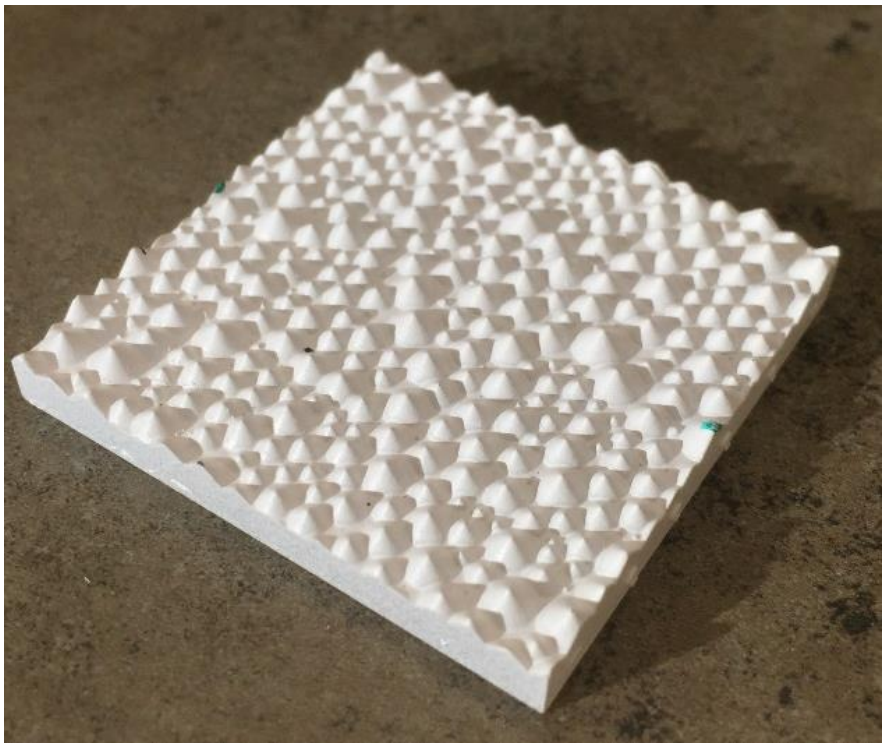

Figure 3.15: 3D Printed Surface (2000μm Peak-to-Valley Height)

The plastic surfaces were scanned with the Keyence VR 3000 light-induced profilometer to acquire the detailed height distributions and true surface roughness parameters. Appendix C presents the Keyence measurements of peak-to-valley height, skewness, and RMS values for all seven surfaces. On a side note, the Keyence profilometer uses diffraction patterns thereby disabling it from being used to measure real frost roughness. As seen in Figure 3.15, the printed models were coated with a matte white spray paint in order to correctly measure surface roughness with the Keyence VR 3000. The photogrammetric method did not require this as the photogrammetry software was able to obtain measurements regardless of whether the plastic surface models were clear or matte white.

Artificial Surface Photogrammetry With the plastic surfaces fabricated and the true roughness parameters known from the profilometer, the surfaces were measured using the photogrammetric method previously described. It is important to note that the scale bar was utilized in the exact same way as described with the frost measurements even though targets could have been placed on the artificial surfaces. Moreover, data acquisition occurred with the artificial surfaces in the wind tunnel without the tunnel operating. Camera settings, traversing movement and lighting all remained constant with the same settings used in the real frost testing to ensure a consistent and valid photographic method. The photogrammetric modeling and scaling were conducted as described previously, leading to the final results of detailed height distributions and roughness parameters. The photogrammetric method was repeated three times on the validation surfaces to ensure no other response factors were involved. Finally, the results were compared to the measurements taken with the Keyence profilometer.

Detailed Height Distribution Comparison In the assessment of the comparison validation for the photogrammetric method, the detailed height distributions of the plastic surfaces were evaluated against the topographic scans of the Keyence profilometer. All seven surfaces had similar results. Figure 3.16 presents two of these visual comparisons, specifically for the 0.021 and 0.31 mm RMS surfaces. The plots in the figure are magnified to show the details of the individual cone roughness elements. The following conclusions were made about the photogrammetric method from the detailed height distributions. Overall, the photogrammetric surface models appeared very similar to the true surface topography measured by the Keyence. The photogrammetric models portray the correct spacing of roughness elements, the correct maximum to minimum height difference and

the correct slope on the cone surfaces. Even for the least rough surface (Figure 3.16a) the photogrammetric method measured the correct locations of peaks and valleys at relatively correct heights. This demonstrates the resolution ability of the micro photogrammetric method and its capacity to measure miniscule frost dendrites.

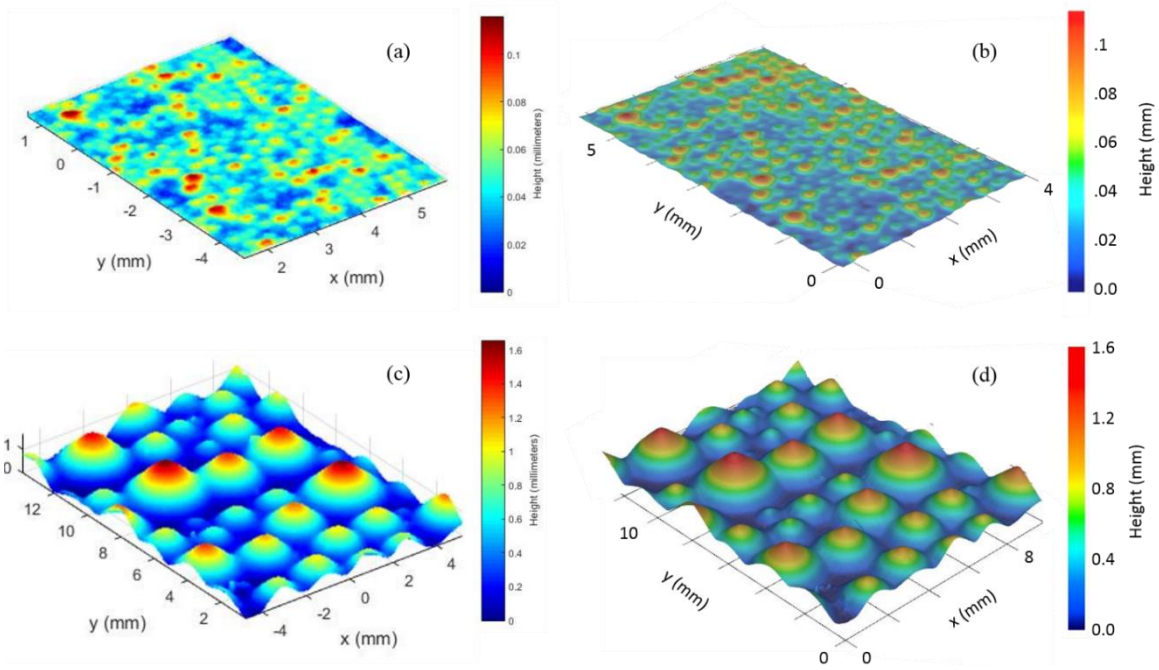

Figure 3.16: Surface Height Distribution Comparison of Photogrammetric Method (a,c) and Keyence Profilometer (b,d): for 0.021 mm (b,d) and 0.31 mm (c,d) RMS Height

Roughness Statistic Percent Difference. The percent differences between the photogrammetrically measured roughness statistics and the profilometric measured values are presented in Figure 3.17. The most important aspect to note from the figure below is that the percent difference is less than 7% for RMS heights greater than 0.1 mm. This indicates that the defined photogrammetric method is accurate for the frost roughness measurements of greatest concern. On the other hand, the two least rough surfaces (0.21 mm and 0.54 mm RMS height) reveal an increase in percent difference, demonstrating the maximum resolution of the photography system leading to inaccuracy in the

measurements. However, the inaccuracy for RMS heights less than 0.1 mm is of little concern because a surface roughness of this magnitude is negligible on an aircraft's wing. In view of the repeatability results, it is evident that the vast majority of frost RMS heights were above 0.1 mm, indicating that the photogrammetric method is a valid and accurate technique for measuring frost roughness. Appendix C was used to draw the same conclusions for the skewness, peak-to-valley height and equivalent sand-grain roughness.

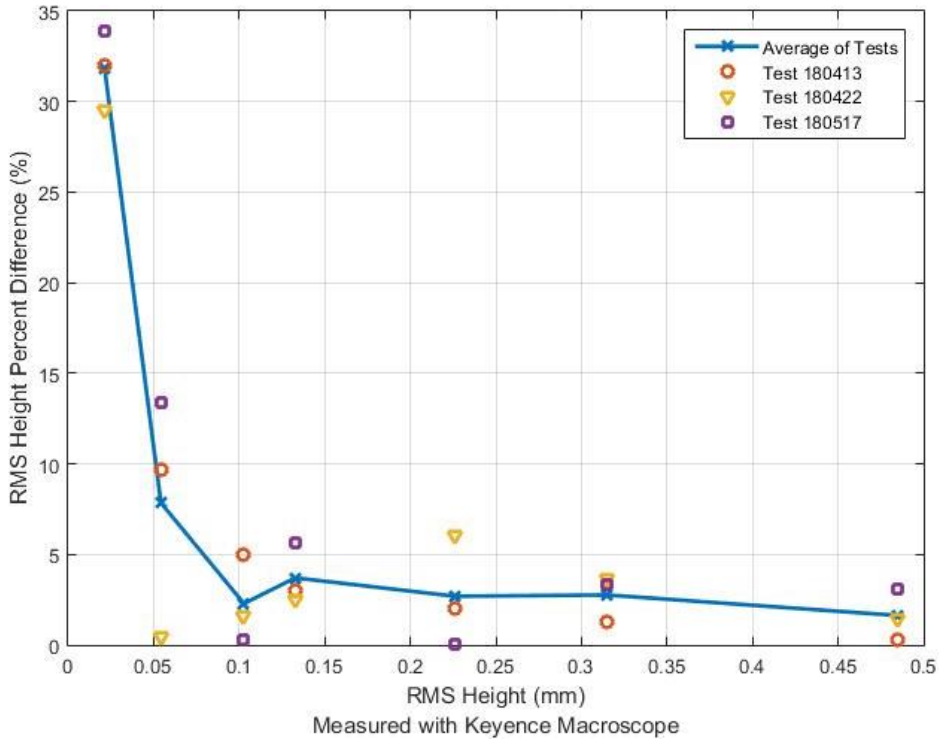

Figure 3.17: Percent Difference of Photogrammetric Method with Increasing Roughness

Repeatability

With an established photogrammetric method that provided accurate surface roughness measurements, the second validation procedure focused on repeatability. Repeatability ensured that the psychrometric wind tunnel produced similar frost formations at the same operating conditions. Moreover, it ensured that the photogrammetric method

and data reduction produced consistent measurements. Figure 3.18 through Figure 3.20 display the photogrammetric measurements of surface roughness evolution for three repeated tests with the same wind tunnel operating conditions

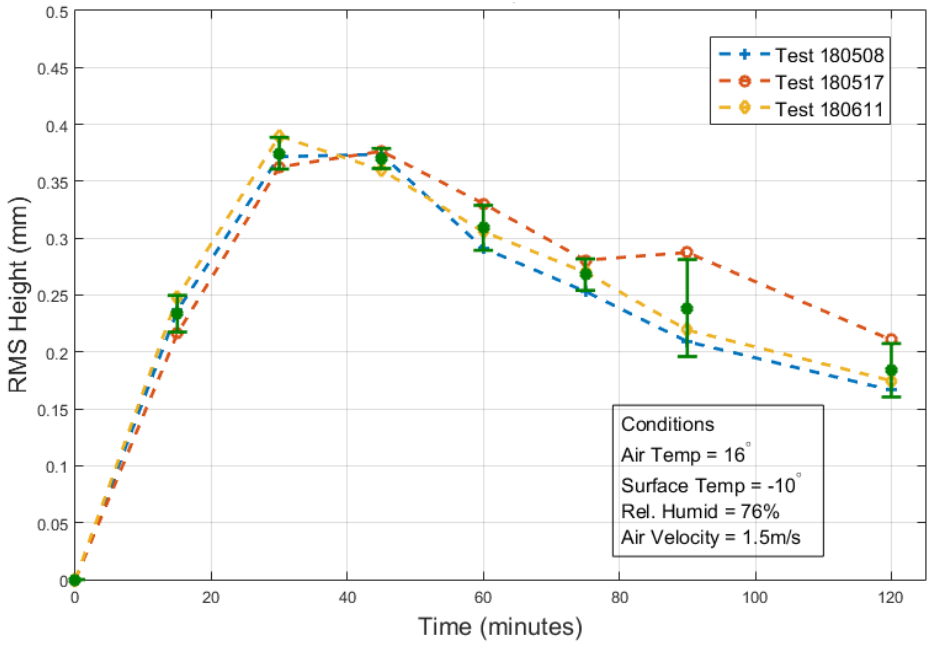

Figure 3.18: Repeatability of Measuring RMS Height Using Photogrammetry

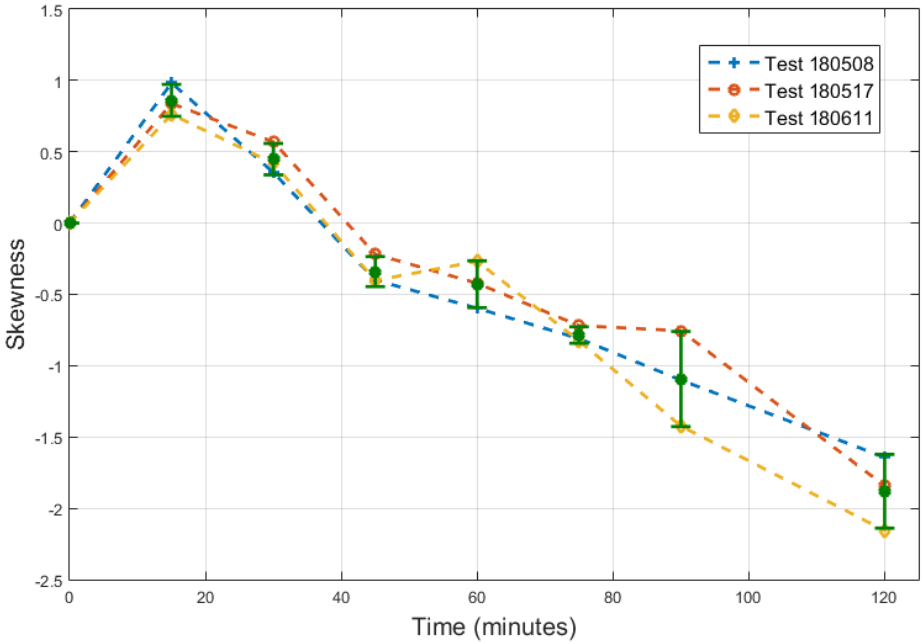

Figure 3.19: Repeatability of Measuring Skewness Using Photogrammetry

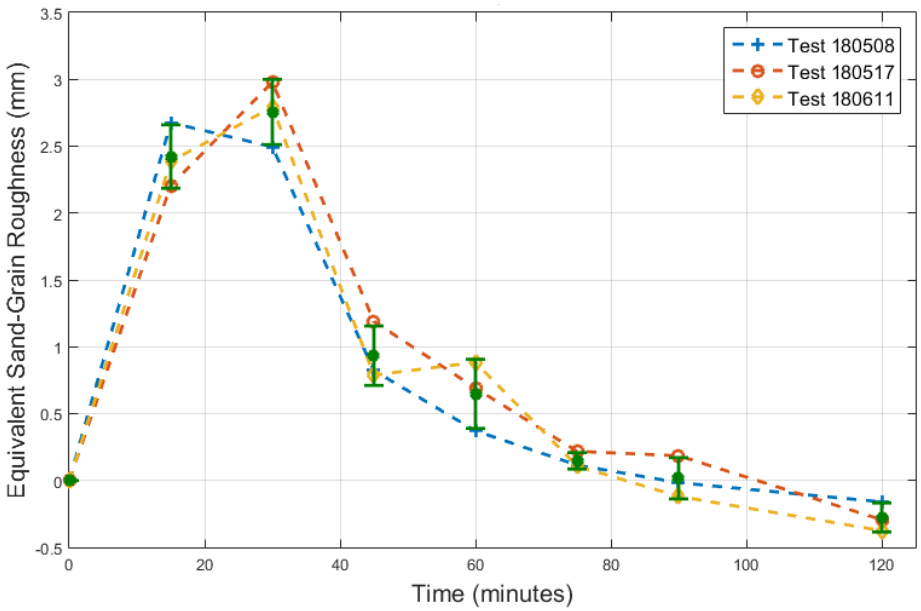

Figure 3.20: Repeatability of Measuring Equivalent Sand-Grain Using Photogrammetry

The repeatability results reveal that the photogrammetric method used for evaluating frost roughness in the Baylor Frost Tunnel is consistent and reliable as measurements for each time increment portray minimal standard deviations. The deviations increased after the first 45 minutes which was when the RMS height started to decrease and the skewness became significantly negative. The maximum standard deviation for the RMS height was 0.043 mm which occurred at 90 minutes and for the skewness it was 0.334. These inconsistencies are believed to have resulted from the stochastic nature of frost formation, specifically due to the unpredictable cycle of redensification and regrowth. Furthermore, the equivalent sand-grain roughness had a more severe, maximum standard deviation of 0.259 mm because it depended on the combined effects of the RMS height and skewness. Regardless of these minor discrepancies, the three repeated tests followed the same general trend line demonstrating that the photogrammetric method coupled with the Baylor Frost Tunnel is repeatable.

Measurement Frequency Check

The final check to ensure that the photogrammetric method was valid entailed increasing the measurement frequency from 15 minutes per data acquisition set to 5 minutes. For this examination, one of the frost formation conditions that was expected to produce more severe roughness was selected. The main objective from this validation was to ensure that no valuable evolution data was lost during the 15 minute intervals. From Figure 3.21 and Figure 3.22 it becomes evident that for the majority of the time frame a measurement frequency of 15 minutes sufficed for comprehensively acquiring evolution data.

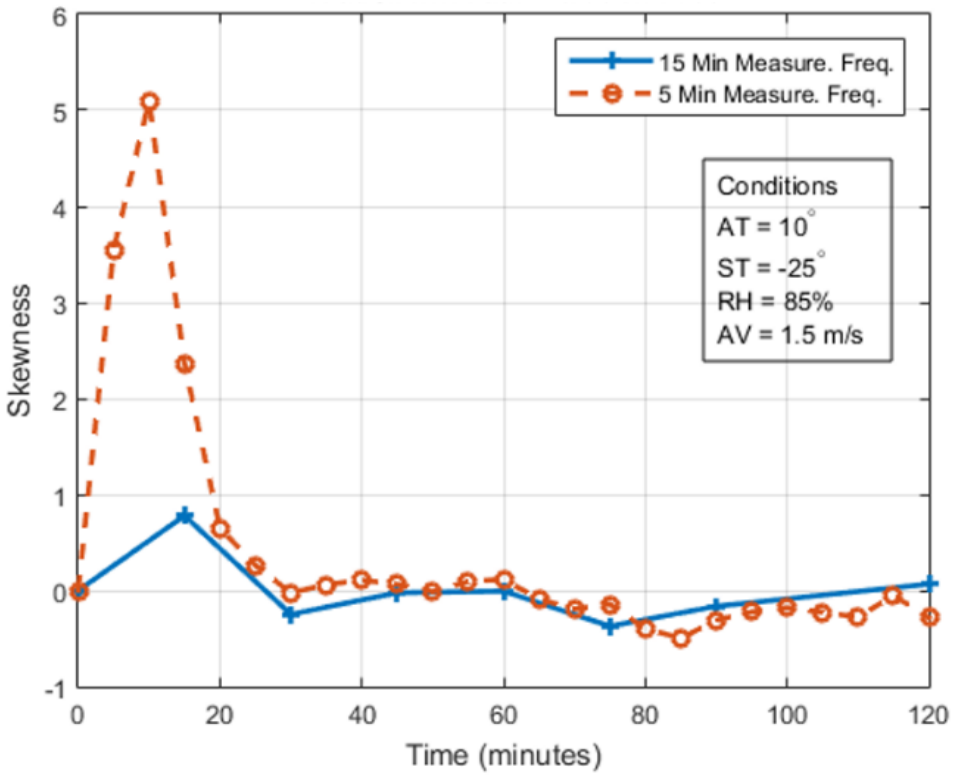

Figure 3.21: Measurement Frequency Check – Frost Skewness Evolution Plot

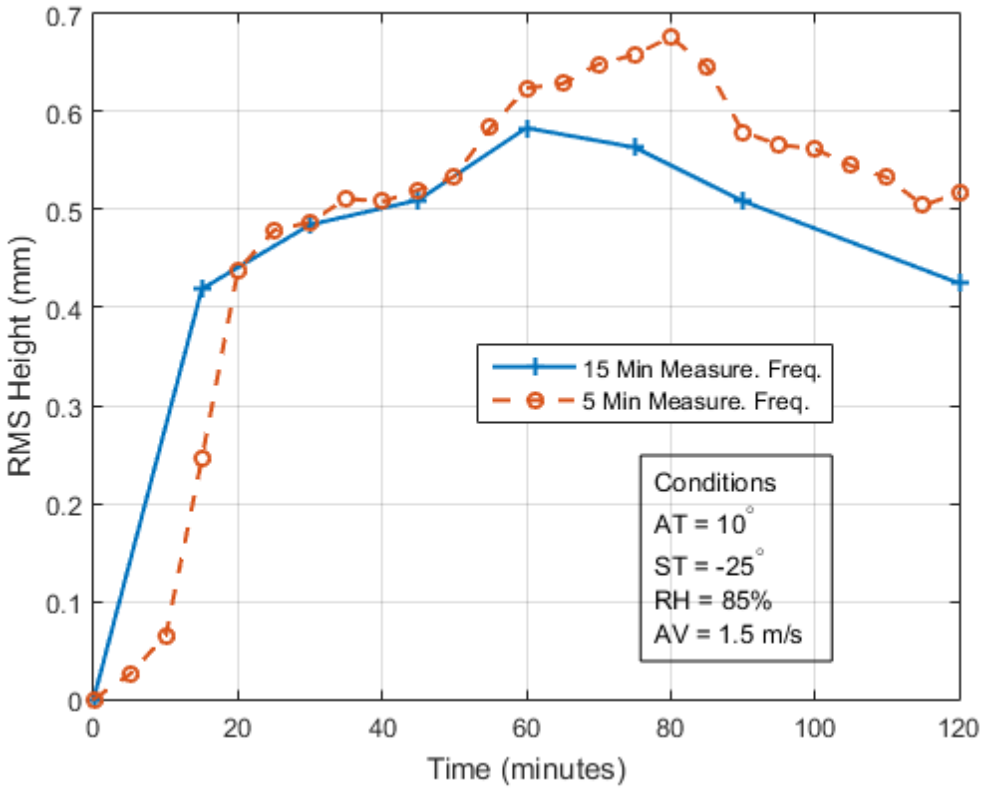

Figure 3.22: Measurement Frequency Check – Frost RMS Height Evolution Plot

However before the first measurement, there was an initial spike in the skewness that was not entirely captured with the 15 minute measurement frequency. This discrepancy was from the foremost frost dendrites rapidly developing before a frost base layer forms. This phenomenon only occurred for extremely cold surface temperatures that are unlikely to be sustained in the event of cold-soaked fuel frost. Furthermore this lost data is of little concern because aircraft very rarely have a turnaround time less than 15 minute as the average turnaround time ranges from 20 minutes to an hour [64].

Validation Summary

In review of the validation process, the photogrammetric method was developed to be accurate and precise. A measurement comparison between the photogrammetric method

and an established profilometery device was conducted through the fabrication of artificially roughened surfaces. The results present very accurate measurements as the percent differences are less than 7% for roughness heights of concern. Additionally, the coupling of the photogrammetric instrumentation and wind tunnel demonstrated repeatable frost formation measurements as similar roughness values were recorded on three different occasions. A measurement frequency check ensured that no valuable data for interpreting the frost evolution plots was lost between data acquisition times. Because of the accurate, precise and repeatable results demonstrated by the validation checks, the photogrammetric method is considered to be established and may be used to measure transient surface roughness in application to frost contamination on cold-soaked aircraft wings.

Test Cases Employed

To develop an understanding of the characteristics of frost evolution and the importance of the chosen environmental variables governing the frost evolution, two tests with completely different environmental conditions were chosen as base operating conditions. The two base conditions employed in the psychrometric tunnel are described as Test: Base 1 and Base 2 in Table 3.2. By varying the environmental conditions relative to the two base conditions, fourteen more cases were investigated and used to perform an ANOVA experiment to determine the most important parameters governing frost roughness evolution. All sixteen cases are described in Table 3.2. For each of the test conditions, the frost roughness topography was measured using the structure-from-motion photogrammetric method. The relevant surface statistics such as RMS roughness height, peak-to-valley height, skewness, and equivalent sand-grain roughness were evaluated using Eqns. (2.6)-(2.8). The ANOVA statistical assessment was then performed on the

resulting roughness description parameters. Additionally from these tests, specific results were grouped together for analysis. These grouped tests gave more clarity to the interaction, sensitivity and predictability of the four environmental factors. Additional tests were conducted for the air temperature and air velocity to gain a further understanding of these two high-influencing factors.

Table 3.2: ANOVA Test Conditions

Test	**Date (*yymmdd*)**	**Frost Evolution Test Conditions**			
		Air Temperature	**Surface Temperature**	**Relative Humidity**	**Air Velocity**
Base 1	180425	16 °C	-10 °C	76 %	0.5 m/s
Base 2	180523	10 °C	-25 °C	85 %	1.5 m/s
3	180508	16 °C	-10 °C	76 %	1.5 m/s
4	180508	16 °C	-25 °C	76 %	1.5 m/s
5	180517	10 °C	-10 °C	76 %	1.5 m/s
6	180517	10 °C	-10 °C	85 %	0.5 m/s
7	180519	10 °C	-10 °C	76 %	0.5 m/s
8	180523	10 °C	-10 °C	85 %	1.5 m/s
9	180528	16 °C	-10 °C	85 %	1.5 m/s
10	180529	16 °C	-25 °C	85 %	0.5 m/s
11	180529	16 °C	-25 °C	85 %	1.5 m/s
12	180604	10 °C	-25 °C	76 %	0.5 m/s
13	180604	10 °C	-25 °C	85 %	0.5 m/s
14	180606	16 °C	-10 °C	85 %	0.5 m/s
15	180606	16 °C	-25 °C	76 %	0.5 m/s
16	180611	10 °C	-25 °C	76 %	1.5 m/s

CHAPTER FOUR

Results and Discussion

This chapter presents the results of frost surface formations procured at various atmospheric conditions in the closed-loop, psychrometric wind tunnel and measured with the newly established photogrammetric method. There are two forms of results presented: detailed roughness topography measurements and reduced roughness parameter evolution plots. The detailed height distributions portray the characteristics of each frost condition and enable visualization of the frost surfaces.

The reduced roughness parameters: root-mean-square height, skewness, peak-to-valley height reveal the effects of the atmospheric conditions. The equivalent sand-grain roughness is presented because it is the most significant factor in determining the aerodynamic effects that frost accumulation has on aircraft wings. Although, the complete aerodynamic impacts are not presented in this research, it is beneficial to keep in mind that larger values of equivalent sand-grain roughness cause a greater aerodynamic degradation. Furthermore, the detailed height distributions qualitatively confirm the roughness parameters.

The first section presents a comprehensive evolution of detailed frost distributions and the corresponding roughness time plots to give a general understanding of the characteristics of frost at various stages in development. The next section presents the roughness parameter results formulated in a two-way Analysis of Variance (ANOVA) test which indicates the more significant atmospheric conditions and interaction effects that dictate frost roughness. This section also discusses the result's application to cold-soaked

fuel frost aircraft takeoffs. The third section presents a closer examination of the more significant environmental conditions through an in-depth analysis of sensitivity and interaction. The condition with the least significance is also confirmed through a simple sensitivity plot. The results conclude with a hypothesis on the general atmospheric conditions that may cause one of the more severe cases of frictional drag from frost contamination.

Frost Evolution Characteristics

For a fundamental understanding of the characteristics of frost evolution, two tests with completely different environmental conditions (as shown in Table 3.2) were performed within the psychrometric tunnel. The frost roughness was evaluated from the results shown in Figure 4.1 through Figure 4.3. The detailed height distributions of Figure 4.1 and Figure 4.2 portray frost dendrites developing from relatively smooth surfaces into rough surfaces consisting of frost dendrites of different shapes, depending on the test conditions. However, both tests resulted in frost roughness that had maximum equivalent sand-grain roughness heights and RMS heights at around the 60 minute measurement (confirmed in Figure 4.3). Before this time, the frost roughness (RMS and peak-to-valley height) increased at a relatively rapid pace. However after 60 minutes, the frost demonstrated a slow decrease in RMS and peak-to-valley roughness values while still increasing in thickness. Furthermore, the frost portrayed an initial increase, then decrease in skewness. Figure 4.1 and Figure 4.2 display these roughness observations and may be used to explain how the frost dendrites reached a maximum allowable height in the boundary layer before collapsing or melting back into the frost sublayer. The frost sublayer also increased in density from the continued growth of frost dendrites within the crystalline

matrix. The increased density reduced the severity of the frost dendrite peaks which resulted in a decreased frictional drag. However this will also incur an increase in the form drag because the increased frost thickness would slightly widened the shape of a wing. A final comment in application to cold-soaked fuel frost is that the drastic difference between the initial frost surface and the developed frost roughness values, indicate that a very quick turnaround time may be aerodynamically beneficial to the takeoff of a CSFF aircraft. In comparison of the two base test conditions, it may be observed that Test 2 was much thicker and had a much larger RMS and peak-to-valley height, but this did not necessarily equate to having a greater equivalent sand-grain roughness because of the influence of the skewness as shown in Figure 4.3. Therefore, it was important to assess the skewness, peak-to-valley and RMS height evolution plots to more fully understand the resulting sand-grain roughness. Although these results give a fundamental understanding of frost formation, they did not indicate which atmospheric conditions have the greatest effect on frost roughness formation, therefore additionally testing was necessary.

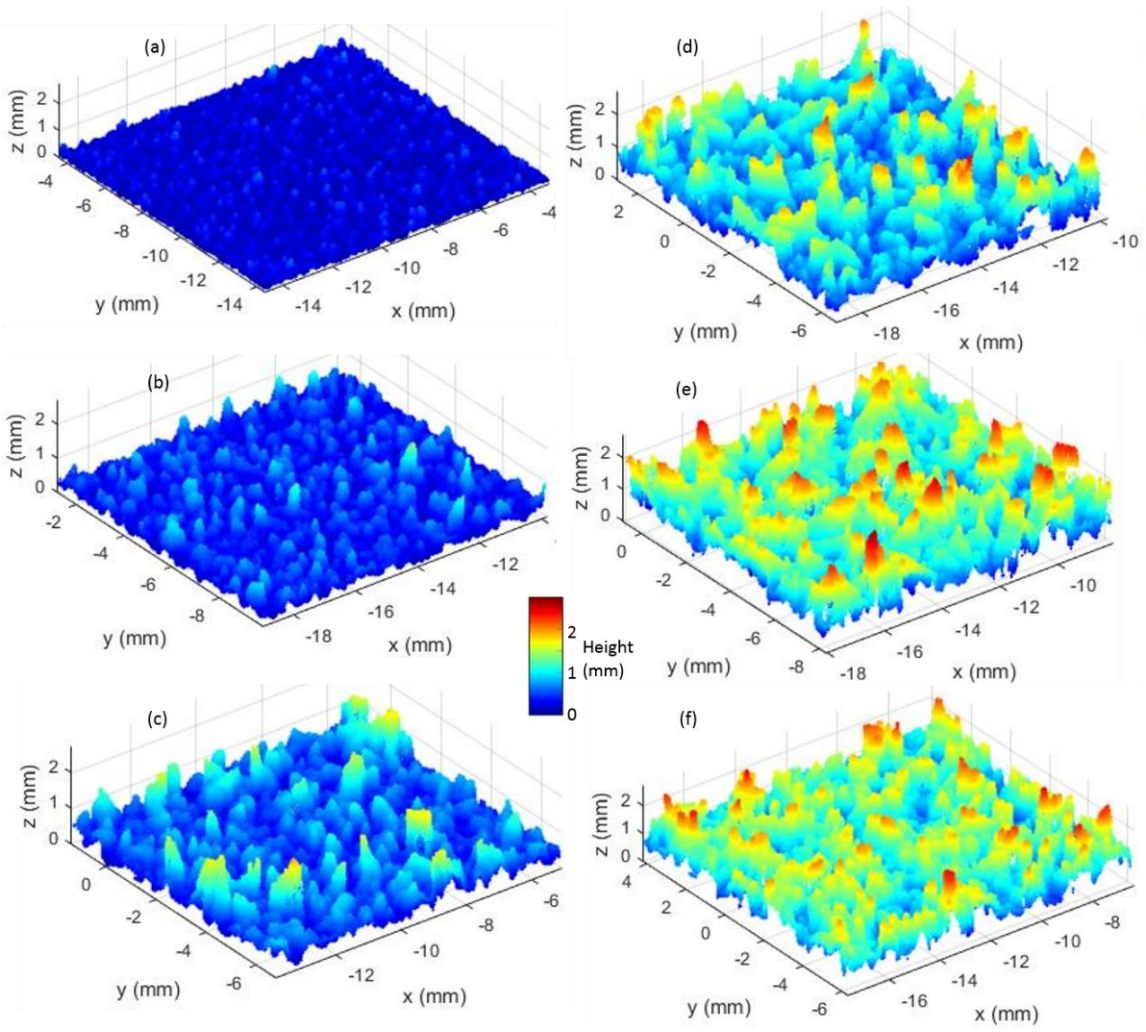

Figure 4.1: Detailed Height Distribution of Frost Evolution of Base Test 1 (16 °C -10 °C 76% 0.5m/s) at: (a) 15 minutes, (b) 30 minutes, (c) 45 minutes, (d) 60 minutes, (e) 75 minutes, (f) 90 minutes

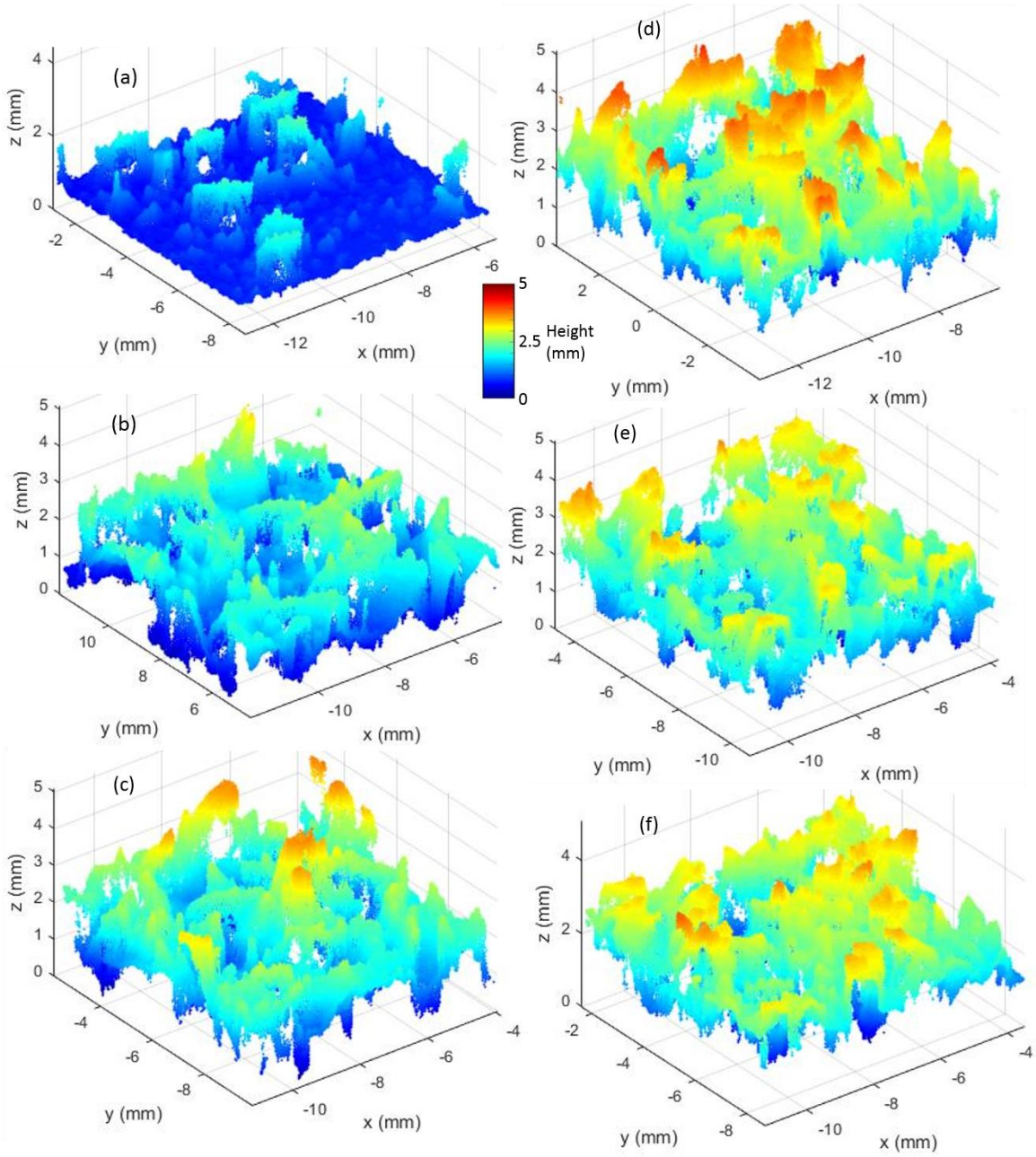

Figure 4.2: Detailed Height Distribution of Frost Evolution of Base Test 2 (10 °C -25 °C 85% 1.5m/s) at: (a) 15 minutes, (b) 30 minutes, (c) 45 minutes, (d) 60 minutes, (e) 75 minutes, (f) 90 minutes

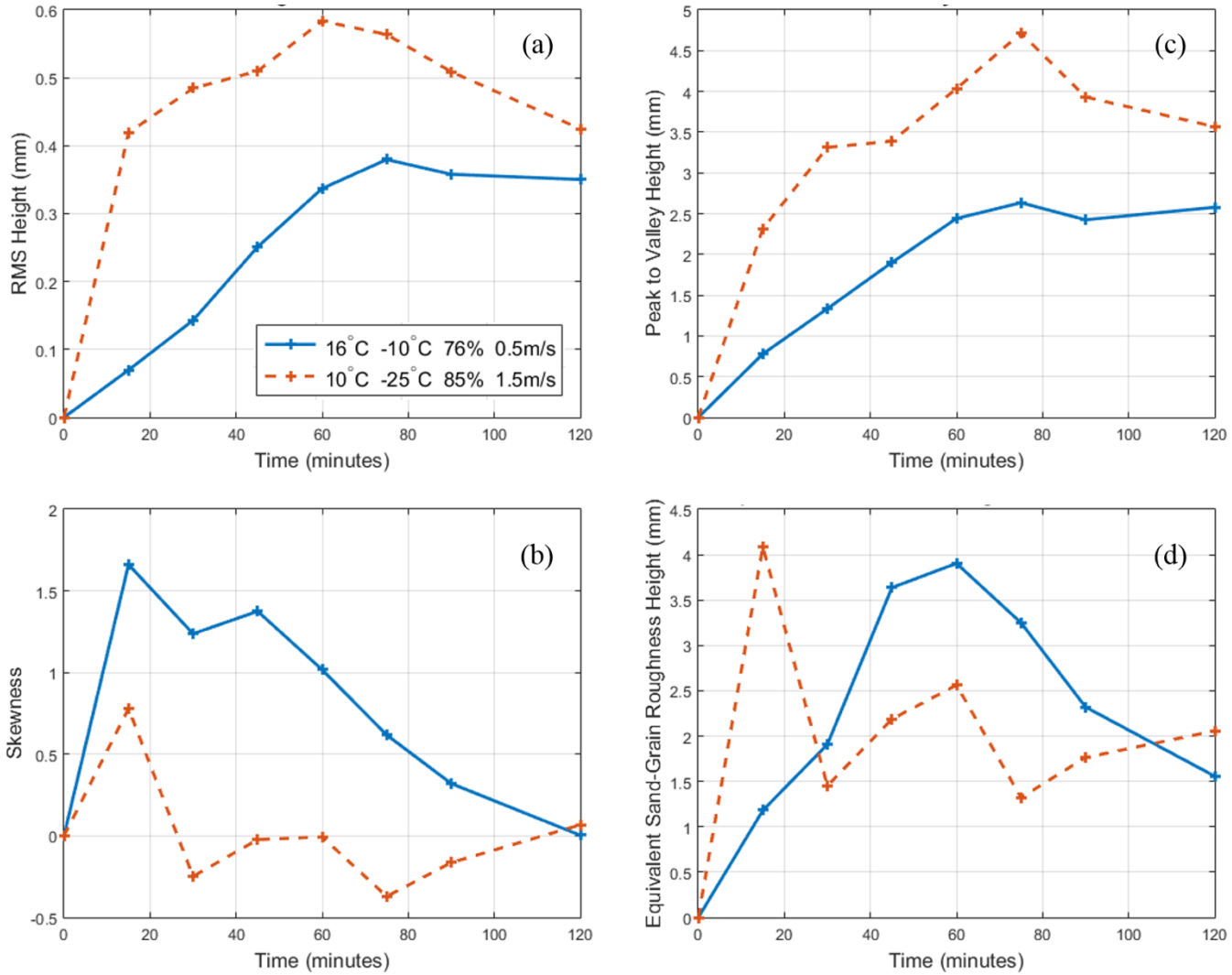

Figure 4.3: Roughness Parameter Evolution Plots : (a) RMS Height Evolution, (b) Skewness Evolution, (c) Peak-to-Valley Height Evolution, and (d) Equivalent Sand-Grain Roughness Height Evolution

Analysis of Variance

To determine the atmospheric factors that have the most influence on the frost roughness evolution and interaction effects between factors, two analysis of variance statistical assessments were employed. The results from the test conditions of Table 3.2 were used in the ANOVA assessments and are presented in the following section.

Complete Frost Development Results

Table 4.1 through Table 4.6 present the roughness parameter measurements for the 16 test combinations of the ANOVA experiment. Following each table is a corresponding figure that displays the measurements in a plot highlighting the variations in the air temperature and the air velocity. These figures (Figure 4.4 through Figure 4.7) may be comprehended by the following clarifications. To understand the legend, a "16 -10 76 0.5" label defines a 16 °C air temperature, -10 °C surface temperature, 76% relative humidity and a 0.5 m/s air velocity. The dashed lines in the figures indicate conditions that had an air velocity of 0.5 m/s while the solid lines indicate a 1.5 m/s air velocity. The warmer colored (orange/red/yellow) lines represent the 16 °C air temperature test conditions, while the cooler colored (blue/green) lines portray the 10 °C air temperatures.

The 2 hour time evolutions of frost RMS height and peak-to-valley height in Figure 4.4 and Figure 4.6 portray several substantial conclusions about the environmental factors affecting frost roughness development. The air velocity demonstrated a significant influence on frost formation as seen with the evident trend of a faster velocity increasing the frost growth rate. This was attributed to a more rapid process of water vapor molecules, creating frost dendrites. Another prominent factor was the air temperature. The results show that a colder air temperature increased the maximum height of the frost roughness.

This maximum height may be explained by the frost dendrites reaching 0 °C in the thermal boundary layer or a critical air velocity in the viscous boundary layer at which point the dendrites either melted or collapsed back into the frost layer. Because the thermal and viscous boundary layers are related, an interaction affect occurred between the air velocity and the air temperature. This infers that the air velocity affected more than just the development rate of the frost; it also affected the allowable height of the frost dendrites.

The skewness measurements in Figure 4.5 correspond with the atmospheric influences portrayed by the other roughness measurements. Most prominent in the skewness results was a warmer air temperature resulting in a negative skewness. A negative skewness indicated a surface with frost crystals that are mainly formulated on the upper part of the frost layer. This occurred from the peak frost dendrites melting and forming a thick upper surface layer with ravines into the sublayer. Between the RMS height, peak-to-valley and skewness, the results in all three figures indicate the humidity level having the least amount of influence on the frost roughness formation. Throughout all the test results, there is no clear indication of relative humidity increasing or decreasing the frost roughness.

Table 4.1: Frost Surface Roughness Parameter Results: RMS Height (mm)

Test	**Date** (*yymmdd*)	**Conditions** *(AT_ST_RH_AV)*	**Time**						
			15 min	**30 min**	**45 min**	**60 min**	**75 min**	**90 min**	**120 min**
Base 1	180425	16_-10_76_0.5	0.0697	0.1429	0.2513	0.3370	0.3796	0.3579	0.3503
Base 2	180523	10_-25_85_1.5	0.4191	0.4846	0.5099	0.5836	0.5637	0.5089	0.4249
3	180508	16_-10_76_1.5	0.2365	0.3716	0.3737	0.2913	0.2532	0.2091	0.1664
4	180508	16_-25_76_1.5	0.4192	0.3988	0.3314	0.2265	0.2252	0.2043	0.1544
5	180517	10_-10_76_1.5	0.0710	0.1485	0.2672	0.3641	0.4037	0.4627	0.4908
6	180517	10_-10_85_0.5	0.1378	0.2298	0.2961	0.3539	0.3885	0.3803	0.4159
7	180519	10_-10_76_0.5	0.0461	0.1431	0.2695	0.2907	0.3134	0.3153	0.3658
8	180523	10_-10_85_1.5	0.0976	0.2050	0.2788	0.3131	0.3197	0.3606	0.3825
9	180528	16_-10_85_1.5	0.1972	0.4179	0.3778	0.3226	0.2510	0.2060	0.1265
10	180529	16_-25_85_0.5	0.0398	0.2149	0.2902	0.3859	0.4235	0.3894	0.3284
11	180529	16_-25_85_1.5	0.4414	0.3608	0.3168	0.2651	0.2500	0.2022	0.1555
12	180604	10_-25_76_0.5	0.0254	0.0808	0.1544	0.2856	0.4072	0.4442	0.5681
13	180604	10_-25_85_0.5	0.0305	0.0748	0.1114	0.1537	0.2504	0.3445	0.4866
14	180606	16_-10_85_0.5	0.0647	0.1385	0.2319	0.3114	0.3557	0.3687	0.3212
15	180606	16_-25_76_0.5	0.0318	0.0817	0.1951	0.2968	0.3779	0.4642	0.3988
16	180611	10_-25_76_1.5	0.4781	0.5129	0.4835	0.4888	0.4147	0.4096	0.3403

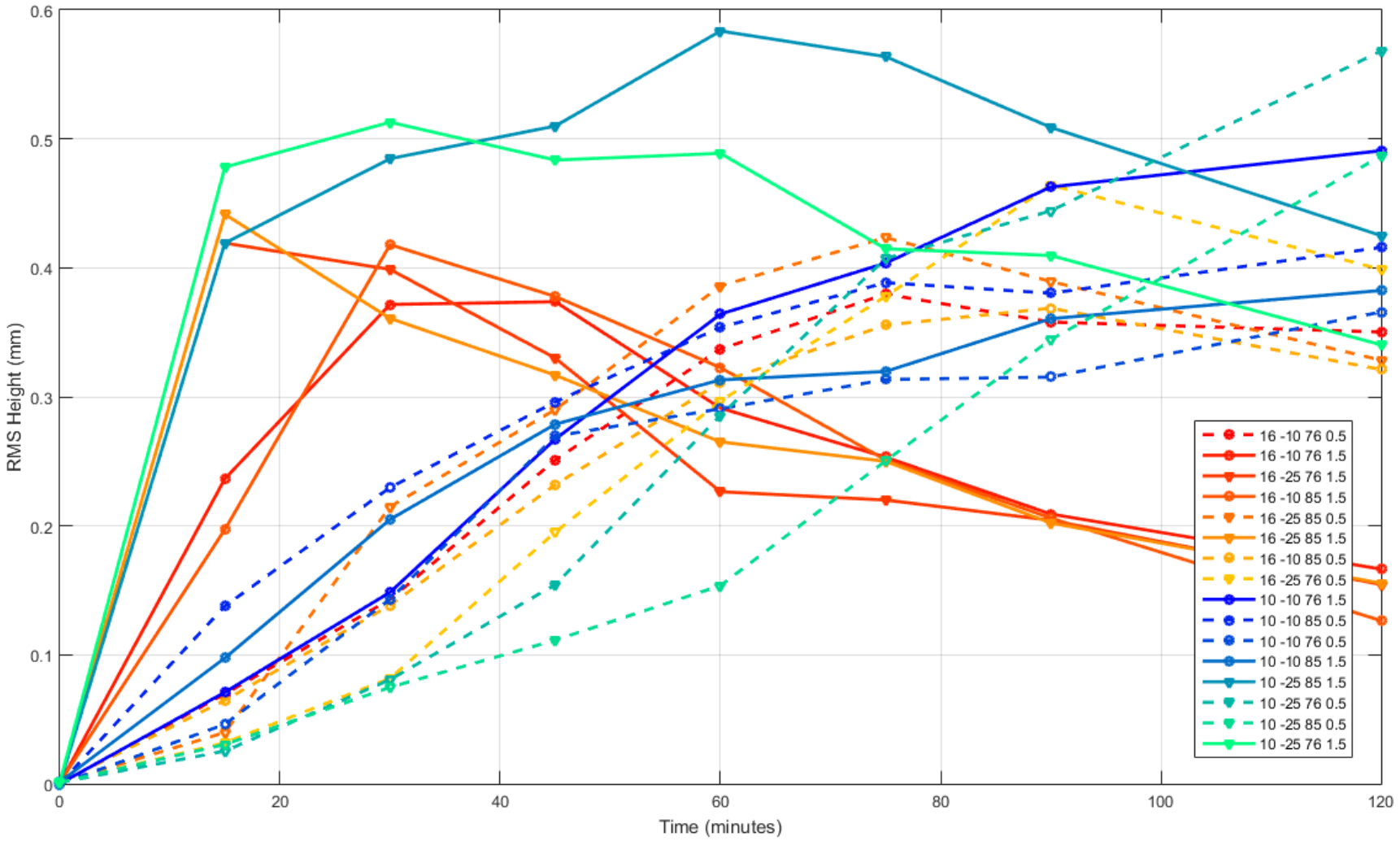

Figure 4.4: Frost RMS Height Evolution Results Highlighting Air Temperature and Air Velocity

Table 4.2: Frost Surface Roughness Parameter Results: Skewness

Test	Date (*yymmdd*)	Conditions *(AT_ST_RH_AV)*	Time						
			15 min	**30 min**	**45 min**	**60 min**	**75 min**	**90 min**	**120 min**
Base 1	180425	16_-10_76_0.5	1.661	1.238	1.375	1.017	0.617	0.32	0.003
Base 2	180523	10_-25_85_1.5	0.779	-0.248	-0.023	-0.007	-0.371	-0.164	0.067
3	180508	16_-10_76_1.5	0.982	0.355	-0.423	-0.597	-0.812	-1.101	-1.643
4	180508	16_-25_76_1.5	-0.262	-0.178	-0.102	-0.618	-0.821	-1.136	-1.365
5	180517	10_-10_76_1.5	0.982	0.654	1.11	0.841	0.718	0.638	0.204
6	180517	10_-10_85_0.5	1.785	0.778	0.477	0.612	0.804	0.295	0.528
7	180519	10_-10_76_0.5	2.136	1.365	1.617	1.32	1.061	1.038	0.585
8	180523	10_-10_85_1.5	1.13	0.317	1.093	0.965	0.894	0.735	0.271
9	180528	16_-10_85_1.5	1.511	0.341	-0.451	-0.651	-0.902	-1.42	-2.035
10	180529	16_-25_85_0.5	1.261	1.13	0.268	0.11	-0.327	-0.348	-0.404
11	180529	16_-25_85_1.5	-0.384	-0.337	-0.377	-0.386	-0.485	-0.683	-1.149
12	180604	10_-25_76_0.5	0.677	1.021	1.361	1.196	0.761	0.51	0.462
13	180604	10_-25_85_0.5	0.508	0.424	0.313	1.339	0.907	0.4	0.381
14	180606	16_-10_85_0.5	0.904	1.249	1.152	0.699	0.295	-0.008	-0.341
15	180606	16_-25_76_0.5	0.585	1.579	1.085	0.388	0.181	-0.007	-0.365
16	180611	10_-25_76_1.5	-0.271	-0.31	-0.366	-0.293	-0.196	-0.242	-0.259

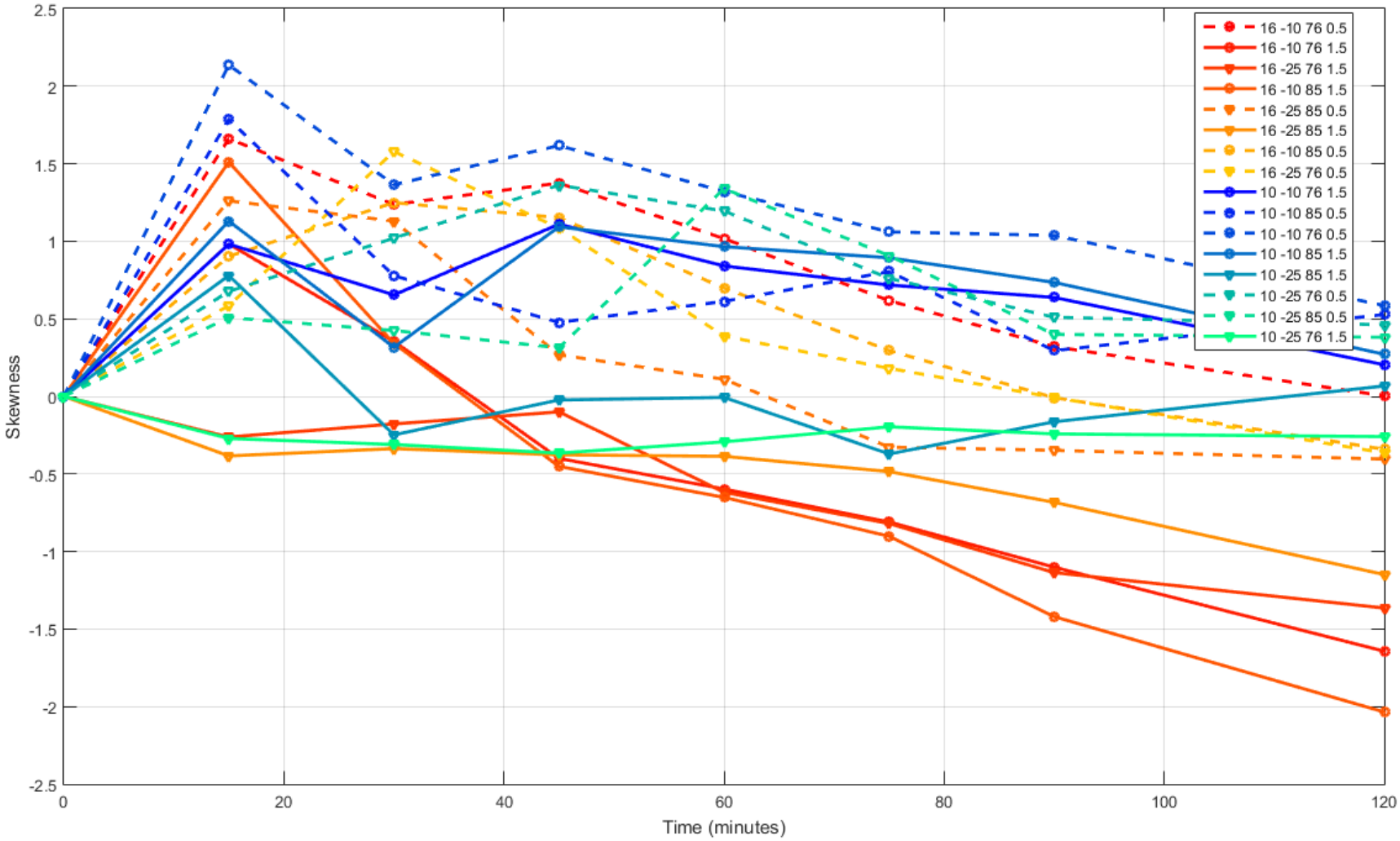

Figure 4.5: Frost Skewness Evolution Results Highlighting Air Temperature and Air Velocity

Table 4.3: Test Surface Parameter Results: Peak-to-Valley Height (mm)

Test	**Date** (*yymmdd*)	**Conditions** *(AT_ST_RH_AV)*	**Time**						
			15 min	**30 min**	**45 min**	**60 min**	**75 min**	**90 min**	**120 min**
Base 1	180425	16_-10_76_0.5	0.779	1.334	1.901	2.441	2.633	2.425	2.578
Base 2	180523	10_-25_85_1.5	2.316	3.313	3.389	4.033	4.715	3.931	3.567
3	180508	16_-10_76_1.5	1.594	2.089	2.067	2.05	1.92	1.843	1.351
4	180508	16_-25_76_1.5	2.779	3.187	2.523	1.639	1.82	1.913	1.425
5	180517	10_-10_76_1.5	0.533	1.041	1.783	2.175	2.702	2.97	3.163
6	180517	10_-10_85_0.5	0.953	1.413	1.919	2.637	3.171	2.833	3.094
7	180519	10_-10_76_0.5	0.532	1.206	1.925	2.363	2.303	2.285	2.564
8	180523	10_-10_85_1.5	0.783	1.711	2.387	2.83	2.779	3.077	2.94
9	180528	16_-10_85_1.5	1.587	2.175	2.175	2.229	2.104	1.952	1.38
10	180529	16_-25_85_0.5	0.602	2.266	2.198	2.797	3.14	3.281	2.754
11	180529	16_-25_85_1.5	2.846	3.134	2.828	2.078	2.152	1.643	1.364
12	180604	10_-25_76_0.5	0.361	0.782	1.755	2.11	3.126	2.605	3.62
13	180604	10_-25_85_0.5	0.438	0.633	0.912	1.729	1.868	2.402	3.527
14	180606	16_-10_85_0.5	0.641	1.343	1.866	2.204	2.648	2.474	2.637
15	180606	16_-25_76_0.5	0.365	1.259	1.627	2.852	2.486	2.822	2.976
16	180611	10_-25_76_1.5	2.635	3.286	3.687	3.869	3.51	3.812	2.988

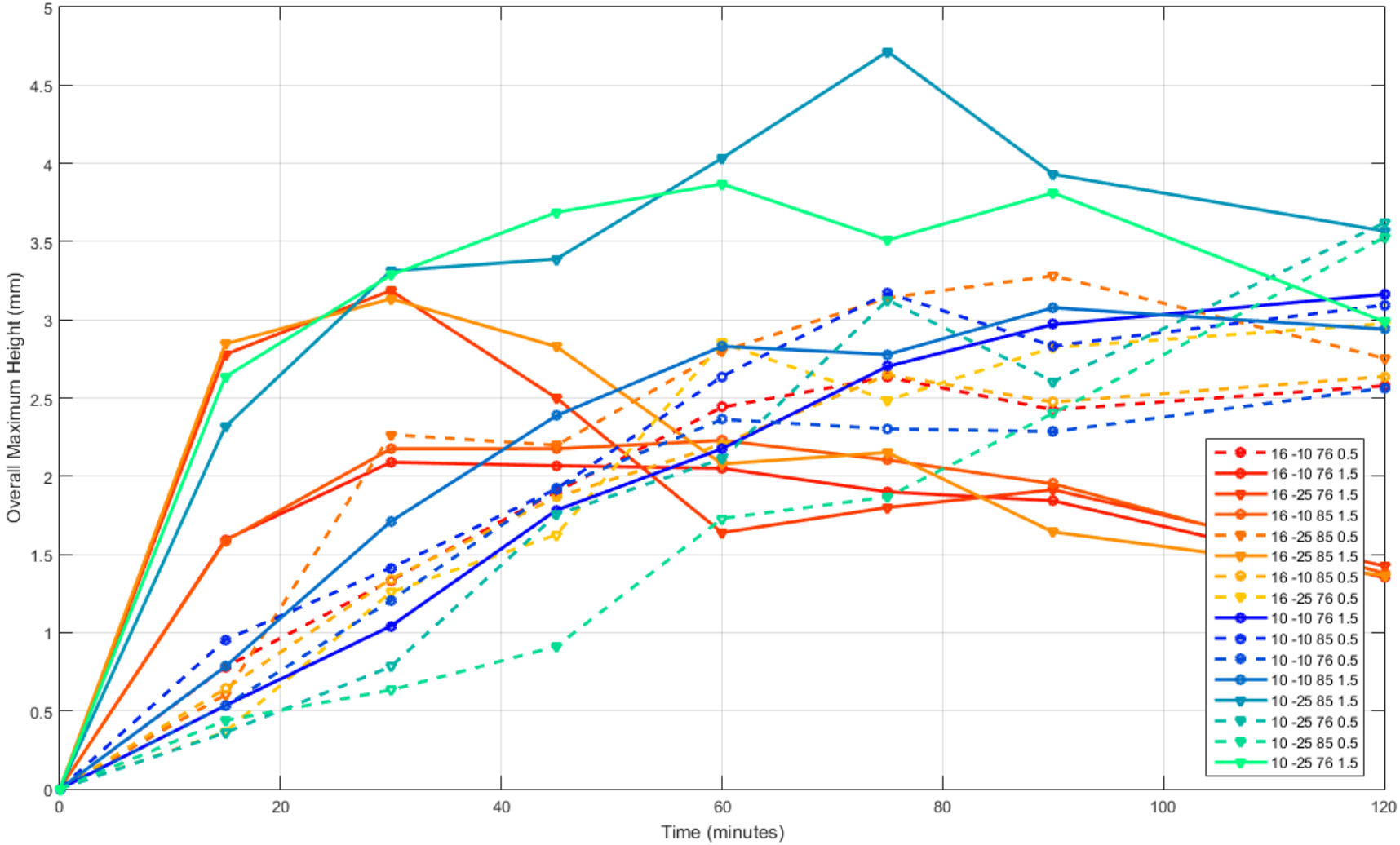

Figure 4.6: Frost Peak-to-Valley Height Evolution Results Highlighting Air Temperature and Air Velocity

ANOVA Results In review of the frost roughness parameter measurements, the statements made about the effect of the atmospheric conditions on the frost formations may be reinforced by ANOVA statistical significance. Statistical p-values were calculated based on the development rates of RMS, peak-to-valley height, and skewness. These development rates were formulated from the slopes of best fit lines for each of the roughness parameters and displayed in Table 4.5. The slopes were used for statistical assessment because they incorporate measurements of greatest concern (turnaround time frame of aircraft), and factor in frost dendrite growth rate and maximum frost roughness height. In this statistical analysis, a hierarchal order of environmental influence on frost roughness may be observed in Table 4.4. The results demonstrate that between the time of 30 and 75 minutes, the air temperature and air velocity had the highest governing effect on frost roughness formation. Statistically speaking, a p-value less than 0.05 indicates a significant test variable that heavily influenced frost roughness formation. The assessment also determined if certain test variables resulted in significant interaction effects. The table demonstrates that the air velocity effected both the surface and air temperature.

Table 4.4: ANOVA P-Values of Development Rates of
Frost Roughness Parameters for 30 to 75 Minutes

Environmental Test Variable	**P-value**
Air Temperature	0.00030
Air Velocity	0.00379
Interaction Affect: Air Velocity / Air Temperature	0.03571
Surface Temperature	0.03999
Interaction Affect: Air Velocity / Surface Temperature	0.04285
Relative Humidity	0.11100

Table 4.5: Frost Surface Roughness Parameter Development Rate (30 to 75 minutes) Results

Test	**Date** (*yymmdd*)	**Conditions** *(AT_ST_RH_AV)*	**Parameter**		
			RMS Height *(mm/min)*	**Skewness** *(1/min)*	**Peak-to-Valley** *(mm/min)*
Base 1	180425	16_-10_76_0.5	5.31E-03	-1.61E-02	2.96E-02
Base 2	180523	10_-25_85_1.5	2.07E-03	1.68E-03	3.23E-02
3	180508	16_-10_76_1.5	-2.92E-03	-2.03E-02	-3.89E-03
4	180508	16_-25_76_1.5	-4.27E-03	-1.51E-02	-3.35E-02
5	180517	10_-10_76_1.5	5.75E-03	-6.82E-03	3.58E-02
6	180517	10_-10_85_0.5	3.56E-03	-2.45E-03	3.99E-02
7	180519	10_-10_76_0.5	3.55E-03	-1.01E-02	2.49E-02
8	180523	10_-10_85_1.5	2.52E-03	-3.22E-03	2.43E-02
9	180528	16_-10_85_1.5	-3.70E-03	-2.49E-02	-1.07E-03
10	180529	16_-25_85_0.5	4.81E-03	-1.56E-02	2.15E-02
11	180529	16_-25_85_1.5	-2.56E-03	-8.91E-03	-2.47E-02
12	180604	10_-25_76_0.5	7.40E-03	-9.47E-03	4.92E-02
13	180604	10_-25_85_0.5	3.79E-03	-1.26E-03	3.02E-02
14	180606	16_-10_85_0.5	4.87E-03	-1.93E-02	2.84E-02
15	180606	16_-25_76_0.5	6.60E-03	-2.13E-02	3.27E-02
16	180611	10_-25_76_1.5	-1.93E-03	1.09E-03	5.69E-03

Equivalent Sand-Grain Roughness Application. The RMS, peak-to-valley height and skewness are beneficial for understanding the effects of the atmospheric conditions, but these parameters are not the final application for aerodynamic analysis. Therefore, the equivalent sand-grain roughness heights were calculated and displayed in Table 4.6. Figure 4.7 also displays the results in a plot highlighting the variations in the air temperature and the air velocity. One distinct trend to observe is: before 30 minutes the frost formations with the faster air velocity had a greater roughness (on average), but after 30 minutes the slower air velocity demonstrated higher roughness values. This is important because a commercial airplane's turnaround time can take anywhere from 20 minutes to over an hour, therefore knowing the air velocity is crucial because it can mean the difference between an insignificant frost roughness or a critical frost contamination. Furthermore, results from the 10 °C air temperatures tend to have a higher equivalent sand-grain roughness, thereby indicating that colder air temperatures create a more hazardous condition for cold-soaked fuel frost on aircraft wings. It is important to note that these trends in the data are weak in relationship. Further testing and analysis would need to be performed to declare these observations as conclusive.

Table 4.6: Test Surface Parameter Results: Equivalent Sand-Grain Roughness (mm)

Test	**Date** (*yymmdd*)	**Conditions** *(AT_ST_RH_AV)*	**Time**						
			15 min	**30 min**	**45 min**	**60 min**	**75 min**	**90 min**	**120 min**
Base 1	180425	16_-10_76_0.5	1.181	1.909	3.637	3.904	3.25	2.32	1.558
Base 2	180523	10_-25_85_1.5	4.088	1.452	2.188	2.562	1.322	1.764	2.058
3	180508	16_-10_76_1.5	2.675	2.495	0.822	0.371	0.115	-0.016	-0.16
4	180508	16_-25_76_1.5	1.225	1.351	1.265	0.268	0.093	-0.023	-0.068
5	180517	10_-10_76_1.5	0.803	1.311	3.293	3.722	3.753	4.029	2.803
6	180517	10_-10_85_0.5	2.483	2.239	2.239	3.016	3.863	2.401	3.292
7	180519	10_-10_76_0.5	0.978	2.062	4.461	4.081	3.739	3.704	3.046
8	180523	10_-10_85_1.5	1.218	1.323	3.398	3.501	3.396	3.397	2.354
9	180528	16_-10_85_1.5	3.084	2.768	0.735	0.338	0.046	-0.11	-0.233
10	180529	16_-25_85_0.5	0.54	2.681	1.78	1.973	1.09	0.96	0.715
11	180529	16_-25_85_1.5	1.007	0.911	0.734	0.602	0.446	0.185	-0.02
12	180604	10_-25_76_0.5	0.229	0.938	2.22	3.715	3.916	3.46	4.233
13	180604	10_-25_85_0.5	0.238	0.538	0.717	2.181	2.686	2.419	3.354
14	180606	16_-10_85_0.5	0.693	1.863	2.936	2.852	2.246	1.615	0.803
15	180606	16_-25_76_0.5	0.265	1.325	2.365	2.061	2.102	2.035	0.948
16	180611	10_-25_76_1.5	1.373	1.365	1.148	1.346	1.362	1.242	0.999

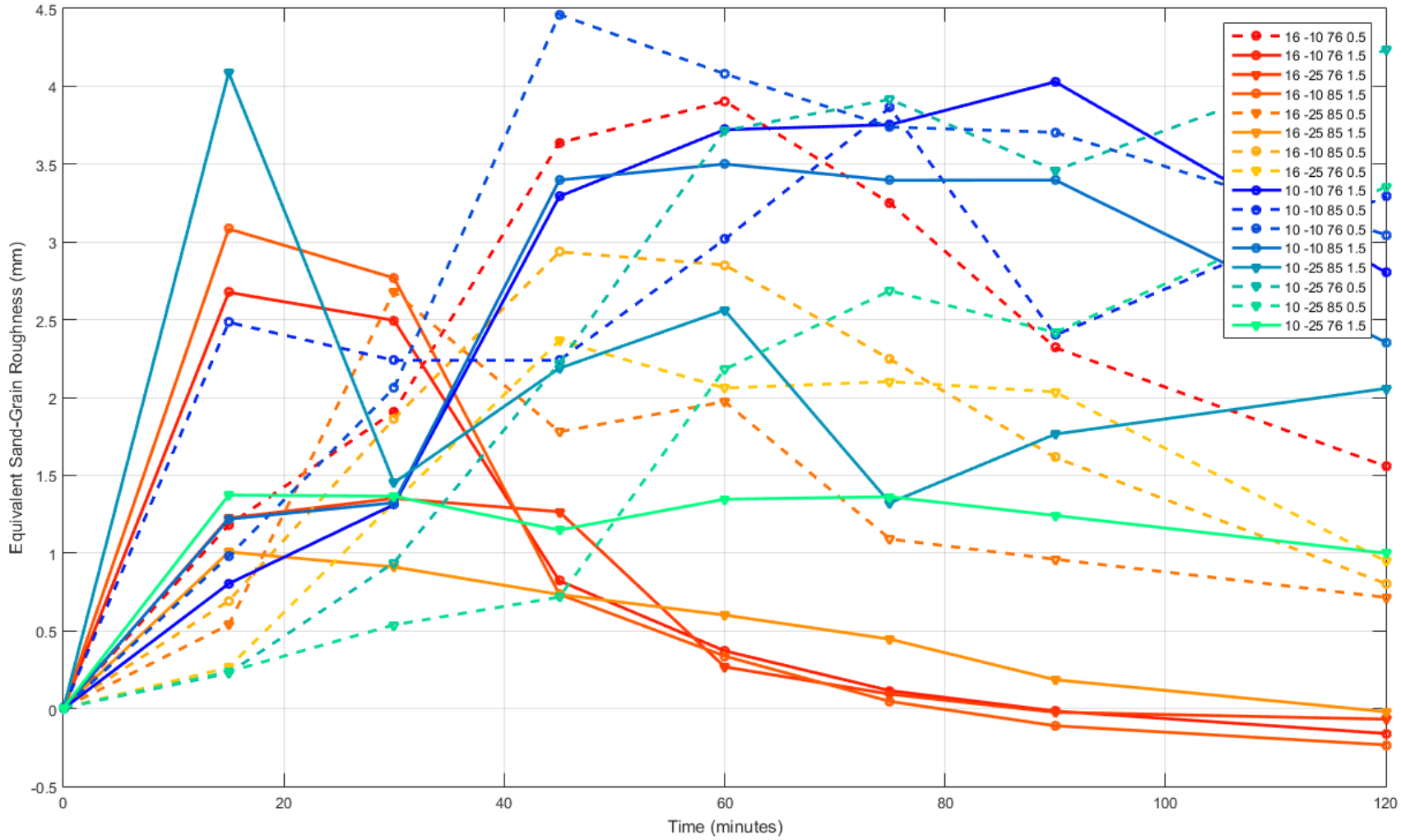

Figure 4.7: Equivalent Sand-Grain Roughness Evolution ANOVA Results Highlighting Air Temperature and Air Velocity

Initial Frost Development Results

Another dominating factor not clearly seen in the figures above is the surface temperature. The surface temperature had the most impact on the frost roughness formation in the first 30 minutes because frost was developing near the surface during this time. Figure 4.8 through Figure 4.11 highlight the effects of the surface temperatures and air velocities for the 16 different test combinations for ANOVA assessment. The data in the following figures is the same as the previous section, but now the blue/green lines represent a -25 °C surface temperature and the red/yellow/orange lines represent -10 °C. The most prominent aspect to note in Figure 4.8 through Figure 4.10 is the combined effect of the -25 °C surface temperature and the 1.5 m/s air velocity, producing rapidly developed frost dendrites. The unique characteristic of those initial frost dendrites is attributed to the rapid accumulation and freezing of water vapor that produced tall and thick frost dendrites. The tall height of those frost formations is reflected in the high RMS values while the thickness or density of the frost dendrites closely packed together is reflected by the negative skewness values. For a visual explanation of these observations see Figure 4.14. On the contrary, the initial frost formations for the -25 °C surface temperature and the 0.5 m/s air velocity produced less rough frost dendrites that were shorter and very dense near the test surface. Once again this is reflected by shorter RMS heights and positive skewness values. Since it was previously observed that the air velocity influenced the growth rate of the frost dendrites, it may now be concluded that the surface temperature affected the initial thickness and density of the frost. Moreover, by the time the frost had developed for 45 minutes the effects of the surface temperature had decreased due to the frost growing away from the surface and the air temperature began to have a more significant impact.

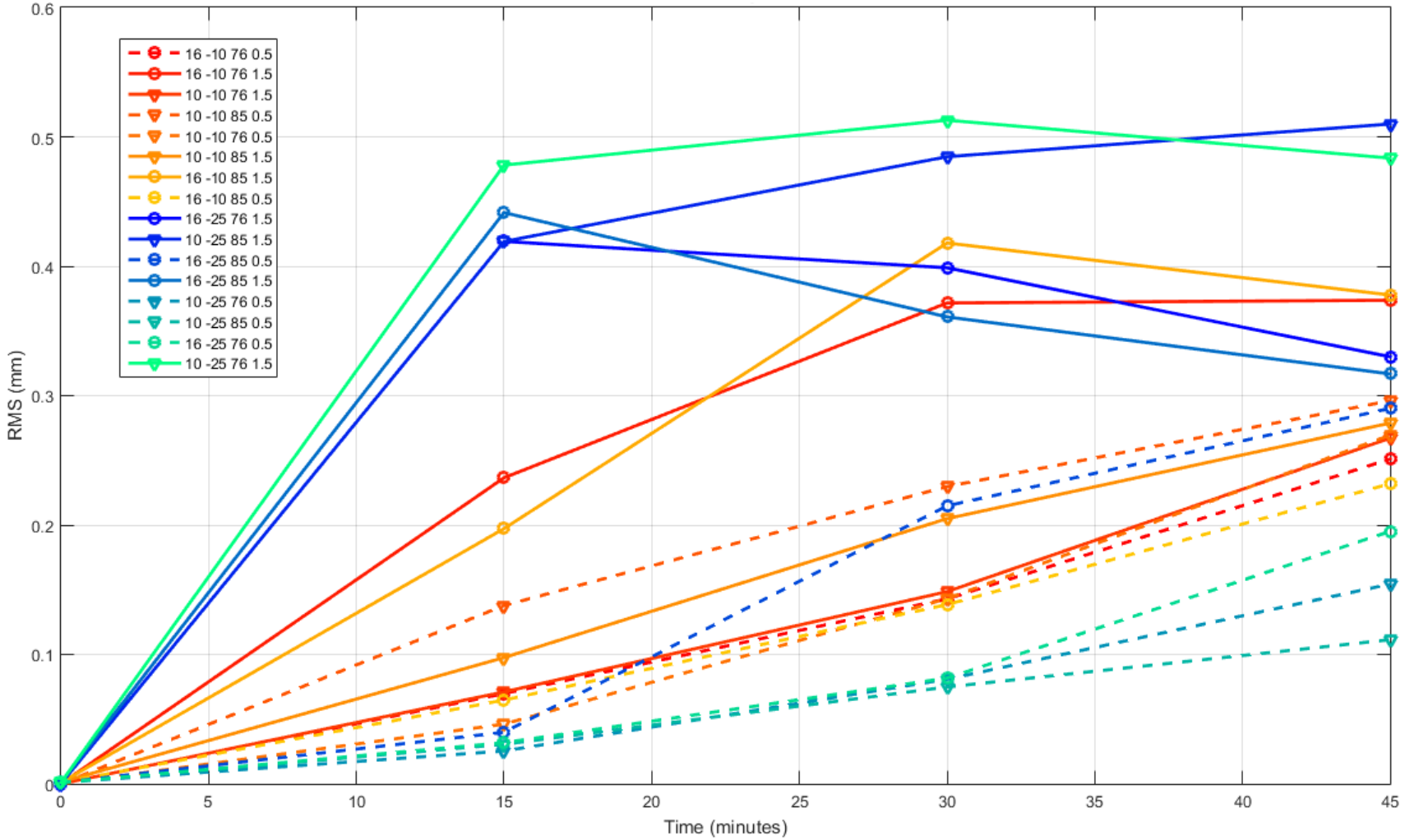

Figure 4.8: Frost RMS Height Evolution ANOVA Results Highlighting Surface Temperature and Air Velocity

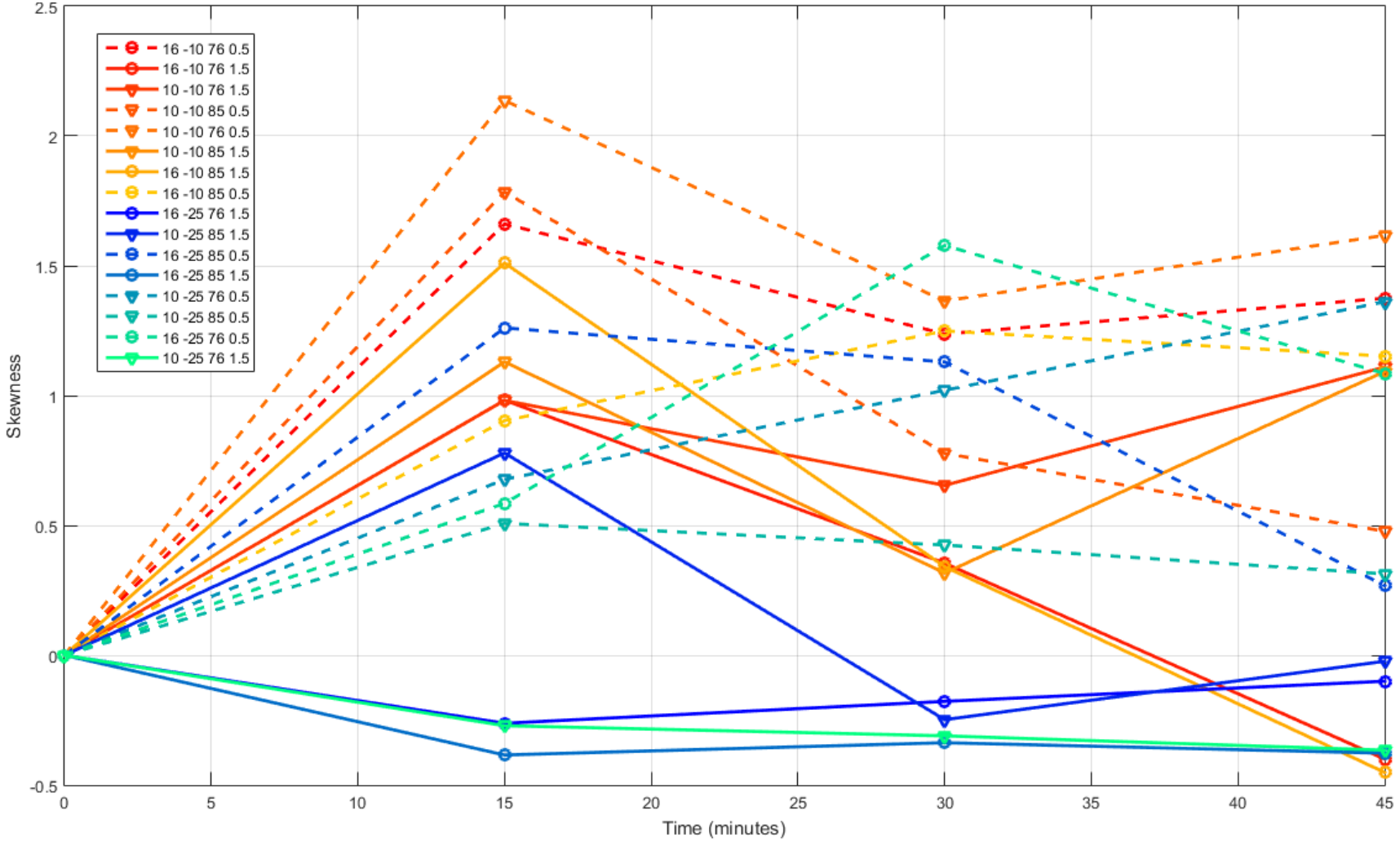

Figure 4.9: Frost Skewness Evolution ANOVA Results Highlighting Surface Temperature and Air Velocity

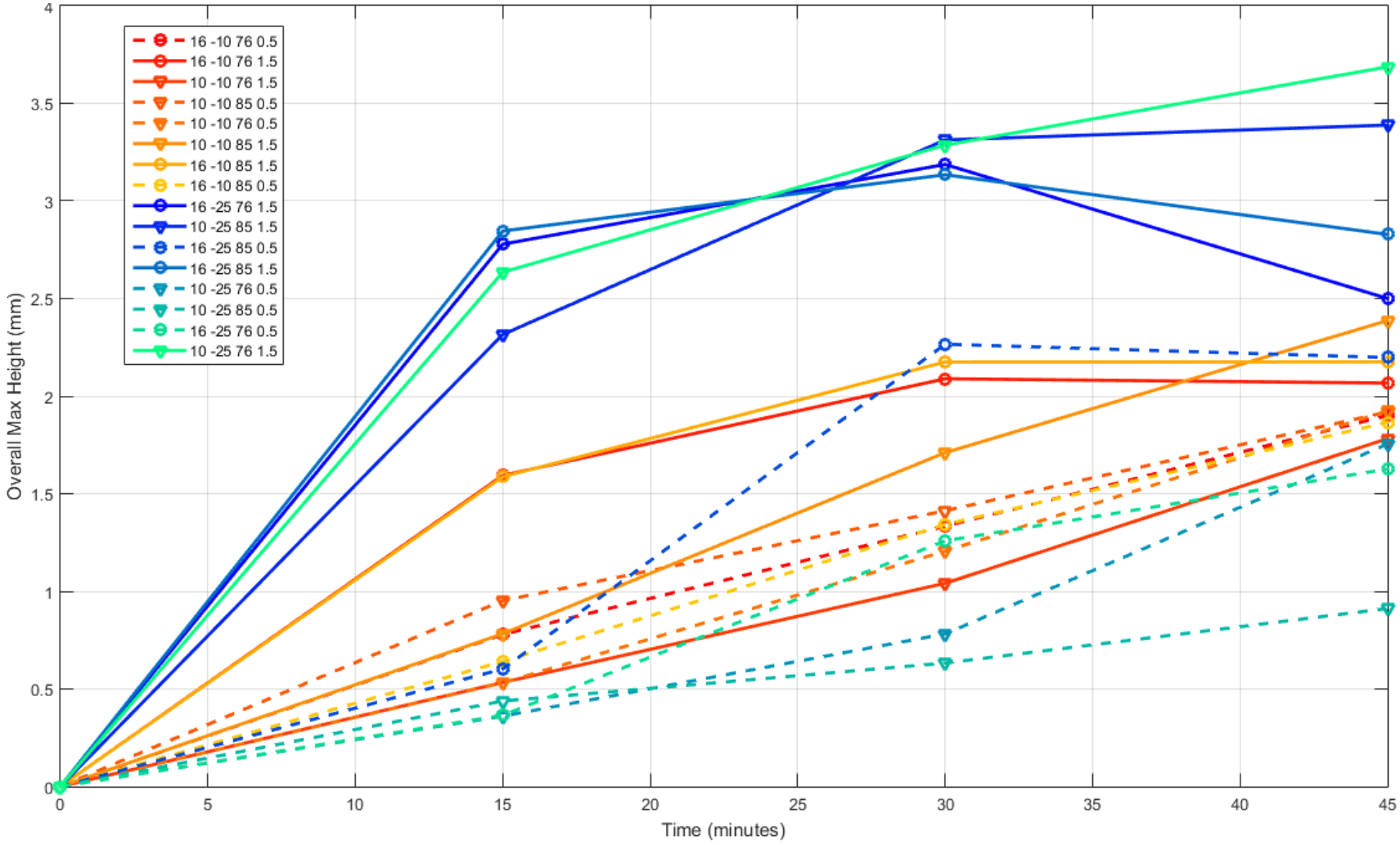

Figure 4.10: Frost Peak-to-Valley Height Evolution ANOVA Results Highlighting Surface Temperature and Air Velocity

ANOVA Results To reinforce the conclusions made about the effects of surface temperature and air velocity, the ANOVA p-values of the initial development rates for the measured roughness parameters were calculated and presented in a hierarchal order (Table 4.7). These development rates were calculated for the first 15 minutes because they most clearly portray the significance of the test variables during the initial formation of frost. Similar to the results from the previous ANOVA assessment, these p-values demonstrate that air velocity had a significant effect on frost roughness formation and also effects surface and air temperature. The table also portrays that the surface temperature was a more significant factor than air temperature in the initial frost formation as expected. Once again, the relative humidity appeared to have the least amount of effect on the specific characteristics of the frost roughness.

Table 4.7: ANOVA P-Values of Development Rate of
Frost Roughness Parameters for 0 to 15 Minutes

Environmental Test Variable	**P-value**
Air Velocity	0.00024
Interaction Affect: Air Velocity / Surface Temperature	0.00125
Surface Temperature	0.00541
Interaction Affect: Air Velocity / Air Temperature	0.09661
Air Temperature	0.12163
Relative Humidity	0.24110

Equivalent Sand-Grain Roughness Application. Although the general effects of the surface temperature are not very distinguishable in the equivalent sand-grain roughness plot of Figure 4.11, the data still presents valuable application. Because there are no evident trends, the data demonstrates that the surface temperature is not as significant in predicting frost roughness in comparison to air temperature and velocity. However, a slight trend may be observed that the 10 °C surface temperature results (on average) in a larger equivalent sand-grain roughness. Theoretically because the colder surface temperature increased the initial frost thickness and density, a warmer surface temperature resulted in frost dendrites that were not as close to the critical height in the viscous boundary layer giving them more room to grow, which corresponds to a higher equivalent sand-grain roughness. Regardless of this trend, surface temperature is not a sufficient, sole predictor of frost roughness patterns. Additionally, when cold-soaked fuel frost occurs, measuring the exact surface temperature may not always be accessible or practical. Because air temperature and air velocity are the heaviest factors in determining frost roughness, these variables are two of the most important parameters for predicting and determining if atmospheric conditions are safe for takeoff with cold-soaked fuel frost.

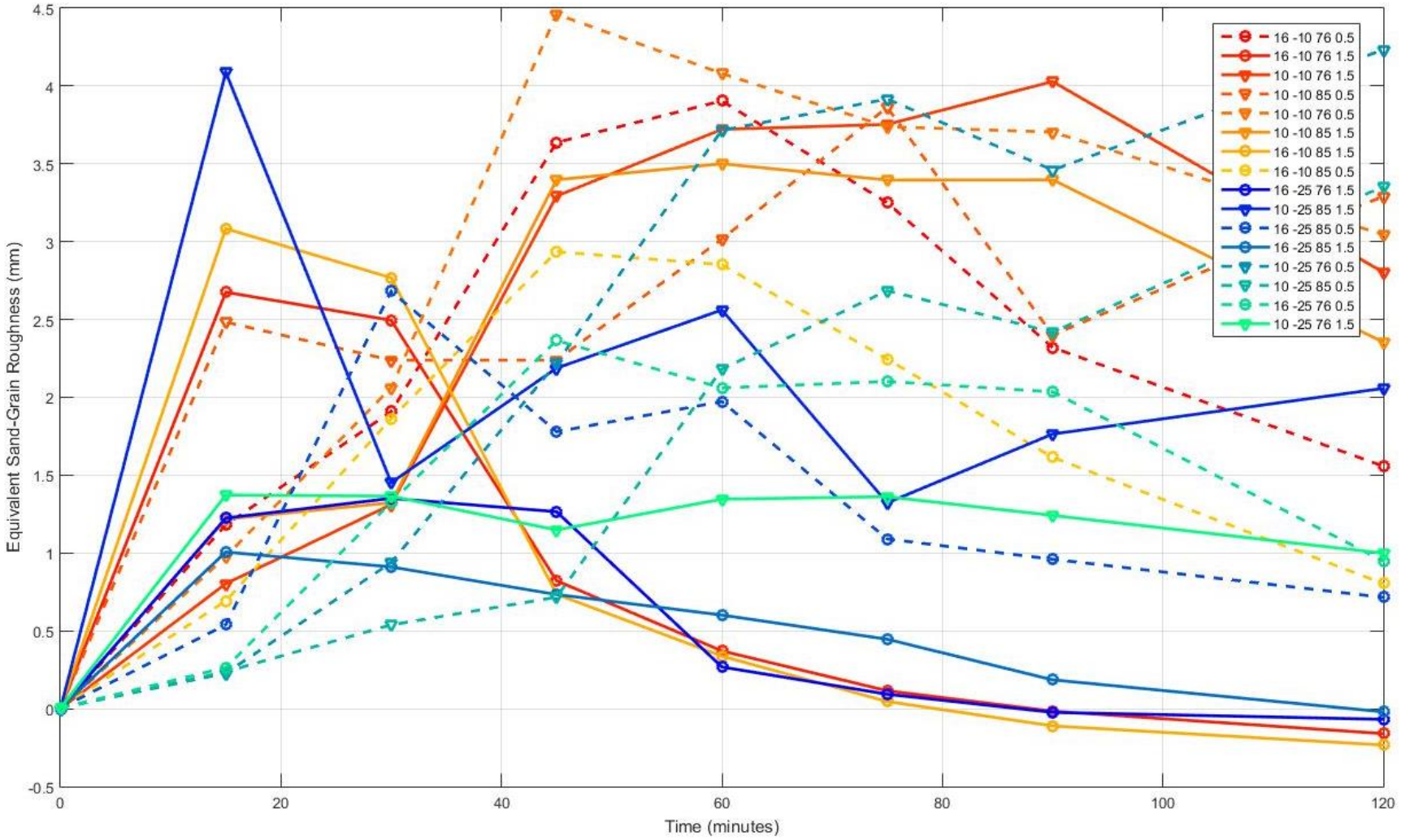

Figure 4.11: Equivalent Sand-Grain Roughness Evolution ANOVA Results Highlighting Surface Temperature and Air Velocity

ANOVA Summary

In summation of the ANOVA experiment, surface temperature affects the initial density and thickness of the frost; air temperature influences the maximum allowable height of the frost dendrites and air velocity mainly determines the development rate of the frost dendrites. All three of these atmospheric factors interact with one another to form various frost roughness formations, but the air temperature and air velocity have the greatest governing effects on the roughness during the turnaround timeframe of an aircraft.

Air Temperature vs Air Velocity

Sensitivity Analysis

Although the results from the ANOVA tests, clearly indicate that the air temperature and air velocity are the most significant factors in effecting the frost roughness, the sensitivity and predictability at various conditions is not clearly portrayed. Therefore, the completed tests were subdivided into groups based on air temperature and air velocity. Figure 4.12 displays four groups of evolution time plots each with a base test condition and corresponding atmospheric perturbations. These perturbations include relative humidity (ΔRH) = +9%, and surface temperature (ΔST) = -15 °C. The main suggestion from the results is that a warmer air temperature (16 °C) and a faster air velocity (1.5 m/s) result in a frost formation that is less sensitive to atmospheric changes, while a colder air temperature (10 °C) and a slower air velocity (0.5 m/s) demonstrates more susceptibility to changes in frost formation. Furthermore, since it will be required to predict the equivalent sand-grain roughness on cold-soaked fuel frosted wings, the measurements for colder air temperatures and slower air velocities will be more difficult to predict because each of the perturbations demonstrates significant deviation.

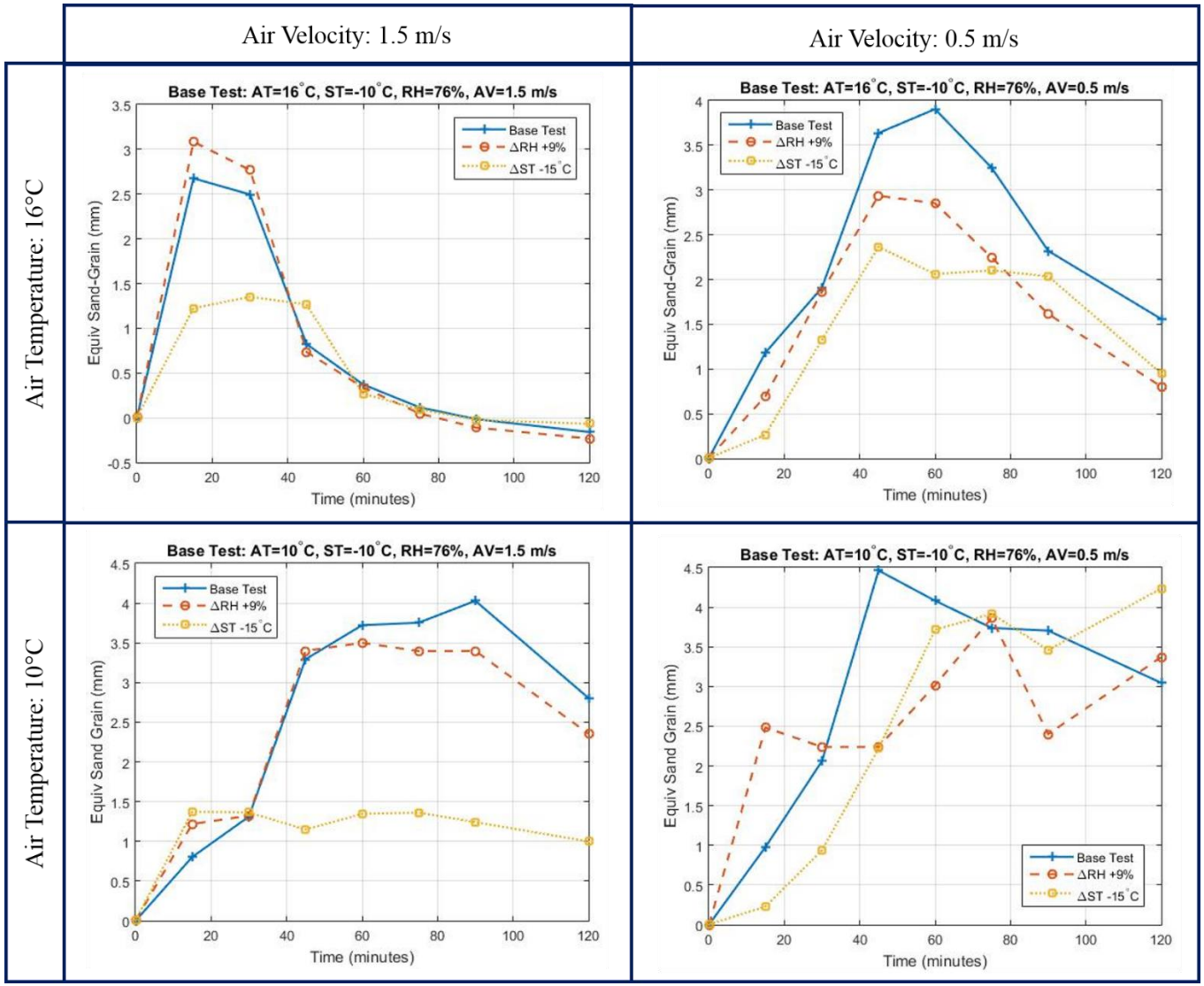

Figure 4.12: Air Velocity vs Air Temperature Sensitivity Results – Roughness Evolution Plots

Interaction Effects

Figure 4.13 presents the detailed height distributions from the base tests of Figure 4.12 for the times of 30 and 60 minutes. A distinct distribution presented for the 16 °C air temperature and 1.5 m/s air velocity, is the glazed over frost surface that resulted from densification. Even though this height distribution has an equal peak-to-valley height at the corresponding 10 °C air temperature case, the resulting equivalent sand-grain roughness is not as severe, mainly because of the 16 °C test condition's negative skewness. However, a more critical frictional drag resulted from the large, feathery frost dendrites for the colder air temperature (10 °C) and slower air velocity (0.5 m/s) condition. The frost dendrites at this condition continued to grow, without any clear indication of reaching a critical height in the boundary layers. This is reflected in the relatively high equivalent sand-grain roughness plot of Figure 4.12. This affirms that a critical case of cold-soaked fuel frost roughness is for colder air temperatures with slower air velocities. If an aircraft is in environmental conditions where frost dendrites continue to grow without redensification, the resulting skin friction will continue to increase until an environmental change causes the dendrites to melt or collapse.

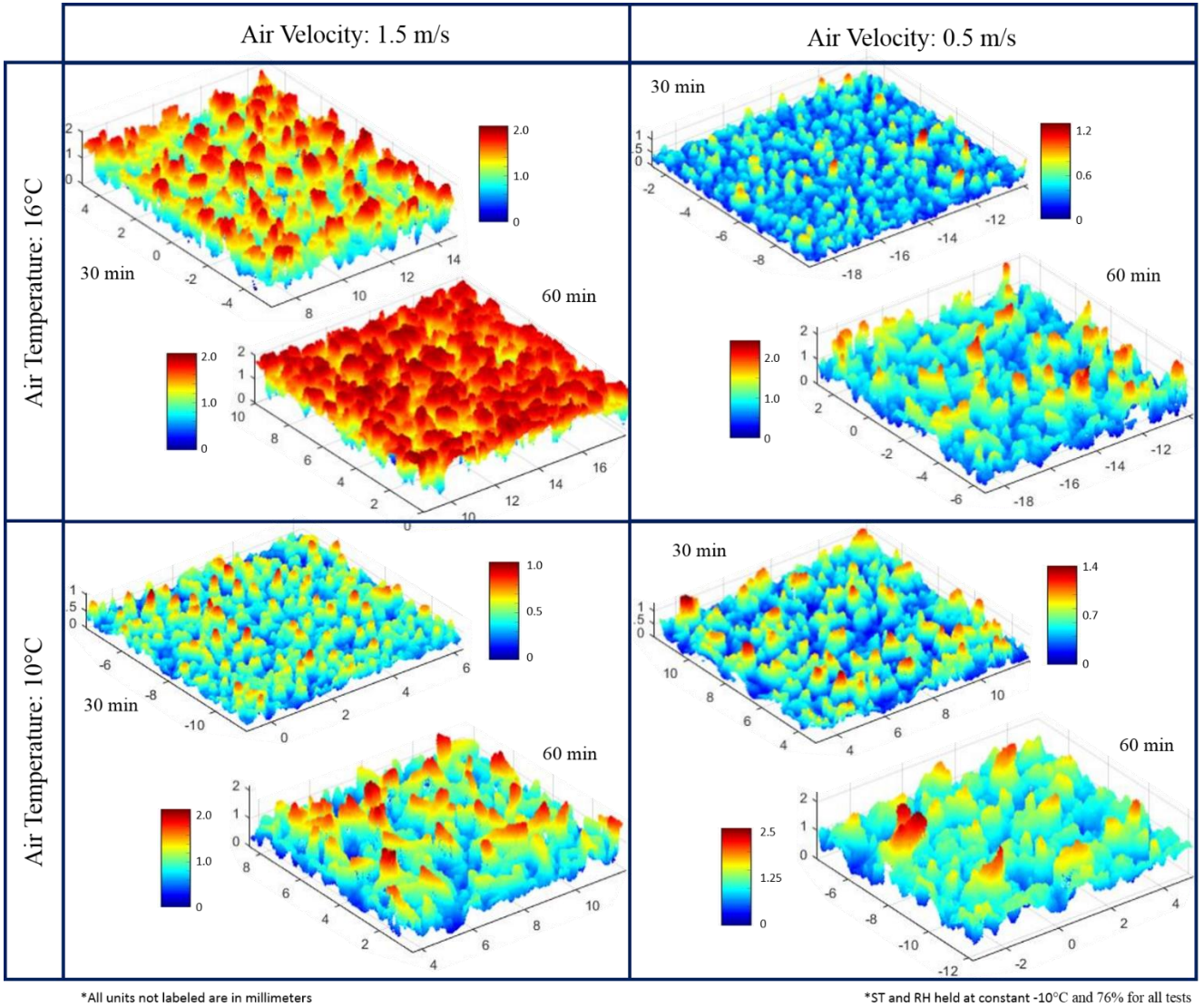

Figure 4.13: Air Velocity vs Air Temperature – Detailed Distributions at 30 and 60 min.

Interaction Effects

Another condition of interest is the interaction effect between surface temperature and air velocity. Figure 4.14 displays the detailed height distributions for four distinct conditions all with a constant air temperature of 16 °C. These distributions present a wide range of various types of frost formation. A distinct distribution is the roughness for the 1.5 m/s air velocity and -25 °C surface temperature. This condition presents one of the highest initial RMS heights, but a smaller equivalent sand-grain roughness value. This demonstrates that a frost layer may be thick and incur more form drag than frictional drag. Furthermore, the detailed height distribution at 60 minutes for this condition is similar to the corresponding distribution for the surface temperature of -10 °C. This agrees with the previous statement that air temperature dictates the frost formation more heavily than surface temperature after 30 minutes. A final observation clearly seen for both surface temperatures is that a difference in air velocity of 1.0 m/s determined the alteration between rapid initial frost formation with densification (1.5 m/s) and a slow frost growth with no densification (0.5 m/s).

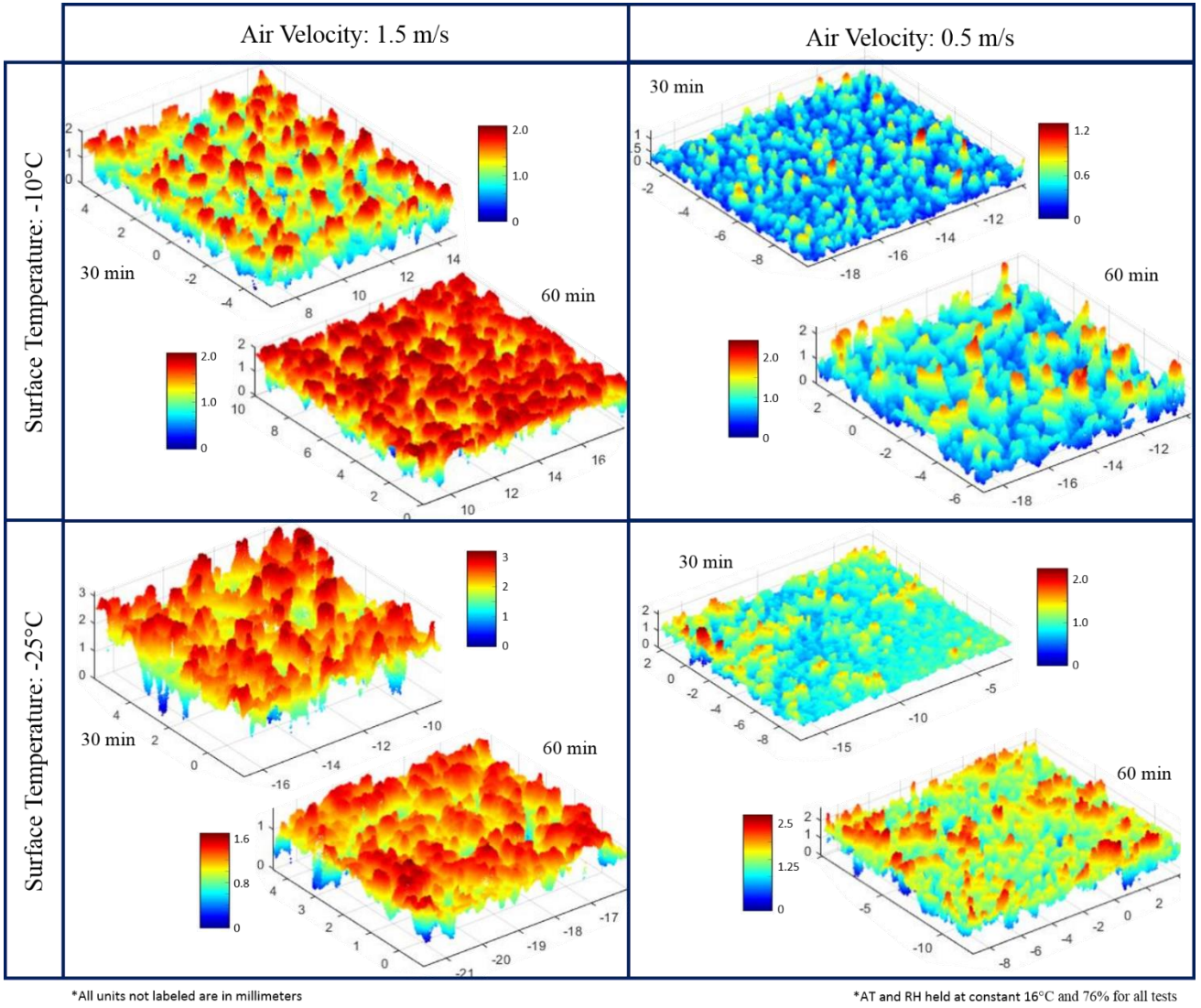

Figure 4.14: Air Velocity vs Surface Temperature – Detailed Distributions at 30 and 60 min.

Relative Humidity

For completeness, the relative humidity was also individually assessed to confirm that it had the least amount of impact on frost roughness. Figure 4.15 displays the minimal variation in RMS heights between varying humidity levels. An important clarification to make is that even though the relative humidity had little effect on the frost roughness development, the humidity level must be high enough to enable a dew point for water vapor to saturate on the test surface, otherwise there will be no frost formation.

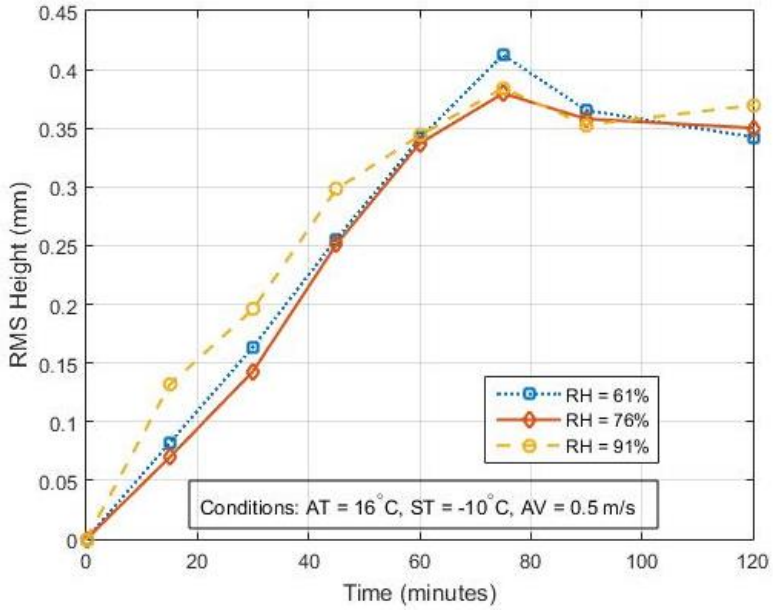

Figure 4.15: Relative Humidity Sensitivity Results – Roughness Evolution Plot

Critical Frost Case

Air Velocity

From the results and discussion presented in the previous sections, one of the more critical conditions to an aircraft's takeoff with cold-soaked fuel frost is environments with colder air temperatures and slower air velocities. Since air velocity was determined to be the most significant factor in governing frost roughness formation, it was individually

assessed to understand its full ramification. Figure 4.16 displays the roughness evolution for four tests with different air velocities. For a faster velocity (5.0 m/s) the frost demonstrated no aerodynamic roughness values of concern. This is visually confirmed in Figure 4.17 which displays a fairly smooth frost surface for the air velocity conditions of 5.0 m/s at 30 minutes. It may be concluded that if the air velocity is high enough, the resulting cold-soaked fuel frost will have negligible effect on the skin friction of an aircraft. However, for slower air velocities (0.5 m/s and 1.0 m/s) the resulting frost roughness heights were much more critical. The maximum equivalent sand-grain values for these slower air velocities were about equal but developed at different rates. In application to aerodynamics, if an aircraft forms CSFF at slower air velocities, the resulting roughness will increase the friction drag of the airplane wings to higher levels of concern. However, it would be beneficial to have a quick turnaround time as this will decrease the degradation on the angle of attack and lift coefficient.

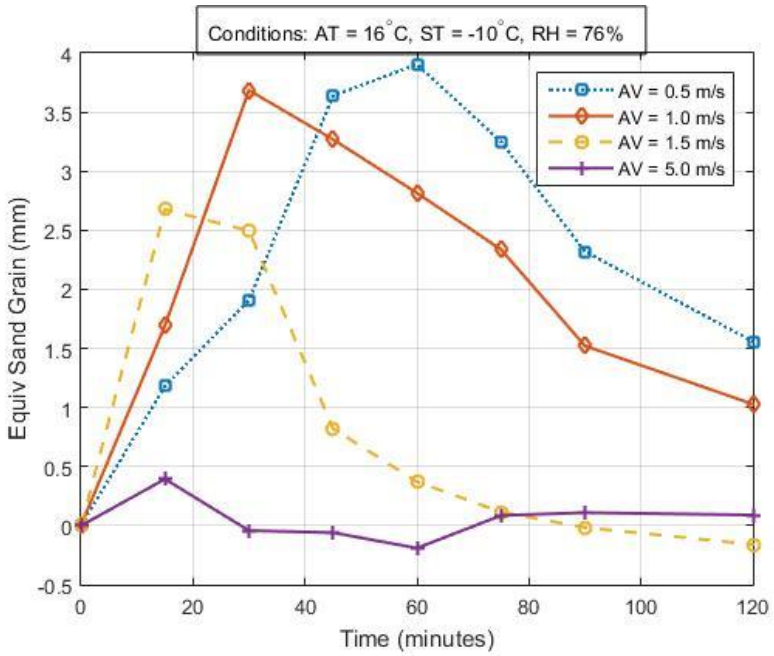

Figure 4.16: Air Velocity Sensitivity Results – Roughness Evolution Plot

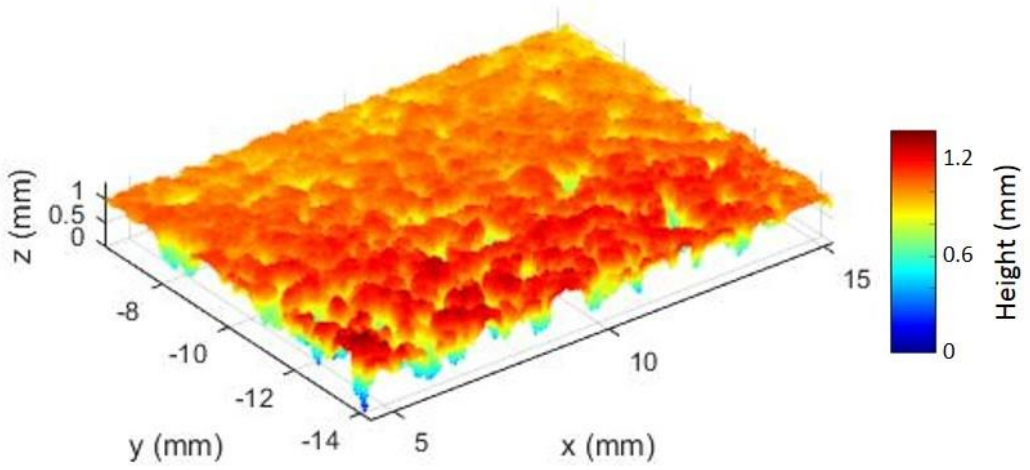

Figure 4.17: Air Velocity Sensitivity Results –
Detailed Distribution of AV = 5.0 m/s at 30 Minutes

Air Temperature

Additional testing was conducted at air temperatures colder than 16 °C with a velocity of 0.5 m/s because this environment demonstrated the highest maximum sand-grain roughness out of all previous conditions. Figure 4.18 demonstrates that as air temperatures decrease the resulting frictional drag from cold-soaked fuel frost increases. In these conditions, the decrease of 6 °C air temperature resulted in an increase in a maximum sand-grain roughness height of about 0.5 mm. For the coldest temperature, the frost formation developed to a sand-grain roughness value near 4.5 mm. However, Figure 4.18 also portrays that frost equivalent sand-grain roughness rapidly reached its peak value before decreasing. Once again this suggests that a method to decrease the risk of CSFF takeoffs is through fast turnaround time.

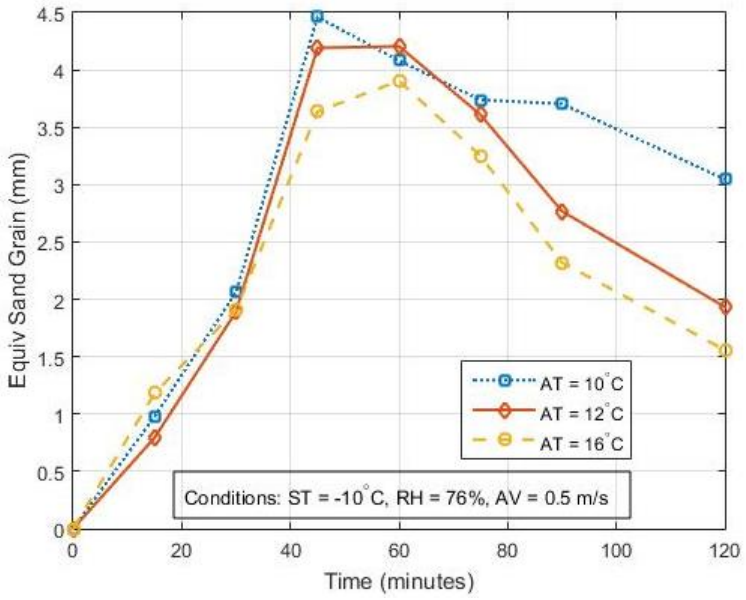

Figure 4.18: Air Temperature Sensitivity Results – Roughness Evolution Plot

Summary

Because of the general trends observed from all the results, the following conclusions may be stated. First, the relative humidity has minor effects on frost roughness formation. Second, colder surface temperatures may increase the initial frost density and thickness, but this gives no clear prediction on the frost roughness during the average aircraft turnaround time frame. Last and most importantly, the air temperature and air velocity have the greatest governing effect on frost roughness. As the air temperature and air velocity decrease, the frost's peak value of equivalent sand-grain roughness intensifies, which results in an increased skin friction coefficient that may be above a safe frictional drag. However, a quick turnaround time decreases the magnitude of aerodynamic degradation experienced for colder air temperatures and slower air velocities.

CHAPTER FIVE

Conclusions

Cold-soaked fuel frost degrades the aerodynamic performance of an aircraft. Therefore, the FAA has restricted the takeoff of airplanes with CSFF, unless a certification exemption for a specific aircraft model is granted. To assist the FAA in evaluating exemption requests and airframe manufacturers in design of airplane wings, the characteristics and roughness evolution of frost must first be measured and assessed. This chapter summarizes the research efforts and results of measuring and analyzing frost roughness. This section also discusses future work to simulate and measure CSFF on aircraft wings and efforts to create a prediction model from the measurements.

Summary of Work

A new method was created and verified to measure transient surface roughness using micro photogrammetry in application to cold-soaked fuel frost accumulation on the wings of aircraft. The method uses a non-invasive, aerial top-down system incorporating a camera mounted to a telescoping boom that enables perspective change for capturing multiple data images. The frost was formed within a closed-loop, psychrometric wind tunnel with controlled air temperature, air velocity, relative humidity and surface temperature. The camera captured the data in-situ with targets defined by a scale bar placed streamwise to the test surface. The data images were processed in a photogrammetric software creating a 3D point cloud model, which was constrained to the correct planar size using a horizontal measurement and scaled to the correct height using an iterative

numerical method. Detailed height topography measurements of the frost surfaces were made from the point clouds. Additionally, the resulting surface roughness parameters obtained from the photogrammetric frost models included root-mean-square height, skewness, peak-to-valley height and equivalent sand-grain roughness. The measurements were analyzed to determine the effects and trends that each environmental factor had on the frost roughness formation. Further, the aerodynamic impacts of the roughness results were discussed in reference to cold-soaked fuel frost.

Atmospheric test conditions were established and operated within the wind tunnel to match the environmental conditions of recorded occurrences of cold-soaked fuel frosted aircraft. The wind tunnel tests resulted in transient frost roughness measurements that were assessed in an ANOVA statistical experiment. The results indicate the most significant atmospheric factors and environmental interaction effects. Each atmospheric factor was then further assessed through grouped test conditions to give a deeper understanding of the trends, sensitivity and interactions observed. The newly established photogrammetric method and critical discoveries of this study are described in the following paragraphs.

Photogrammetric Measuring Method

The micro, structure-from-motion photogrammetric surface measuring method works well for quantifying all types of transient frost roughness formations created at different atmospheric conditions. The method was validated through the measurements of 3D printed surfaces with known roughness statistics and the percent differences of the measurements from the true values were all less than 7% for RMS heights of concern. The photogrammetric measuring method was also assessed for repeatability and demonstrated a maximum standard deviation of 0.259 mm for equivalent sand-grain roughness, which is

hypothesized to have mainly resulted from the stochastic nature of frost formation. Additionally, the measurement frequency was checked to ensure no valuable data was lost between data acquisition times.

Atmospheric Factors

From the resulting frost surface measurements, several conclusions were made about the atmospheric factors. The most prominent atmospheric factor that affects the entire development of frost roughness formation is air velocity. A faster air velocity will result in a more rapid development of frost formation, but roughness will decrease drastically if the development reaches a point of redensification. The next highest governing atmospheric factor during the timeframe of concern is air temperature, which demonstrates that colder temperatures increase the maximum height of frost dendrites. Furthermore, the results portray that colder air temperatures and slower air velocities produce frost formations that are more sensitive to atmospheric variations. The third most influential factor is surface temperature which impacts the initial density of the frost formation. All three of these atmospheric factors interact with one another to create frost formations that develop at different rates, redensify at different times, and have different roughness characteristics. Lastly, relative humidity has little effect on the characteristic of frost roughness.

Critical Frost Case

One of the more critical cases of cold-soaked fuel frost impacting aerodynamic performance occurs for slower air velocities and colder air temperatures. The equivalent sand-grain roughness values for an air temperature of 10 °C and velocity of 0.5 m/s

demonstrated maximum values around 4.5 mm. Furthermore, this sand-grain roughness value occurred during the average turnaround time frame of a commercial airplane. The results indicate that if air temperature and air velocity continue to decrease the resulting maximum sand-grain roughness value would increase.

Future Work

This research is the first use of photogrammetry measuring transient, micro surface roughness. The results and conclusions from this study provide a solid foundation for future work on studying the aerodynamic effects of CSFF on the wings of aircraft. Future studies will build upon the methodology of this photogrammetric approach to enhance the utility of the method by making it autonomous. Additionally, the photogrammetric approach will be used in a facility that more closely simulates cold-soaked fuel frost on the wings of aircraft. With these adaptations an accurate prediction model and public database of CSFF on aircraft wings may be created.

Wing Surface Model

The effects of convective heat transfer from the fuel and conduction from the skin and wing surface were not considered in the Baylor Frost Tunnel measurements. Therefore, a wing surface model that replicates the formation of cold-soaked fuel frost on commercial aircraft is needed. These issues are planned to be resolved with a wing box model that simulates fuel flow underneath a surface and matches the surface material and paint job of operational aircraft. A prototype model of this system is shown in Figure 5.1.

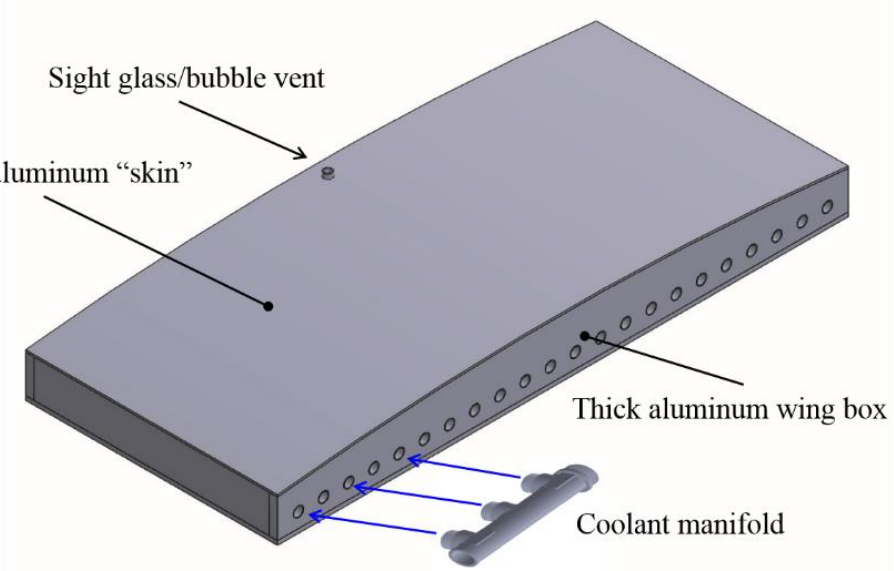

Figure 5.1: Wing Box SolidWorks Model

Remote Photogrammetry System

Future work must also entail a remote photogrammetric system, to improve accuracy and increase measurement production rate. This will be accomplished through the use of three motorized traverse rails that position the camera at specific locations above the surface as shown in Figure 5.2. With a preset program controlling the motors and image capturing times, the entire procedure will be autonomous, resulting in a more productive and accurate measuring method. Furthermore, this robotic system will enable the location of the camera to be recorded for each image captured. As mentioned in the Chapter 2 and Chapter 3, knowing the location of the camera increases accuracy and computation speed.

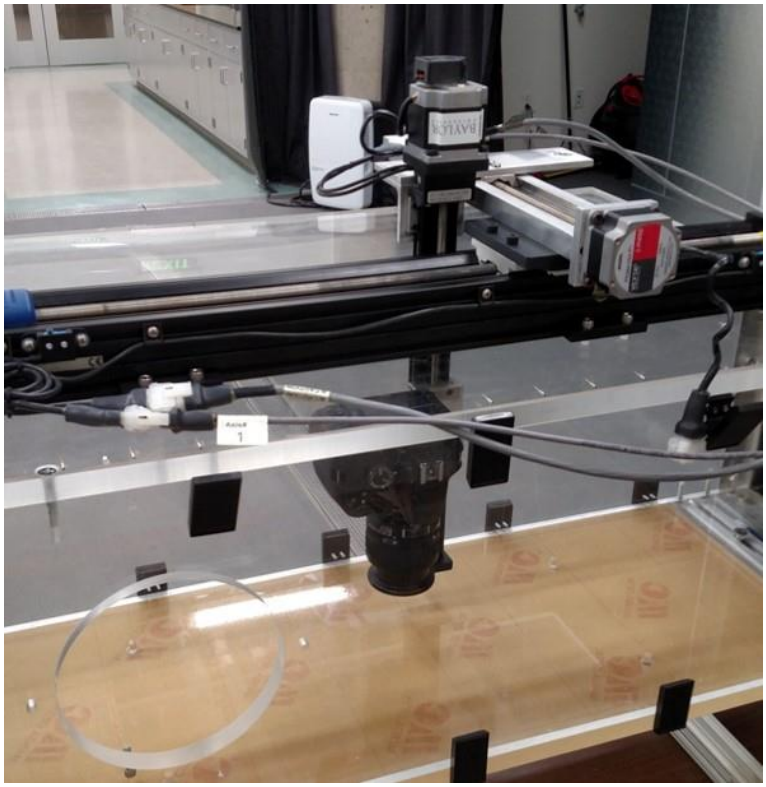

Figure 5.2: Remote Photogrammetry System for Future Testing

Test Facility

For the two previous tasks to be completed a climate chamber (Figure 5.3) has been constructed that accommodates a wind tunnel with a 12” by 12” test section (Figure 5.4). Compared to the closed-loop psychrometric wind tunnel, this new system will be able to more closely simulate environmental conditions experienced in CSFF scenarios compared to the Baylor Frost Tunnel. The wind tunnel will integrate the final wing box model on the bottom side of the test section and the autonomous photogrammetric measuring system will be equipped on the top side. When the climate chamber, wind tunnel, wing box model and the photogrammetric system are synchronized, it will be possible to accurately and remotely measure CSFF roughness for various atmospheric conditions.

Figure 5.3: Climate Chamber for Future Testing

Figure 5.4: Wind Tunnel for Future Testing

Frost Prediction Model

The final step to the complete analysis of cold-soaked fuel frost will be the creation of a one-dimensional model that incorporates not just the frost roughness but also the frost thickness. Frost thickness measurements are already being performed in the Baylor Frost Tunnel using a microscope to capture side profile views of the frost formations. For the final thermodynamic prediction model to be calculated, cold-soaked frost roughness and thickness measurements are required for a wide range of atmospheric conditions. From these measurements the empirical correlations will be analyzed to create a model. It is expected that the frost roughness model will reflect the wall-normal height of the water triple point temperature and variations in the thermal boundary layer thickness. From the model, a database will be published that provides fundamental information about the aerodynamic degradation resulting from cold-soaked fuel frost for a range of atmospheric conditions.

APPENDICES

APPENDIX A

Sample MATLAB Scripts

MainProgram

This MATLAB script was used to organize the imported point cloud files into the chronologically working functions that: leveled the scale bar surface (levelerX), rotated the scale bar (RotateSlopeX), determined the z-scale factor (Z_scaleFinderX) and reduced the data to surface statistics and plotted the height distributions (RoughPlot). The MainProgram then plotted the surface statistics versus time and exported these values in a simple text file for comparison to other test conditions. Note that the X at the end of the functions represent a point cloud file with the scale bar aligned with the virtual x-axis that the photogrammetric software autonomously determined. This does not affect the results, only a variation in the computation process as corresponding MATLAB functions were created for scale bars virtually oriented along the y-axis.

```
% Real Frost Roughness Evaluation Main Program
% Surface Roughness of Frost Using Photogrammetric Methods
% Date 05/28/18

format long

clear all;
close all
clc

%%%%%%%%%%%%%%%%%%%%%%%% Import Data  %%%%%%%%%%%%%%%%%%%%%%%%
% Photogrammetry Frost Surface Point Cloud (mm)
Rq0 = 0.00; %mm
File1 = 1000*dlmread('Sq 15min.txt');
File2 = 1000*dlmread('Sq 30min.txt');
File3 = 1000*dlmread('Sq 45min.txt');
File4 = 1000*dlmread('Sq 60min.txt');
File5 = 1000*dlmread('Sq 75min.txt');
File6 = 1000*dlmread('Sq 90min.txt');
File7 = 1000*dlmread('Sq 120min.txt');
```

```
% Time each measurement was taken (minutes)
time = [0 15 30 45 60 75 90 120];

% Photogrammetry Sloped Surface of Scale Bar Point Cloud
Slope1 = 1000*dlmread('slope 15min.txt');
Slope2 = 1000*dlmread('slope 30min.txt');
Slope3 = 1000*dlmread('slope 45min.txt');
Slope4 = 1000*dlmread('slope 60min.txt');
Slope5 = 1000*dlmread('slope 75min.txt');
Slope6 = 1000*dlmread('slope 90min.txt');
Slope7 = 1000*dlmread('slope 90min.txt');

% Change following text to correct conditions
Conditions = {'Air Temp = 10^{\circ}C','Surf Temp = -25^{\circ}C','Rel.
Humid = 76%','Air Speed = 0.5 m/s'};

% Angle of Scale Bar (Found from Solidworks Model and Keyence)
angle = 60; %(degrees)

% Photogrammetry "Horizontal" Surface of Scale Bar Point Cloud
HorizFile = 1000*dlmread('horiz.txt');


%%%%%%%%%%%%%%%%%%%%%%  Main Program  %%%%%%%%%%%%%%%%%%%%%%%%%%%%

% Change function to correct X or Y
% Determines angle to rotate sloped surface
% Multiple of 2 applied based on empirical correlations in validation
ang_to_rot = 2*levelerX(HorizFile);

%     Time 1    (15 minutes)
% Rotates sloped surface so that top surface is level
RSlope1 = RotateSlopeX(Slope1,ang_to_rot);
%  Determine z-scale factor from sloped surface fit that will be
% applied to frost surface
Z_scale1 = Z_scaleFinderX(RSlope1,angle);
%  Applies z-scale factor to frost surface, reduces data and plots
% height distribution
[Rq1,Skw1,P2V1,Ks1] = RoughPlot(File1,Z_scale1)
fprintf('\n')

%     Time 2    (30 minutes)
RSlope2 = RotateSlopeX(Slope2,ang_to_rot);
Z_scale2 = Z_scaleFinderX(RSlope2,angle);
[Rq2,Skw2,P2V2,Ks2] = RoughPlot(File2,Z_scale2)
fprintf('\n')

%     Time 3    (45 minutes)
RSlope3 = RotateSlopeX(Slope3,ang_to_rot);
Z_scale3 = Z_scaleFinderX(RSlope3,angle);
[Rq3,Skw3,P2V3,Ks3] = RoughPlot(File3,Z_scale3)
fprintf('\n')
```

```
%     Time 4    (60 minutes)
RSlope4 = RotateSlopeX(Slope4,ang_to_rot);
Z_scale4 = Z_scaleFinderX(RSlope4,angle);
[Rq4,Skw4,P2V4,Ks4] = RoughPlot(File4,Z_scale4)
fprintf('\n')

%     Time 5    (75 minutes)
RSlope5 = RotateSlopeX(Slope5,ang_to_rot);
Z_scale5 = Z_scaleFinderX(RSlope5,angle);
[Rq5,Skw5,P2V5,Ks5] = RoughPlot(File5,Z_scale5)
fprintf('\n')

%     Time 6    (90 minutes)
RSlope6 = RotateSlopeX(Slope6,ang_to_rot);
Z_scale6 = Z_scaleFinderX(RSlope6,angle);
[Rq6,Skw6,P2V6,Ks6] = RoughPlot(File6,Z_scale6)
fprintf('\n')

%     Time 7    (120 minutes)
RSlope7 = RotateSlopeX(Slope7,ang_to_rot);
Z_scale7 = Z_scaleFinderX(RSlope7,angle);
[Rq7,Skw7,P2V7,Ks7] = RoughPlot(File7,Z_scale7)
fprintf('\n')

%%%%%%%%%%%%%%%%  Plotting Roughness versus Time  %%%%%%%%%%%%%%%%%%

RMS_Height = [Rq0 Rq1 Rq2 Rq3 Rq4 Rq5 Rq6 Rq7];
figure (1);
plot(time,RMS_Height,'x-','MarkerSize',6,'LineWidth',2);
xlabel('Time (minutes)');
ylabel('RMS Height (mm)');
dim = [.6 .15 .05 .3];
annotation('textbox',dim,'String',Conditions,'FitBoxToText','on');
grid on;
title({'Time Evolution of Frost RMS Height'});

Skewness = [0 Skw1 Skw2 Skw3 Skw4 Skw5 Skw6 Skw7];
figure (2);
plot(time,Skewness,'x-','MarkerSize',6,'LineWidth',2);
xlabel('Time (minutes)');
ylabel('Skewness');
dim = [.6 .15 .05 .3];
annotation('textbox',dim,'String',Conditions,'FitBoxToText','on');
grid on;
title({'Time Evolution of Frost Skewness'});

Peak2Valley = [0 P2V1 P2V2 P2V3 P2V4 P2V5 P2V6 P2V7];
figure (3);
plot(time,Peak2Valley,'x-','MarkerSize',6,'LineWidth',2);
xlabel('Time (minutes)');
ylabel('Max to Min Height (mm)');
dim = [.6 .15 .05 .3];
annotation('textbox',dim,'String',Conditions,'FitBoxToText','on');
grid on;
```

```
title({'Time Evolution of Frost Peak-to-valley Height'});

KS = [0 Ks1 Ks2 Ks3 Ks4 Ks5 Ks6 Ks7];
figure (4);
plot(time,KS,'x-','MarkerSize',6,'LineWidth',2);
xlabel('Time (minutes)');
ylabel('Equivalent Sand-Grain Roughness (mm)');
dim = [.6 .15 .05 .3];
annotation('textbox',dim,'String',Conditions,'FitBoxToText','on');
grid on;
title({'Time Evolution of Frost Equivalent Sand Grain Roughness'});


%%%%%%%%%%%%%%%%%%%%%% Export  %%%%%%%%%%%%%%%%%%%%%%%%%%%%
Sq_Time = vertcat(RMS_Height,Skewness,Peak2Valley,KS,time);
%Change text file name for specific test
dlmwrite('Sq_Time180528_10_-25_76_0.5.txt',Sq_Time,'Delimiter','\t'
```

LevelerX

This MATLAB function imported the top surface of the scale bar, determined the rotational angle along the x-axis to make it perfectly level and exported this angle.

```
function angle_to_rot = levelerX(HorizPlaneXYZ);

  % Separating text file to x, y, z files
  PhotoY = HorizPlaneXYZ(:,1);
  PhotoX = HorizPlaneXYZ(:,2);
  PhotoZ = HorizPlaneXYZ(:,3);

  % Determining angle from horizontal using a surface fit
  sc_sf = fit([PhotoX,PhotoY],PhotoZ,'poly11'); %Raw surface fit
  coeffs = coeffvalues(sc_sf);
  slope = coeffs(2);
  angle_to_rot = (atan(slope/1));  % Exported value

end
```

RotateSlopeX

This MATLAB function imported the sloped surface file of the scale bar and the angle to rotate from the leveler function. It then rotated the sloped surface specified by the angle along the x-axis and exported this newly rotated sloped surface.

```
function rotated_PhotoSlope = RotateSlopeX(PhotoSlope,angle_from_level)

  % Separating text file to x, y, z files
  PhotoSX = PhotoSlope(:,1);
  PhotoSY = PhotoSlope(:,2);
  PhotoSZ = PhotoSlope(:,3);

  % Rotation of files
  X = PhotoSX;
  Y = PhotoSY*cos(angle_from_level) - PhotoSZ*sin(angle_from_level);
  Z = PhotoSY*sin(angle_from_level) + PhotoSZ*cos(angle_from_level);

  rotated_PhotoSlope = horzcat(X,Y,Z); % Exported file

end
```

Z_scaleFinderX

This MATLAB function imported the rotated sloped surface and performed an iterative numerical method to determine a z-scale factor that modified the slope to match the slope specified by the angle of the SolidWorks model of the scale bar.

```
function Z_scale = z_scalefinderX(RPhotoSlope,angle)

   % Separating text file to x, y, z files
   PhotoY = PhotoSlope(:,1);
   PhotoX = PhotoSlope(:,2);
   PhotoZ = PhotoSlope(:,3);

   % Initial Guesses
   int_ang = 1;
   Z_scale = 1.5;

   % Iterative Method of increasing slope
   while int_ang < angle

     sc_PhotoZ = PhotoZ * Z_scale;
     sc_sf = fit([PhotoX,PhotoY],sc_PhotoZ,'poly11'); %Raw surface fi
     coeffs = coeffvalues(sc_sf);
     slope = coeffs(2);
     int_ang = abs(radtodeg(atan(slope/1)));
     Z_scale = Z_scale + .005; % Exported value

   end

 end
```

RoughPlot

This MATLAB function imported the frost surface file and the z-scale factor. It then applied the factor to the surface in the z-direction and calculated the RMS height, skewness, peak-to-valley height and equivalent sand-grain roughness value which were all exported. This function also plotted the frost height distribution, using either a set z-axis limit or an auto scaled limit.

```
function [Rq,Skw,P2V,Ks] = RoughPlot(PhotoSurface,Z_scale,Z_limit)

  % Separating text file to x, y, z files
  PhotoX = PhotoSurface(:,1);
  PhotoY = PhotoSurface(:,2);
  PhotoZ = PhotoSurface(:,3);
  % Applying z-scale factor
  scaled_PhotoZ = PhotoZ * Z_scale;
  sf = fit([PhotoX,PhotoY],scaled_PhotoZ,'poly11'); %Surface fit data
  sf_Z = sf(PhotoX,PhotoY);
  % Setting minimum frost height to zero
  new_PhotoZ = (scaled_PhotoZ-sf_Z)-min(scaled_PhotoZ-sf_Z);

  %%%%%%%%%%%%%%%% Surface Statistics %%%%%%%%%%%%%%%%
  % RMS Height: Rq
  Rq = sqrt(1/(length(scaled_PhotoZ)-1)*sum((scaled_PhotoZ-sf_Z).^2));
   % Skewness: Skw
  Skw = (1/Rq^3)*(1/(length(scaled_PhotoZ)-1)*sum((scaled_PhotoZ-...
      sf_Z).^3));
  % Peak-to-valley Height: P2V
  P2V = max(scaled_PhotoZ-sf_Z) + abs(min(scaled_PhotoZ-sf_Z));
  % Equivalent Sand-Grain Roughness Height: Ks
  Ks = 4.43.*Rq.*(1+Skw).^1.37;

  %%%%%%%%%%   Plotting frost height distributions  %%%%%%%%%%%%%%
  figure (100);
  scatter3(PhotoX, PhotoY, new_PhotoZ, 1, new_PhotoZ)
  ylabel('y (mm)');
  xlabel('x (mm)');
  zlabel('z (mm)');
  xt = get(gca, 'XTick');
  set(gca, 'FontSize', 10);
  axis equal;
  dim = [.56 .67 .05 .3];
  colormap(jet)
  colorbar
  ylabel(colorbar,'Height (millimeters)','FontSize', 10);
  %Delete the following two lines of code, if auto scaling plot
  zlim([0 Z_limit]);
  caxis([0,Z_limit]);

end
```

APPENDIX B

Validation Surface Roughness Parameters

This appendix provides the surface roughness statistics of the fabricated validation surfaces. It displays the computationally approximated values of the peak-to-valley height, the exact surface statistics physically measured with the Keyence VR-3000, and the photogrammetric measurements acquired from one of the repeated tests (180422).

Table B.1: Validation Surface Parameters

Computational	**Keyence Measured**			**Photogrammetrically Measured**		
Approx. Peak-to-Valley (μm)	Peak-to-Valley (μm)	RMS Height (μm)	Skewness	Peak-to-Valley (μm)	RMS Height (μm)	Skewness
250	148.70	21.68	0.25	115.68	15.03	0.45
500	349.90	54.46	0.87	346.26	54.49	0.93
750	609.10	102.81	0.95	612.42	104.38	0.90
1000	763.30	131.89	0.85	773.35	136.06	0.89
1500	1138.10	232.04	0.76	1201.29	239.82	0.70
2000	1610.40	311.09	0.83	1720.99	326.59	0.79
3000	2280.00	458.01	0.70	2470.03	492.11	0.69

REFERENCES

[1] Munson, B. ., Young, D. F., Okiishi, T. H., and Huebsh, W. W., 2009, *Fundamentals of Fluid Mechanics*, John Wiley & Sons, Inc, Hobken, NJ.

[2] Ranter, H., "ASN Aircraft Accident Canadair CL-600-2B16 Challenger 604 N90AG Birmingham International Airport (BHX)" [Online]. Available: http://aviation-safety.net/database/record.php?id=20020104-0. [Accessed: 23-May-2018].

[3] Jackson, M., 2016, *Petition for Exemptions, 14 CFR 91.527(a) - Operations in Icing Conditions*, FAA-2016-8561-0001, Boeing, Gary, Indiana.

[4] 1996, "14 CFR Part 135.227 - Icing Conditions: Operating Limitations."

[5] White, F. M., 2006, *Viscous Fluid Flow*, McGraw-Hill, New York, NY.

[6] Tsukizoe, T., and Hisakado, T., 1970, "The Influence of Surface Roughness on the Mechanism of Friction," J. of Lubrication Tech, **92**(2), pp. 264–272.

[7] Georgiadis, J. G., 1990, "Microscopic Study of Frost Inception," Rome, Italy.

[8] Kumar, B., and Marshal, B. ., *An Illustrated Dictionary of Aviation*, McGraw-Hill, New York, NY.

[9] Hobbs, P., 1974, *Ice Physics*, Clarendon Press, Oxford, England.

[10] Dietenberger, M. A., 1982, "A Frost Formation Model and Its Validation Under Various Experimental Conditions," NASA Contractor Report 3595, (3595), p. 70.

[11] Bucklin, R. A., and Haman, D. Z., 2007, "Reading the Simplified Psychrometric Chart for Frost Protection," IFAS, p. 5.

[12] Dooley, J. B., 2010, "Determination and Characterization of Ice Propagation Mechanisms on Surfaces Undergoing Dropwise Condensation."

[13] Jones, B. W., and Parker, J. D., 1975, "Frost Formation with Varying Environmetnal Parameters," ASME, **97**, pp. 255–259.

[14] O'Neal, D. L., and Tree, D. R., 1984, "Frost Growth and Heat Transfer in a Parallel Plate Geometry," *American Society of Mechanical Engineers (Paper)*.

[15] Sherif, S. A., Raju, S. P., Padki, M. M., and Chan, A. B., 1993, "A Semi-Empirical Transient Method for Modeling Frost Formation on a Flat Plate," International Journal of Refrigeration, **16**(5), pp. 321–329.

[16] Lee, K.-S., Kim, W.-S., and Lee, T.-H., 1997, "A One-Dimensional Model for Frost Formation on a Cold Flat Surface," International Journal of Heat and Mass Transfer, **40**(18), pp. 4359–4365.

[17] Lee, K.-S., Jhee, S., and Yang, D.-K., 2003, "Prediction of the Frost Formation on a Cold Flat Surface," International Journal of Heat and Mass Transfer, **46**(20), pp. 3789–3796.

[18] Hermes, C. J. L., Piucco, R. O., Barbosa, J. R., and Melo, C., 2009, "A Study of Frost Growth and Densification on Flat Surfaces," Experimental Thermal and Fluid Science, **33**(2), pp. 371–379.

[19] Armengol, J. M., Salinas, C. T., Xamán, J., and Ismail, K. A. R., 2016, "Modeling of Frost Formation Over Parallel Cold Plates Considering a Two-Dimensional Growth Rate," International Journal of Thermal Sciences, **104**, pp. 245–256.

[20] Becker, C. M., and Els, P. S., 2014, "Profiling of Rough Terrain," International Journal of Vehicle Design, **64**(2–4), pp. 240–261.

[21] Reehorst, A. L., and Richter, G. P., 1987, "New Methods for Molding and Casting Ice Formations," NASA TM-100126.

[22] Lee, S., Broeren, A., Addy, H., Sills, R., and Pifer, E., 2012, "Development of 3D Ice Accretion Measurement Method," American Institute of Aeronautics and Astronautics.

[23] Hovenac, E. A., and Vargas, M., 1995, "A Laser-Based Shape Profilometer for Use in Icing Wind Tunnels," NASA TM-106936.

[24] Lee, S., Broeren, A., Kreeger, R. E., Potapczuk, M., and Utt, L., 2014, "Implementation and Validation of 3-D Ice Accretion Measurement Methodology," *AIAA-2014-2613*, Atlanta, GA.

[25] Broeren, A., Lee, S., and Monsastero, M., 2014, "Validation of 3D Ice Accretion Measurement Methodology for Experiemtal Aerodynamic Simulation," American Institute of Aeronautics and Astronautics, **6th**.

[26] Kreeger, R. E., and Tsao, J. ., 2014, "Ice Shapes on Tail Rotor," *AIAA-2014-2612*, AIAA, Atlanta, GA.

[27] Strong, C., 2017, "User Guide Artec Studio."

[28] An-su Wang, Bin Xie, and Zi-wei Liu, 2018, "Design of Measurement System of 3D Surface Profile Based on Chromatic Confocal Technology," pp. 1061618-10616–6.

[29] Keyence, 2017, “Wide-Area 3D Profile-Measuring Instrument,” Keyence America [Online]. Available: https://www.keyence.com/ss/products/microscope/roughness/equipment/wide-area-3D-measurement-instrument.jsp. [Accessed: 21-Jun-2018].

[30] Hariharan, P., 2003, *Optical Interferometry*, Academic Press.

[31] Chen, M. M., and Rohsenow, W., 1964, “Heat, Mass, and Momentum Transfer Inside Frosted Tubes—Experiment and Theory,” Journal of Heat Transfer, **86**(3), p. 334.

[32] Schlichting, H., 1936, “Experimental Invsetigation of the Problem of Surface Roughness,” National Advisory Committee on Aeronautics, **TM-832**.

[33] Lawrysyn, M., 1989, “Aerodynamic Characteristics of Frost Roughness,” Carleton University, p. 157.

[34] Langston, P. A. ., 1968, “Hoar Frost on Aircraft Surfaces,” BEA Engineering - Project and Developement Technical Note, **1**, p. 570.

[35] Dirling, J., R., 1973, “A Method of Computing Roughwall Heat Transfer Rates on Reentry Nosetips,” *8th Thermophysics Conference*, American Institute of Aeronautics and Astronautics.

[36] Yun, R., Kim, Y., and Min, M., 2002, “Modeling of Frost Growth and Frost Properties with Airflow Over a Flat Plate,” International Journal of Refrigeration, **25**(3), pp. 362–371.

[37] Linder, W., 1959, 2003, *Digital Photogrammetry: Theory and Applications*, Springer, New York;Berlin;

[38] Schenk, T., 2005, *Introduction to Photogrammetry*, Ohio State University Department of Civil and Environmental Engineering.

[39] Smith, M. W., Carrivick, J. L., and Quincey, D. J., 2016, “Structure From Motion Photogrammetry in Physical Geography,” Progress in Physical Geography, **40**(2), pp. 247–275.

[40] Vosselman, G., and Maas, H.-G., 2010, *Airborne and Terrestrial Laser Scanning*, Whittles Publishing.

[41] Lutz, K., 2015, “61 Years of Working Aerial Photogrammetry History,” Photogrammetric Engineering and Remote Sensing, **81**(2), pp. 89–93.

[42] Mason, A., 2015, “Making 3D Models with Photogrammetry,” The Haskins Society Journal Carleton College.

[43] Liu, T., Burner, A. W., Jones, T. W., and Barrows, D. A., 2012, “Photogrammetric Techniques for Aerospace Applications,” paerosci, **54**, pp. 1–58.

[44] Pappa, R. S., Jones, T. W., Black, J., and Walford, A., 2002, "Photogrammetry Methodology Development for Gossamer Spacecraft Structures," NASA, **TM-2002-211739**, p. 23.

[45] Collier, P., Dixon, L., Fontana, D., Payne, D., and Pearson, A. w., 1999, "The Use of Close Range Photogrammetry for Studying Ice Accretion on Aerofoil Sections," The Photogrammetric Record, **16**(94), pp. 671–684.

[46] Soinne, E., Rosnell, T., and Viljanen, N., "Aerodynamic, Laser and Photogrammetry Measurements on CRM Wing Model with Frost," p. 61.

[47] Koivisto, P., 2015, *Effects of Cold Soaked Fuel Frost on Lift Degradation during Simulated Take-Off*, Aalto University and Finish Transportation Safety Agency.

[48] Schindler, K., 2014, *Handbook of Geomathematics*, ETH Zurich.

[49] Luhmann, T., Fraser, C., and Maas, H.-G., 2016, "Sensor Modelling and Camera Calibration for Close-Range Photogrammetry," ISPRS Journal of Photogrammetry and Remote Sensing, **115**, pp. 37–46.

[50] Semyonov, D., and Pasumansky, A., 2017, "Photogrammetry Manual Orthophoto, DEM without GCPs."

[51] Keyence, 2017, "Surface Roughness Parameters," Introduction to Roughness [Online]. Available: www.keyence.com/ss/products/microscope/roughness/line/index.jsp.

[52] Flack, K. A., and Schultz, M. P., 2010, "Review of Hydraulic Roughness Scales in the Fully Rough Regime," Journal of Fluids Engineering, **132**(041203), pp. 1–10.

[53] Nikuradse, J., 1933, "Laws of Flows in Rough Pipes," VDI-Forshungsheft, **4**, p. 361.

[54] Bejan, A., 2004, *Convection Heat Transfer*, Wohn Wiley & Sons, Hoboken NJ.

[55] Cheng, C., and Wu, K., 2003, "Observations of a Early-Stage Frost Formation on a Cold Plate in Atmospheric Air Flow," ASME, **125**(95).

[56] Dietenberger, M. A., 1984, "Simple and Safe Takeoff or Landing Procedure with Wing Surface Contaminations," Journal of Aircraft, **21**(12), pp. 955–961.

[57] Kind, R., 1998, "Icing, Frost and Aircraft Flight Frost.Pdf," Canadian Aeronautics and Space Journal, **44**(2), pp. 110–118.

[58] Bragg, M., Henrich, D., Valarezo, W., and McGhee, R., 1994, "Effect of Underwing Frost on Airfoil at Flight Reynolds Numbers," Journal of Aircraft, **31**(6), p. 8.

[59] Weiland, M., 2016, "Boeing Executive Flight Operations – Cold Soaked Fuel Frost (CSFF) Training."

[60] Buhler, Y., Andreas, S., Marc, A., Ruedi, B., and Christian, G., 2016, "UAS Photogrammetry of Homogenous Snow Cover," DGPF, **25**.

[61] Fisher, R. A., Sir, 1890-1962, 1946, *Statistical Methods for Research Workers*, Oliver & Boyd.

[62] Chullen, A., and Frey, C., 1999, *Probabilistic Techniques in Exposure Assessment: A Handbook for Dealing with Variability and Uncertainty in Models and Inputs*, Springer Science and Business.

[63] Tecson, L., 2013, "Convective Heat Transfer from Realistic Ice Roughness Distributions."

[64] Wu, C., and Caves, R. E., 2004, "Modelling and Optimization of Aircraft Turnaround Time at an Airport," Transportation Planning and Technology, **27**(1), pp. 47–66.